

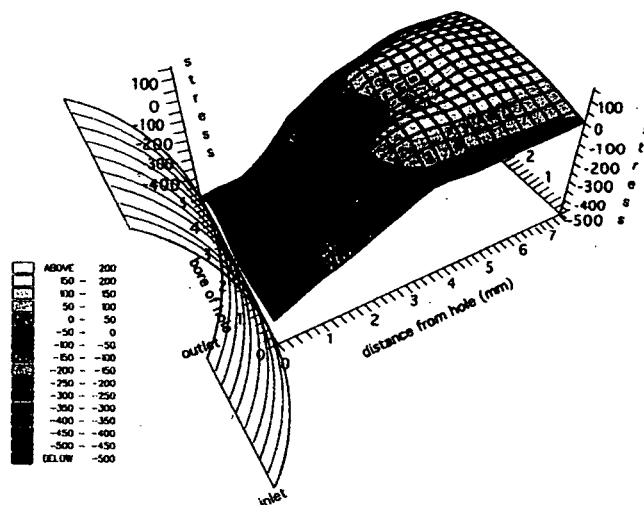


Technical Report
RAL-TR-96-068

PREMIS

Final Technical Report

The Precise Measurement of Internal Stress within Materials using Pulsed Neutrons



Contract BRE2-CT92-0156, Project. no. 5129

Project Coordinator: Rutherford Appleton Laboratory, UK

Partners:
University of Kiel, D
University of Ancona, I
University of Cambridge, UK
The Open University, UK

Starting Date: 1.12.92 Duration 36 months

Project Funded by the European
Community under the
Brite/EuRam Programme

CONTENTS

1 Executive Summary	2
2 Objectives	2
3 Means Used to Achieve Objectives	3
4 The ENGIN Instrument	4
5 Through Surface Measurements	20
6 Intergranular Stresses	32
7 Cold Expanded Faster Holes	43
8 Investigations of Vibrational Stress Relief	52
9 Welded Joints	65
10 Thermal Cycling of Composites	78
11 Fatigue Cracks in MMCs	88
12 Extracting the Strain Tensor	97
ANNEX I table of experiments performed	108
ANNEX II Publications from the PREMIS Project	109

1 Executive Summary

The objective of The PREMIS project has been to develop a routine, non destructive method of measuring internal stresses deep within engineering materials and components. This has been achieved through the construction of a new instrument, ENGIN, on the pulsed neutron facility ISIS, at the Rutherford Appleton Laboratory, and the development of the neutron strain scanning technique using this instrument.

The technique uses a custom designed neutron diffractometer, ENGIN, at ISIS, the pulsed neutron facility located at the Rutherford Appleton Laboratory (UK) to measure the lattice spacings of atoms within the component or material under study. The method is therefore similar to the conventional X-ray technique of measuring strain. The significant advantage of the neutron measurement is the ability of the neutron to penetrate many cm. into most common engineering materials (steels, aluminium, metal matrix composites (MMCs), etc...) making possible measurements deep within the material. A further advantage of the pulsed neutron measuring technique used on ENGIN is its ability to record the lattice spacings of each phase of a composite material - thus providing a unique insight into the stresses present in a composite component.

The PREMIS consortium has drawn upon expertise in Germany, Italy and the UK to construct the instrument, write new software and demonstrate the technique's full capabilities. The design and construction phase of ENGIN, including the analysis software was completed in the first half of 1994. The application of the new technique has been demonstrated in the following areas:

- thermal cycling of composites
- welded joints
- fatigue cracks in MMCs
- test of residual stress relief procedures
- cold expanded fastener holes
- through surface measurements.

2 Objectives

All engineering components are stressed to some extent, either in-service or as a result of their manufacture. Such stresses can result in mechanical failure, which may be costly to industry and have significant safety implications. In these cases, often found in the aerospace, automobile or nuclear industries, a deeper understanding of the stresses within a component is required. Traditional methods of determining residual stresses are either limited to surface measurements, or are destructive in nature.

Hence the overall objective of The PREMIS project has been to develop *a routine, non destructive method of measuring internal stresses deep within engineering materials and components.*

Like most projects, PREMIS has been structured as a series of tasks each with their own objectives and means used to achieve them. This document describes these individual components in chapters 4 -12, and the task objectives are described at the start of each chapter.

3 Means used to achieve objectives

The overall objective of developing *a routine, non destructive method of measuring internal stresses deep within engineering materials and components* has been solved by the construction and development of a new instrument (ENGIN). As is described in detail below it is capable of measuring strain variations up to 50 mm beneath the surface of engineering metals, ceramics and composites. The technique, called *neutron strain scanning* (NSS), uses the crystal lattice within most engineering materials as an atomic strain gauge to measure strain distributions with a sub-millimetre spatial resolution to an accuracy of better than 50 microstrain. The success of the method lies in the fact that it uses a neutron beam that is many more times penetrating than conventional X-rays.

While the technique of neutron strain measurement has been developed considerably since its inception in 1980, this has largely been on continuous, reactor neutron sources. However, pulsed neutron sources using the time-of-flight method, offer potential advantages in measuring internal strains, especially in composite materials. The ENGIN instrument is the first instrument using the *pulsed-neutron* technique in the world designed and optimised exclusively for making measurements on engineering components. These can be up to about a metre in size, and weigh as much as 250 kg.

There are thus many advantages of NSS over conventional stress measurement techniques:

- it can provide sub-surface information not obtainable by any other non-destructive non-contacting technique,
- it is applicable to most crystalline materials,
- the *pulsed* neutron strain scanning can measure the strain in *each component* of a composite material simultaneously within the same gauge volume,
- complicated data corrections are not required, since the stress state is not disturbed by the measurement,
- it can be used to measure stresses within components in environments typical of those experienced in-service,
- it can be used to validate finite element simulations and thus improve performance or lifetime predictions,
- it is much faster and less labour intensive than conventional destructive methods; such a hole drilling or X-ray diffraction followed by surface removal.

The main disadvantage of the technique lies in the scarcity of strain scanning facilities. However, the instrument and expertise at the Rutherford Appleton Laboratory now provide new access within Europe to industry.

The construction of the ENGIN pulsed neutron strain scanner was only the first part of the PREMIS project. Most importantly the instrument was then used to develop the technique through studying a range of engineering problems. In doing so, the technique has been refined, the correct software has been developed, and new results in engineering science obtained. Below, in section 4 we describe the method and the instrument in more detail, and in sections 5 - 12 the way in which the technique has been developed in different engineering areas.

4 The new ENGIN instrument

4.1. Design Objectives

The neutron strain scanning (NSS) technique, like its X-ray counterpart, determines the strain in a material by measuring the distance d_{hkl} between the {hkl} lattice planes within a small volume of the sample - the gauge volume. The strain is then calculated by comparing this measurement with that of the un-strained material (d_0).

ENGIN, a pulsed neutron strain scanning instrument, is therefore a specialised neutron diffractometer with three important attributes:

- an ability to measure the atomic lattice spacings to a high precision
- an ability to make such measurements on a small 'gauge volume' within the component under study, and
- an ability to position the gauge volume accurately with the component.

The neutron is a very penetrating probe, and using such a specialised diffractometer it is possible to measure the strain, and hence stress distribution, along a line, within a plane, or within the volume of the component under study. Moreover, by rotating the sample the strain may be measured along any particular direction, thus enabling the vector strain field to be mapped out in 3-dimensions.

In designing an instrument to meet the three objectives listed above a number of principal design parameters must be decided upon. In some cases (for example count rate and gauge volume) a technical compromise must be decided upon, in other cases the main constraint is cost. The principal design parameters of ENGIN were chosen such that :

- strain within samples could be measured to $\pm 50 \cdot 10^{-6}$ ($\pm 50 \mu\epsilon$)
- gauge volumes within samples could be resolved down to $< 2\text{mm}^3$ cube
- samples could be scanned $\pm 13\text{cm}$ (x,y,z)
- samples could be positioned to $\pm 0.1 \text{ mm}$
- samples up to 250 kg could be handled
- samples temperatures could be controlled up to 1000K

These design parameters therefore act as a benchmark in assessing the final performance of the ENGIN strain scanner.

4.2 The Basis of the Technique - Neutron Diffraction

The ENGIN instrument is situated on the S9 beamline at the ISIS pulsed neutron source, situated at the Rutherford Appleton Laboratory, UK (Fig 4.1). To understand its operation it is necessary to describe the techniques of pulsed-source neutron diffraction.

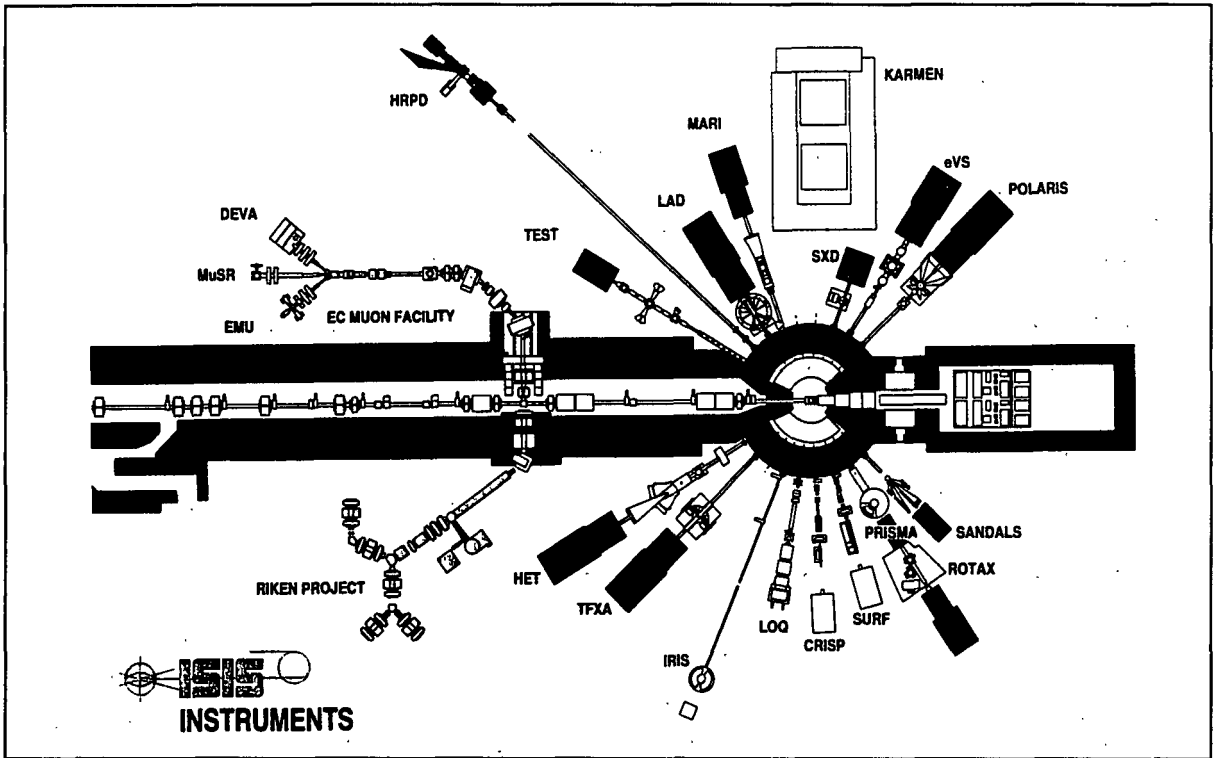


Fig 4.1

A diffractometer on a pulsed neutron source, such as ENGIN, may be represented diagrammatically by Fig 4.2.

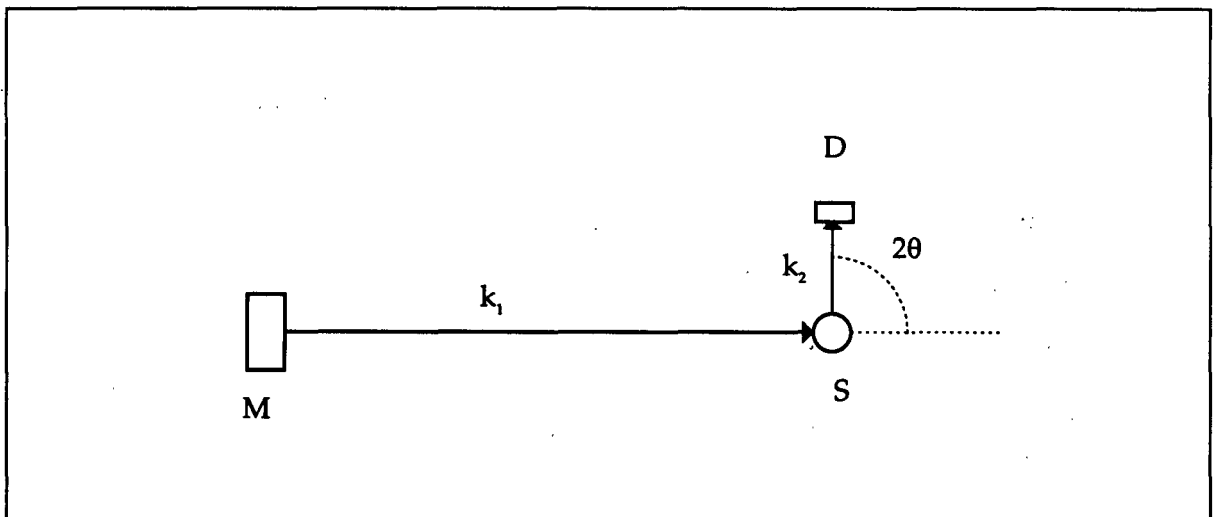


Fig 4.2

Neutrons originate from the moderator (M) in short pulses and travel to the sample (S) where they may scatter into a detector (D) situated at an angle of 2θ to the incident beam. The neutrons originating from the moderator have a wide energy range from a few meV up to many eV. Such energies correspond to neutrons with velocities comparable to the speed

of sound, and hence the neutrons take a few milliseconds to travel from the moderator to the detector, a distance of approximately 15m.

A polycrystalline sample, such as most metal engineering components, will diffract only those neutrons that satisfy Bragg's law;

$$\lambda = 2|d|\sin\theta \quad 4.1$$

and if the detected neutron count is plotted as a function of time (Fig. 4.3) it will exhibit a series of peaks corresponding to the different d_{hkl} lattice planes in the material.

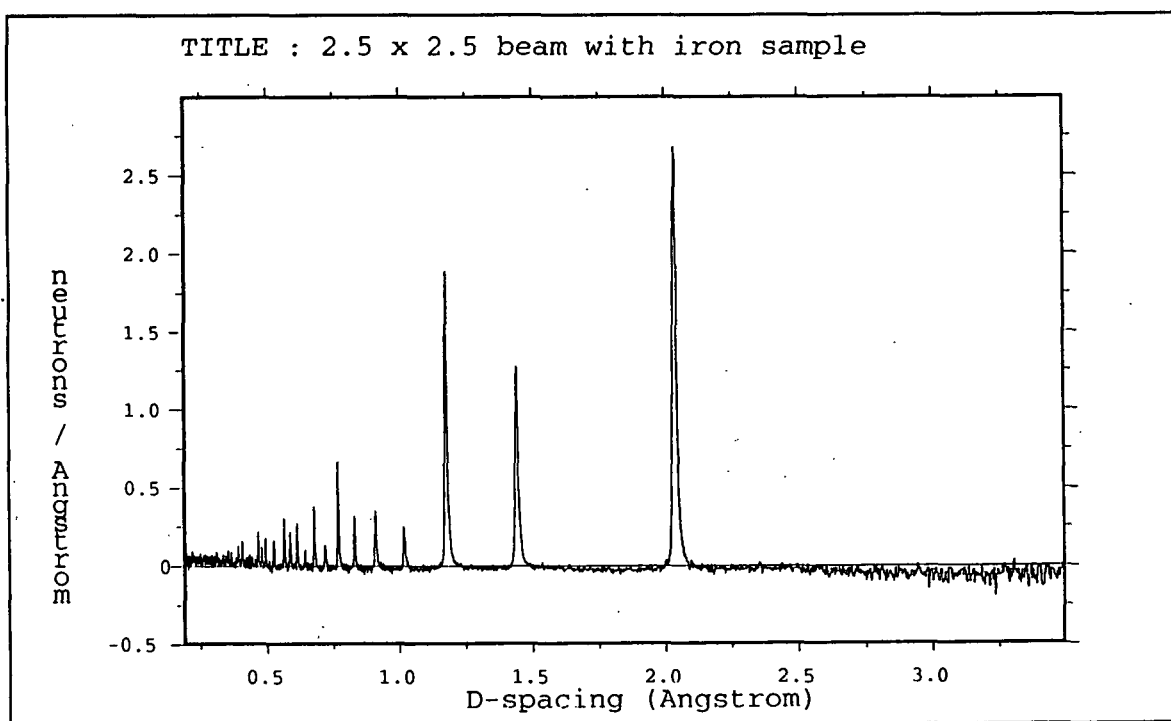


Fig. 4.3

By measuring the time-of-flight (t) from the moderator to the detector, the velocity (v) of the neutrons contributing to a particular Bragg peak may be calculated. Since the wavelength λ of a neutron is related to its velocity by the expression:

$$\lambda = \frac{0.39560}{v} \quad 4.2$$

(when λ is in nm and v in mm/ μ s) a knowledge of the velocity, and the diffraction angle (2θ) is sufficient to determine the lattice spacing d_{hkl} for the particular set of $\{hkl\}$ lattice planes within the sample.

Having determined d , it is then, in principle, straightforward to calculate the strain (ϵ) at that point in the sample from the relationship:

$$\epsilon = (d - d_0)/|d_0| \quad 4.3$$

It should be noted that the strain (ϵ) thus measured is a vector quantity and is measured along the direction of d_{hkl} , which is parallel to the vector τ defined by the expression:

$$\tau = k_2 - k_1 \quad 4.4$$

The directions k_0 and k_1 being along the incident and scattered directions of the neutron path (see Fig.4.2)

4.3 Instrument Construction

4.3.1 Overview

The ENGIN instrument consists of six major components. A collimated incident pulsed neutron beam, a large $xyz\omega$ positioner (to locate the gauge volume within the sample), secondary flight-path radial collimators (which define the gauge volume), and neutron detectors. In addition two telescopes and a laser/CTV system have been installed to enable the sample to be accurately aligned, and its motion monitored. These components are illustrated schematically in Fig. 4.4 and in greater detail in Fig. 4.5.

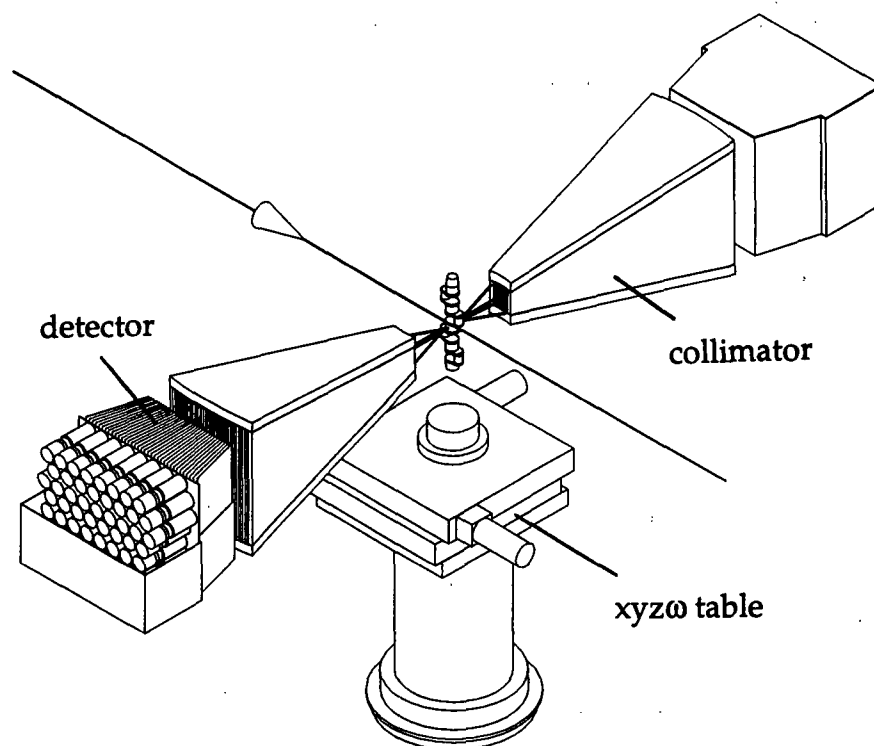


Fig 4.4

Perhaps the most innovative aspect of the instrument's design is the use of two large radial collimators, together with their associated detector banks. The collimators each have 40 vanes made from gadolinium oxide coated mylar, which allow the detectors to receive neutrons from a small volume (about 2mm in size, along the beam direction). For very large samples, one of the collimators can be rotated through 90° to give a larger sample space than the normal 300 mm region between the collimators.

The detectors have three horizontal rows, each of 45 elements, giving 135 elements per bank. Thus there are a total of 270 detectors altogether.

In addition, a small class 2 semiconductor laser is suspended above the centre of rotation of the positioner, which is the main fixed reference point, and a TV camera looks down at this point, its output being visible on two monitors, one in the blockhouse and one in the control cabin.

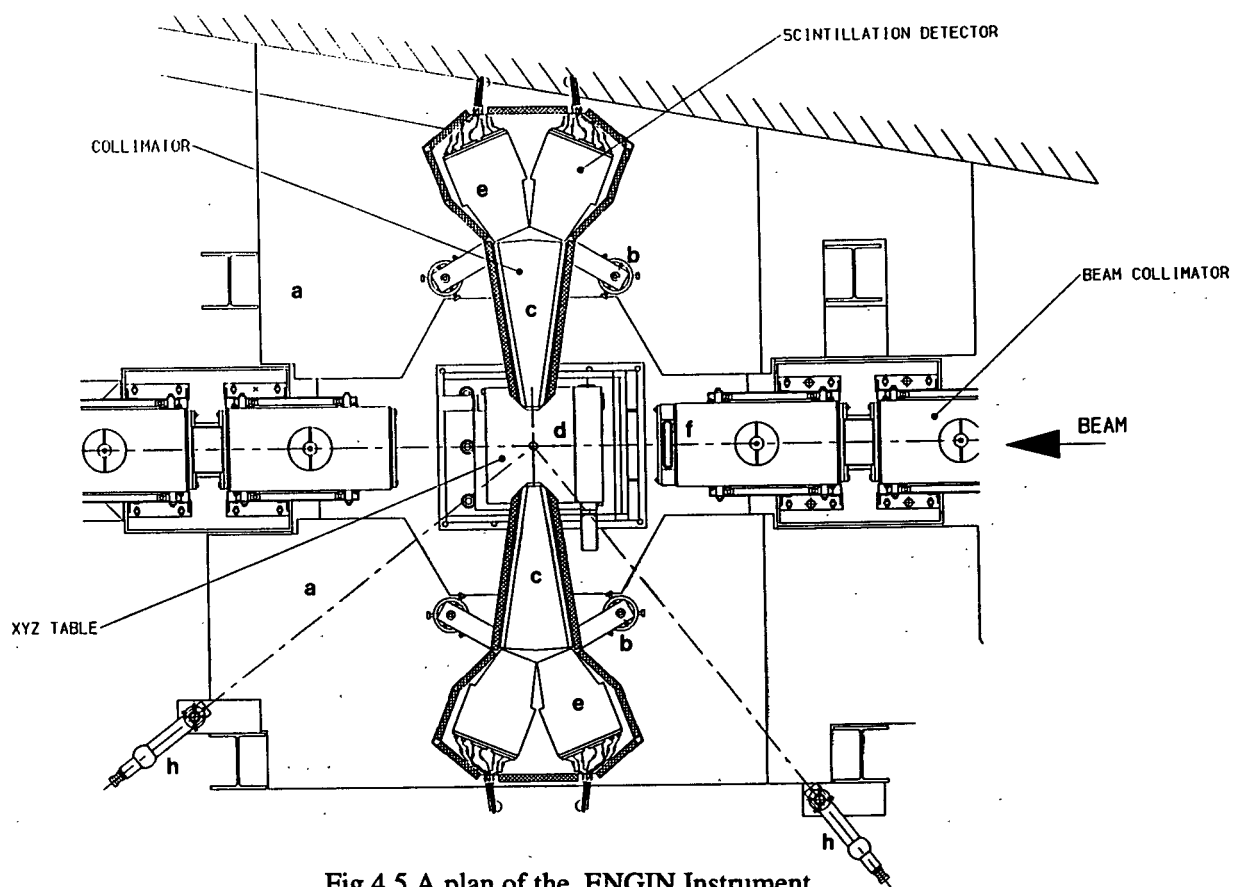


Fig 4.5 A plan of the ENGIN Instrument

(a) 2 sets of decked steelwork to act as supports for the collimators, and to provide working platform for sample changing, (b) 2 collimator mounts, with alignment blocks and facility to rotate collimator through 90° and lock collimator in position, (c) 2 radial collimators each with 40 gadolinium oxide coated mylar foils, giving 41 line of sight paths for neutrons. Input area 46mm wide by 60 mm high. Detector face area 230 mm by 300 mm. Shielded by boron carbide castings. (d) A four axis positioning device comprising an x-y table mounted on a rotating stand-off, the complete assembly movable in the z direction by a geared drive. (see diagram attached) The x-y table has 125 mm of movement about the centre point in each direction. The z drive has a total of 250 mm movement. The load carrying capacity is 250 kg. (e) Detectors. Each system consists of 135 detectors arranged in three rows of 45 detectors stacked above each other. (f) An incoming beam slit definition system consisting of a motorised translation stage carrying a frame supporting a pair of fixed slits forming a square or rectangular aperture. (g) A closed circuit TV system with two monitors, one in the control cabin and one in the blockhouse. A class 1 laser is installed shining vertically down onto the centre of rotation, thus providing a rough marking of the position of the gauge volume. (h) Alignment telescopes.

Following a 3-month design phase from December 1992 to February 1993, the ENGIN components were manufactured and installed on the ISIS TEST beamline in June - July 1993. At this stage the instrument was equipped with a prototype detector, to enable the final detector design to be optimised. The final detector was installed in two stages, in February and May 94, equipping the left hand and right hand collimators respectively. The incoming beam slit system was delayed by late delivery of components, but was surveyed in and installed in the summer '94 maintenance shutdown, and has since been used successfully and without interruption. CCTV monitoring and a gauge volume marker laser were installed at the end of 1994.

Thus the instrument evolved over the period of the project, and a summary of the status of the instrument, together with the experiments performed is given in Annex 1.

4.3.2 Incident Beam Collimation

The neutron beam collimation is provided by a pair of orthogonally mounted interchangeable slits made from sintered boron carbide. A range of such slits (0.5, 1, 2, 3, 4, 5, 10 and 25 mm wide, each 30mm long) has been made, allowing a wide range of square and rectangular beams to be provided. The whole assembly is cantilevered from a motorised, linear translation stage, so that it can be brought close to the sample. Translation of the slits is performed by a stepper motor system (so that no vibration will be transmitted to the slit assembly) and under commands similar to those of the main $xyz\omega$ positioner.

4.3.3 Positioner

The positioner has been designed to carry objects up to 250kg and position them to within 0.01 mm in x and y , 0.001 in z and with an angular accuracy of $.01^\circ$ in ω . It consists of an x - y table with a number of mounting holes in it to enable samples to be firmly fixed to it (see Fig 4.6 for dimensions). The x and y axes can move 125mm on either side of their normal datum point. The x - y table is mounted on a vertical column which can move in the z direction over a total range of 300 mm. The maximum height of the table is 310 mm below the neutron beam. The column sits on a direct drive motor which rotates the whole assembly in the ω direction through slightly less than 360° . The normal datum point of the ω axis is about 180° from the extremes of its travel. In this position, by convention, the x axis is along the incident neutron beam, with the positive direction being towards the moderator. The y axis is perpendicular to this, with the positive direction being to the right when facing towards the moderator.

The system accepts movement input commands and displays output positions in millimetres or degrees, accurate to $.01$ mm or 0.01° . The motion of the positioner has also been programmed using s-curve profiling to reduce the acceleration forces felt by the sample. Since it is possible to drive samples into the collimator, pressure sensitive pads have been installed on the shielding of the collimator to stop the positioner if this occurs.

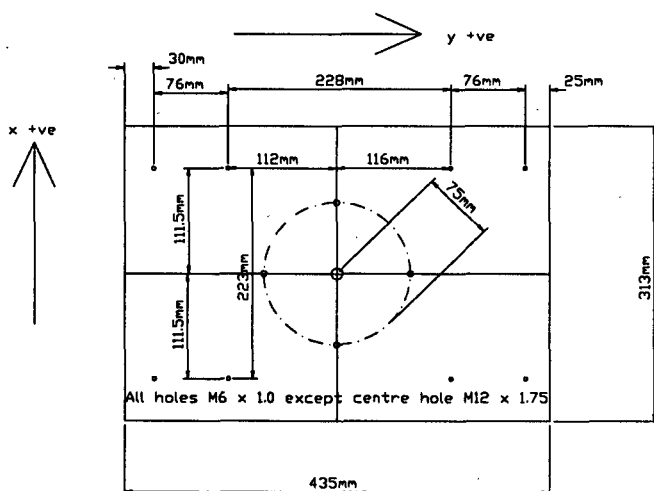


Fig. 4.6. The holes in the top plate of the x - y table and the sign convention of the translator movement.

4.3.4 Detector Collimation

In front of each detector is a radial collimator. This consists of 40 vertical foils of GdO coated mylar film arranged radially about a fixed focal point (see fig 4.7). The foils are opaque to neutrons, so that only neutrons which originate from near this focal point are detected.

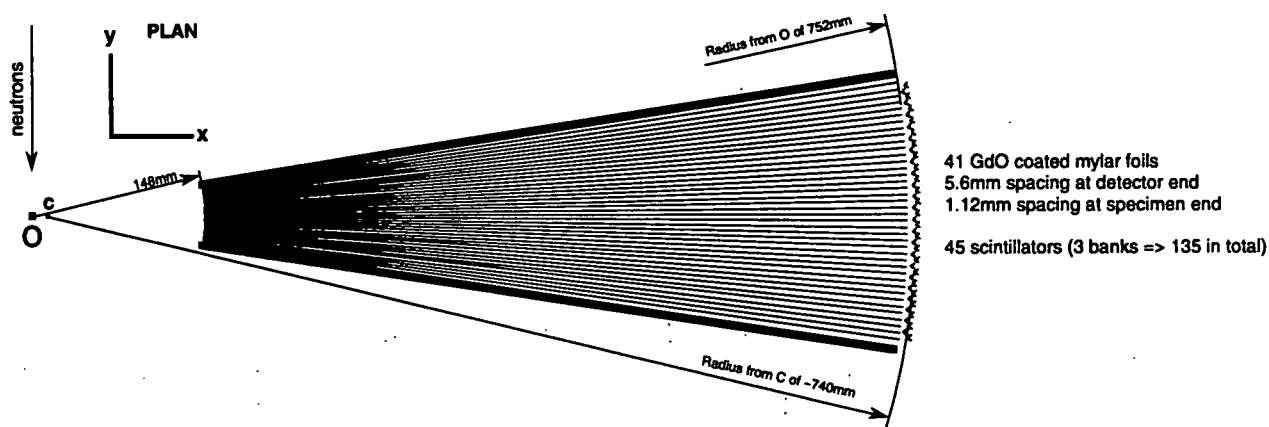


Fig 4.7: A scale diagram (plan view) of various components of the right hand collimator and a detector bank.

4.3.5 Detectors

The detection system on ENGIN consists of two detectors, each centred on a Bragg angle (2θ) of $\pm 90^\circ$. This enables the lattice spacing of the specimen, and hence the elastic component of the strain, to be measured simultaneously in two perpendicular directions.

Following the successful trials with a prototype detector, a decision was made to construct a fibre coupled scintillator design using a V shaped scintillator. The detector modules comprise 45 elements each 5mm wide and 100mm high. The 45 elements are $2C_n$ coded into 10 photo multiplier (PM) tubes, so that the signal from any pair of PM tubes uniquely specifies one of the 45 detector elements. Each detector bank is composed of 3 modules stacked vertically to produce 45 detector elements, each 5x300 mm. The detector therefore covers the angular range 81.4° to 98.6° in 2θ on each side of the incident neutron beam. The overall efficiency of the detector modules is about 60% at 1 Å.

4.4 Instrument and Sample Alignment

Sample Mounting & Alignment

Since small changes in the position of the ENGIN collimators cause large changes in the apparent strain measured it is essential to maintain the collimation system to a very high standard of positional accuracy. The aim of this section is to describe briefly the methods used to establish the positional calibration of the collimation system and the measurements that have been made to verify the positional stability of the incoming beam collimation system as a function of translation of the carrier stage and removal and reinsertion of the slit elements. Measurements made to locate and correct the position of the collimators in a direction orthogonal to the neutron beam are also described.

The alignment activity rests upon the assumption of the centre of rotation of the positioner as an invariant. It is also assumed that the z-axis defines the vertical. The positioner is first rotated until one of its translation axes lies perpendicular to the line of sight of the telescope. Then a 3.2mm iron rod is set up on the positioner. This rod has a conical point machined on one of its ends to aid visual alignment. This point is aligned with the centre of rotation of the positioner using the principal telescope. This is achieved by successive rotations of the

positioner through 180 degrees and incremental movement of the rod and the telescope until the vertical graticule and point remain in coincidence at both positions. By this means the centre of rotation of the positioner and the line of sight of the telescope can be made coincident to $\pm 0.05\text{mm}$. This derives from the readability of the cursor scale on the telescope which is readable to about 0.025mm .

The positioner is now rotated through 90 degrees and the other translation axis is brought to a position where the point and the graticule are again in coincidence. The second telescope - conventionally the one nearer the target station - can now be aligned with the point of the rod.

Alignment of the z-axis is achieved by levelling very accurately the principal telescope. The level used for this purpose has a stated precision of 2.5mrad and this precision is confirmed by reversal of the level. Once the telescope is levelled, then the z-drive is used to align the point of the rod with the horizontal graticule. The secondary telescope is also aligned with this position but note that no assumption is made that the secondary telescope is level since it is known that a difference in height of about 0.3mm exists between the two telescopes. At this point the rod may be driven up and down using the z-drive and the rotational alignment of the telescope graticules can be set so that the point remains aligned with the vertical graticule along its entire length.

To assist with sample alignment, a mock up of the sample mounting table, mounted on a bearing system, has been constructed to enable samples to be aligned outside the blockhouse. This reduces the setting up time on ENGIN itself and hence the number of neutrons wasted while the shutter is closed during sample alignment.

Alignment of the Neutron Collimators

The rod is now removed and replaced by the nylon thread assembly. The thread is then aligned so that it is coincident with the centre of rotation, and the telescope graticule. The x and y axes are set to zero using the remote controllers.

The stage is now set for the alignment of the neutron collimators. The table is rotated so that the x axis is in line with the neutron beam - the theta axis is now at zero. A standard scan is now run from -3 to $+3$ mm on the x axis. A typical slit setting for this measurement would be 2mm wide by 10 mm high. The intensity from the most intense peak is then summed across the all detectors in the central bank. This provides an intensity figure. These figures are then plotted for both left and right hand collimators using Sigma Plot, and a Gaussian fit is used to establish the position of the collimators with respect to the zero position of the xy table.

Alignment of Incoming Beam Collimation

A similar scan is now performed using the y axis to establish the position of the slit system. Again, if the slit system is shown to be more than 0.1 mm from its central position as an average between the two collimators, then an adjustment is made using the micrometers.

For the purposes of completion of the basic alignment procedure, the alignment of the z axis is now described, although this is usually performed later in the sequence. The iron rod is now mounted horizontally on the positioner. Its horizontal alignment is checked by running the rod from side to side on the translator and adjusting its position until it is seen to be

aligned with the graticule at both ends. The rod is then aligned with the gauge volume at an angle of 45 degrees to the beam. The slits are then removed and replaced to give a 10mm wide by 3 mm high slit. A z scan is now performed, and again the micrometer can be used to adjust the position of the slit to within 0.1mm. This completes the description of the basic alignment procedure used in setting up ENGIN.

4.5 The Gauge Volume & Pseudostrains

When measuring the strain within an engineering component it is essential to know over what region the measurement has been taken. For this reason the *gauge volume* must be well characterised. A detailed understanding of the shape of the gauge volume is also necessary since changes in the shape of the gauge volume can affect the measured value of the strain.

The gauge volume is defined by the intersection between the incoming neutron beam and the space viewed by the radial collimators in front of the neutron detectors (the collimator response function). To calculate the gauge volume a computer model of the collimator has been set up in order to predict the collimator resolution as a function of position. This model enables the performance of the instrument to be predicted and to understand (and to correct for) the strain-free peak shifts that inevitably occur when measuring near surfaces (internal or external).

It is often convenient to consider the volume from which the detected neutrons originate (the gauge volume) to be cuboid with perfectly sharp edges. However even for the simplest of collimation systems, this is an oversimplification. Consider a simple detector and collimation system consisting of just a single detector and two pairs of slits (fig 4.8). Whilst most of the detected intensity originates from the rectangular shaded area, a significant number of neutrons will be detected from the regions of penumbra which surround the central region. It is therefore apparent that the gauge volume cannot be represented by a

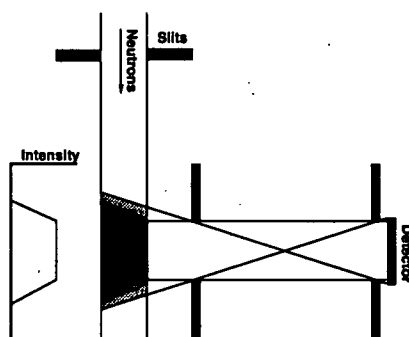


Fig 4.8: The resolution function of a simple, conventional collimation system showing the regions of penumbra. Even in this simple case the gauge volume is not a sharp-edged cuboid.

simple geometrical shape but is instead a distribution - a three dimensional function, the value of which represents the fraction of the detector which can see that point. The name given to this three dimensional function representing the collection efficiency of the collimation and detection system is the *spatial resolution function*.

Most importantly it should be noted that this resolution function is not an instrumental constant but will vary according to the *specimen being measured*. For example if the specimen is a strong absorber of neutrons, the resolution function will be biased towards those areas of the gauge volume for which the total path length of neutrons in the specimen is shortest. An extreme case is where the gauge volume is incompletely filled (as happens when making near surface measurements). Here the spatial resolution function is reduced to zero everywhere the specimen is absent.

This variation of the resolution function with specimen position, shape and material means that the region of the specimen represented by the measured lattice spacing will also vary. *The consequence of this is that the measured lattice spacing may vary as a function of the specimen geometry and material, independent of any residual stresses, if the gauge volume is incompletely filled or filled with a strongly absorbing sample.* These effects are collectively referred to as *geometrical pseudo-strains*. The need to predict and account for this variation of measured lattice spacings means that a detailed model of the behaviour of the detection and collimation system must be made where these effects may be present.

The time of flight is given by:

$$\tau = cd_{hkl}l \sin\theta$$

and

$$\frac{\partial\tau}{\tau} = \frac{\partial d}{d} + \frac{\partial(l \sin\theta)}{l \sin\theta}$$

hence

$$\text{Peak shift} = \text{lattice strain} + \text{pseudostrain}$$

(where d_{hkl} is the lattice spacing, l is the total neutron path length (moderator to detector), and θ is the Bragg diffraction angle).

From the above equation we can see that the measured peak shift has two contributions: the lattice strain, which we are aiming to measure; and the variation of $l \sin\theta$. Were the gauge volume to be a simple point, then $l \sin\theta$ is a constant (for a given scintillator). However in reality the gauge volume has a finite size and the value of $l \sin\theta$ will be different for different points in the gauge volume. The $l \sin\theta$ term in the above equation therefore represents a weighted average of $l \sin\theta$ over the whole gauge volume. The weighting function will be the detected intensity at each point in the gauge volume i.e. the resolution function.

We therefore see that the average value of $l \sin\theta$ of the detected neutrons depends upon the resolution function. We have already seen that changes of absorption coefficient or incompletely filled gauge volumes affect the resolution function; they will therefore cause a change in the average $l \sin\theta$ and therefore the time of flight of the detected neutrons. If this peak shift is not to be mistaken for a change in the lattice parameter, we must be able to predict and thus correctly for it. The term we have used to describe the peak shift due to a change in the average $l \sin\theta$ is a geometrical pseudo-strain.

The computer model that has been developed to calculate geometrical pseudo-strains includes a detailed representation of the geometry of the radial collimator and detectors, and of the specimen itself. It is possible to predict the geometrical pseudo-strains due both to absorption coefficient and incompletely filled gauge volumes. Because the absorption coefficient is almost invariably homogeneous within a specimen, the pseudo-strain is independent of specimen position and represents a systematic error. This error is present in order to calculate the lattice spacings, the measured times of flight are calibrated against a ceria standard. Unless the absorption coefficient of the specimen is precisely the same as that of ceria, the resolution functions will be different and the average $l \sin\theta$ will therefore also differ.

Geometrical pseudo-strains become very important when we are working very close to the specimen surface (a very interesting region for internal strain measurement, see section 5) with an incompletely filled gauge volume.

The collimator model requires a 3D calculation. However, since the z dimension does not affect the diffraction angle in any way, its only effect is upon the intensity and path length; the model can therefore be made simpler by considering first the 2D case and then extending it to 3D.

Fig. 4.9 shows a schematic view of the collimator and detector but includes only a small number of foils and scintillators for clarity. It is not to scale! The point in the gauge volume under consideration is labelled P. In-flight neutrons are shown as shaded areas emanating from P. The fine hairlines represent rays with the maximum and minimum diffraction angles which pass between two adjacent collimator foils. The first step in calculating the illuminated region of the detector is to calculate the equations of these rays.

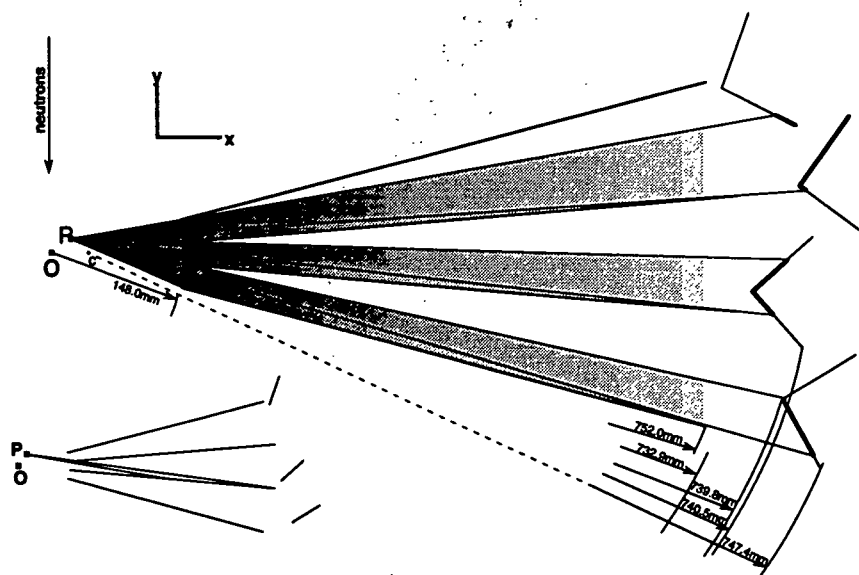


Fig 4.9: Dimensions of the collimator and scintillator elements. The inset shows the case where no neutrons from P are able to pass through the collimator aperture under consideration.

4.6 Prediction of the Collimator Resolution Function

We have seen that the collimator resolution function of the ENGIN instrument is a complicated, three dimensional function and that it is intimately related to the geometrical pseudostrains present in strain measurements. Moreover, this resolution function is itself a function of the specimen geometry and material (specifically the neutron absorption coefficient). When calculating the predicted pseudostrains, the collimator resolution function is not determined directly, but is simply included in the mathematical model. However a direct calculation of the resolution function is important for two reasons. Firstly it is, of course, necessary to know the sampling volume to which the measured lattice spacing relates. Secondly, it enables the theoretically achievable spatial resolution of the instrument to be calculated and compared with the experimentally measured value.

The total intensity detected in all the scintillators was calculated for a square grid of points, P , on the x - y plane. A square grid was chosen in preference to the more usual random array of points as it was more suited to the available graph plotting software. The points were constrained to the x - y plane because the resolution function is a far stronger function of x and y than it is of z . An idealised material, with no neutron absorption was chosen for simplicity as this removes the dependency of the predicted function on the specimen geometry (assuming a full gauge volume). Secondary absorption due to diffraction makes such a material a theoretical impossibility but in practise it is close to the behaviour of materials such as Al and Si.

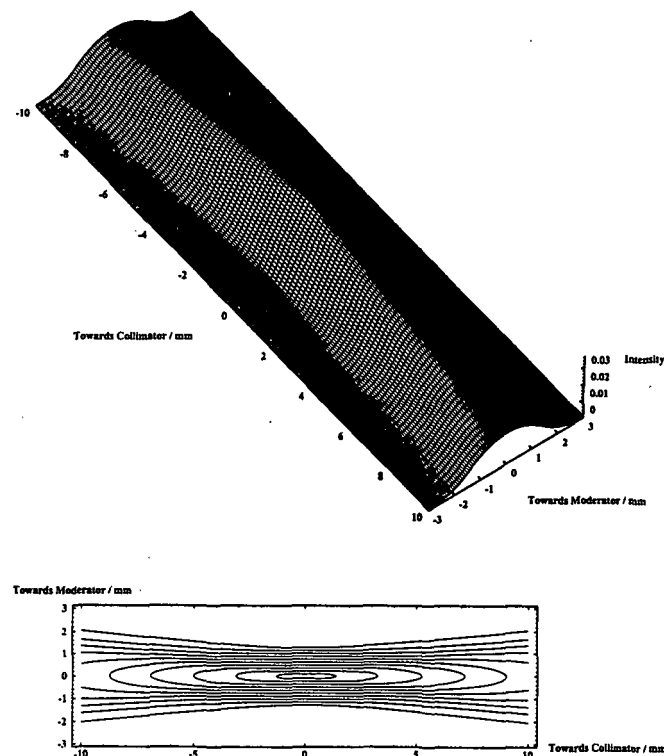


Fig 4.10: The predicted collimator resolution function for a non-absorbing specimen in the plane of the neutron beam. The result is shown as a contour map (equally spaced contours) and a surface.

The predicted resolution function is shown in fig 4.10. It can be seen that it is far sharper in the y direction than it is parallel to x . This is a useful feature since it means that the x

direction of the sampling volume is determined effectively by the width of the incident beam slits (allowing for dispersion) and is not significantly affected by the collimator. The cross section of the resolution function in the y direction (across the face of the collimator) is triangular at the centre, becoming approximately Gaussian a few mm away from the focal point. The FWHM of the resolution function as a function of defocus is shown in fig 4.11

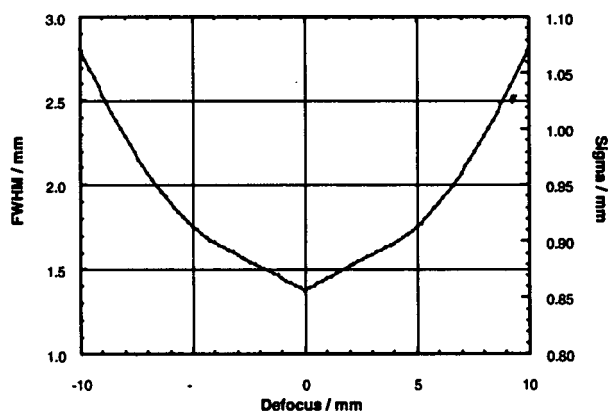


Fig 4.11: The theoretical resolution of the spectrometer as a function of collimator defocus.

The collimators have been mounted with their focal point at the centre of the gauge volume (as defined by the incident beam slits) in order to provide the best possible spatial resolution. However it would also be possible to move the collimators by a few mm in the x direction should it ever be desirable to decrease the spatial resolution of the instrument. This would enable the size of the gauge volume to be controlled in all three dimensions. It is also possible that the collimators could be accidentally misaligned, causing a decrease in the spatial resolution. Whilst the sharpness of the resolution function parallel to the neutron beam makes it relatively straightforward to align the focal points of the two collimators in the y direction, the smoothness perpendicular to the neutron beam makes it very difficult to align the focal points with the centre of the neutron beam. One such installation error has already been noticed and corrected.

4.7 Determining Lattice spacings

The final output from a strain scanning measurement is a map of a lattice spacing (or an average lattice spacing) $d(hkl)$ as a function of position within the component under study. The recorded data from one of the ENGIN detector modules consists of 135 spectra from each of the 135 individual detector elements making up the module.

The process of calculating the lattice spacing map from the raw data therefore takes two steps:

- i) adding the individual spectra together to form a single diffraction pattern (*focusing*)
- ii) calculating the lattice cell size from this diffraction pattern using the Rietveld method.

These steps have been accomplished with the crystallographic data analysis software available at the ISIS facility, which has been modified to automate the processing of large number of measurements.

4.7.1 Automated Generation of Focusing Routines

The purpose of the *focusing* routine is to add together the data from each of the individual detectors, taking account of the difference in $l_T \sin\theta$ between them. The average value of $l_T \sin\theta$ of the neutrons detected in each individual scintillator is calculated by measuring the time-of-flight of the peaks in the spectrum from a calibration specimen, such as silicon or ceria.

With a total of 270 individual detectors in the two detector banks, it is necessary to automate this process using a Rietveld refinement of each individual detector element. Starting from the central scintillator, the program refines the data from each scintillator in turn, calculating the effective path length for that scintillator. These values are then incorporated in the focusing routine.

4.7.2 Refinement of the lattice dimensions

The determination of lattice dimensions from a single phase material using the Rietveld method is generally straight forward and has been described elsewhere. In engineering samples the process may be complicated by texture, the anisotropic effects of stresses or by multi-phase samples.

To avoid the effects of texture, which are often present in engineering samples, a modification of the Rietveld method, known as a Pawley refinement, is used for analysing ENGIN data. The effect of texture is to change the relative intensities of the individual Bragg reflections in the diffraction pattern. A Pawley refinement accommodates these variation by imposing no constraints on the *intensity* of individual reflections, only constraining the peak position to be that defined by the lattice dimensions.

Many interesting materials (both from a scientific and engineering viewpoint) consist of more than one crystalline phase. This presents difficulties when analysing the diffraction profiles since there will be a distinct set of Bragg peaks for each phase present. In such situations it is not uncommon for peaks from different phases to overlap. There are three approaches to the profile refinement of multi-phase materials: ignore the presence of the second phase, eliminate the second phase peaks from the refinement, or simultaneously refine all the phases.

Fig 4.12 compares the first two approaches. It shows the results obtained from the matrix of a quenched Al-SiC MMC plate. The solid line represents the results obtained from a standard Pawley refinement in which the whole profile has been included in the refinement. The dashed line was obtained after filtering out the regions of the diffraction pattern not associated with the Al peaks.

It can be seen that the two sets of data are almost identical (the average difference of 36 refinements was calculated as $6.8 \pm 30 \mu\epsilon$), indicating that attempting to remove second phase peaks in this way is unnecessary.

We therefore conclude that, for the MMC studied, attempting to eliminate the second phase peaks did not affect the results.

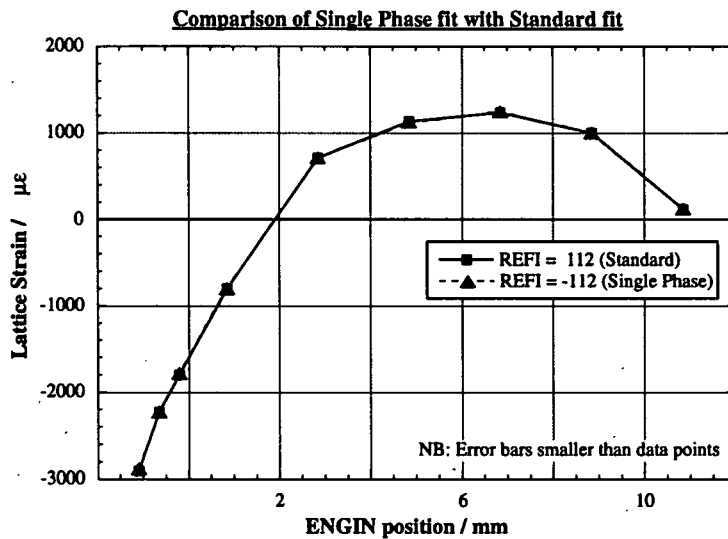


Fig4.12: The residual stresses in the matrix of a quenched Al-SiC MMC plate. There is no discernible difference between ignoring the presence of the SiC diffraction peaks (solid line) and eliminating the peaks prior to the profile fitting process.

4.7.3 Simultaneous refinement of all phases

Experience of multi-phase refinement on data obtained on ENGIN is, at present, rather limited. However early results look very promising. Fig 4.13 shows the results of a multi-phase refinement on a ceramic layer composite, consisting of alternate layers of Al_2O_3 and ZrO . It can be seen that the fitted line is very close to the experimental data, even in regions with significant overlapping of peaks. It should be emphasised that, unlike the Al-SiC data presented above, the data from the ceramic composite proved impossible to analyse using single phase profile fitting. Without the multi-phase Rietveld software, it would have been difficult, if not impossible, to satisfactorily analyse this data using single peak fitting methods.

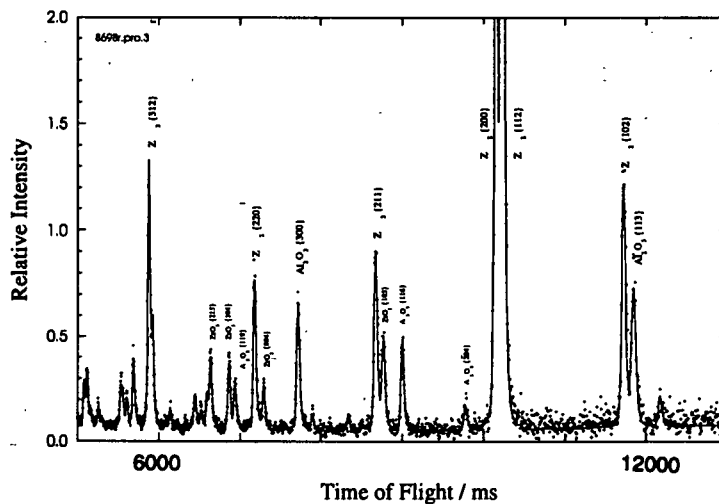


Fig 4.13: Multi-phase Rietveld refinement of an alumina-zirconia layered composite.

4.8 Summary and Conclusions

The resolution function of the new collimation and detection system has been studied experimentally and found to compare very favourably with the original design specification for ENGIN.

The problem of correcting for geometrical pseudostrains (peak shifts which are not caused by changes in lattice parameter) has been identified and a computer program has been written to model the behaviour of the collimation and detection system.

Experimental data has shown that there is a large variation of geometrical pseudostrain between individual scintillators, especially for near-surface measurements. This variation, which is well understood, causes peak broadening and results in a loss of strain resolution. Efforts to model the geometrical pseudostrain for individual scintillators, as a function of specimen geometry and material have been very successful.

The average geometrical pseudostrain predicted by the computer model is in good agreement with that experimentally determined. Therefore we are already in a position to be able to successfully correct for the effects of geometrical pseudostrain, after refinement. The work on separating the lattice strains and geometrical pseudostrains is described elsewhere in this report.

The process of batch refining large arrays of points to build up 1D, 2D or 3D maps of residual strains has been successfully automated. Software now exists to enable the user to quickly and accurately analyse large data sets and the subtleties of its use are well understood.

Software has also been written to simplify the job of the instrument scientist when analysing the calibration runs at the start of each cycle, in order to generate the new focusing routines and instrument parameter file. This software has been shown to produce results as good as, or better than the previous methods, though it is likely there is the possibility of more optimisation, particularly in the choice of refinement procedures.

Multi-phase Rietveld refinement on ENGIN is still in its infancy, but initial results look very promising. If highly textured materials, such as whisker reinforced MMCs, are to be studied routinely then multi-phase Pawley refinement code will have to be written, to complement the existing Rietveld code.

5 Through Surface Measurements

As described in the previous section, measurements of strain in materials near to their surfaces requires the measurements to be corrected for *pseudostrains* which arise from the change in the shape of the gauge volume when it traverses a surface. The objective of this part of the project was to confirm the effectiveness of our corrections by experimentally measuring the geometrical pseudostrains observed when the gauge volume was scanned through the surface of a stress-free specimen.

5.1 Depth of Centroid as a Function of ENGIN position

When making near surface measurements the zero position of the ENGIN positioner does not correspond to the centre of gravity of the material from which the neutrons are diffracted (Wang & Edwards, 1994). It is therefore necessary to be able to relate the position of the ENGIN translation table and the position of the centroid as the surface is penetrated. The computer model of the collimator has been compared with simple mathematical models, as shown below. In most cases the differences were very small so the use of an elaborate model is not usually necessary.

Comparison of different representations of the gauge volume

The shape of the ENGIN gauge volume is the intersection of an approximately rectangular incident beam (assuming negligible beam divergence) with an approximately Gaussian collimator resolution function. The actual function which represents the gauge volume is illustrated in the previous section. Most experiments, however, are not sensitive to the precise shape of the gauge volume. In such cases it is acceptable to model it as a cuboid.

The incident beam collimation defines two of the dimensions and the width of the gauge volume parallel to the incident neutrons is taken to be 1.4mm, the FWHM of the resolution function. Using such a model, the position of the centroid was calculated as a surface at 45° to the incident neutron beam (the standard diffraction geometry) was scanned through the gauge volume. A comparison with a cubic (2x2x2mm) gauge volume and the more detailed computer model of the gauge volume was also made to investigate how critical is the choice of model used to describe the shape of the gauge volume.

Fig 5.1 shows the predictions of the position of the centroid for the three models. It is clear that failing to account for the shifting of the centroid can lead to serious errors for measurements < 1mm from the surface. This is shown by the deviation from the straight line in fig 5.1. This shows that measurements made with the focal point of the collimator less than 1mm from the surface, will underestimate the depth at which the strains are measured. It also means that provided corrections can be made for surface effects, it is possible to acquire data at distances many times less than the width of the nominal sampling volume.

It is apparent that there is little difference between the models, the maximum error in the centroid position being around 0.1mm. In most circumstances this difference between the models will be unimportant. However where more accuracy is required, for example for measurements of plasma sprayed coatings which are only 300µm thick, this difference is significant. In such cases, it may be necessary to use the more detailed computer model of the gauge volume.

It can also be seen that, when considering the position of the centroid, a $\langle \text{slit width} \rangle \times 2.0\text{mm}$ rectangular gauge volume is a better representation than a $\langle \text{slit width} \rangle \times 1.4\text{mm}$ rectangle and should probably be used in calculations. This is not to say that the dimensions of the gauge volume *are* cubic, but that when using a simple rectangular representation of the gauge volume, one should use a rectangle wider than the FWHM of the true resolution function.

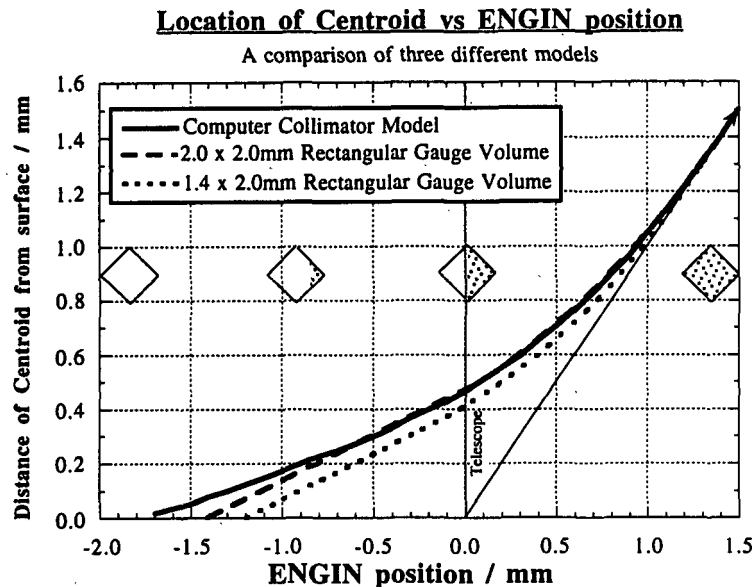


Fig 5.1 Position of the centre of gravity of diffracting specimen for a non-absorbing material ($\mu=0$), as a function of position of the ENGIN positioner. The thin line represents no correction for centroid shifting. The position of the centroid is a good representation of the depth at which the strain field is sampled. A 2mm wide incident beam was assumed in each model.

5.2 The Effect of Slit Width on Centroid Position

The effect of slit width on the conversion from the position of the ENGIN translator to the position of the centroid will be greatest when the only a fraction of the gauge volume is occupied by diffracting material. However there will also be small effects, even when the gauge volume is totally full, due to the absorption of the material. Fig 5.2 shows the centroid position as a function of the incident beam slit width. For reasonably small gauge volumes, we see that there is less than 0.2mm variation in the position of the centroid. The material modelled is iron, which is a fairly strong absorber of neutrons. For larger gauge volumes, there can be up to 0.4mm difference, though this is still a small fraction of the overall size of the gauge volume.

5.3 The Effect of Absorption Coefficient on Centroid Position

When the gauge volume is only partially filled, absorption will have little effect on the position of the centroid because all the neutrons are diffracted from near the surface of the specimen. However, for a fully filled gauge volume, the centroid will be nearer to the surface of the component due to the absorption. Fig 5.3 shows this in more detail. For most materials studied, the shift is small, being around 0.2mm for Ni (assuming a 2mm wide

incoming beam slit). For steel, with 2mm wide slits, the difference is ~0.1mm, which is the same order as the positioning accuracy for normal use.

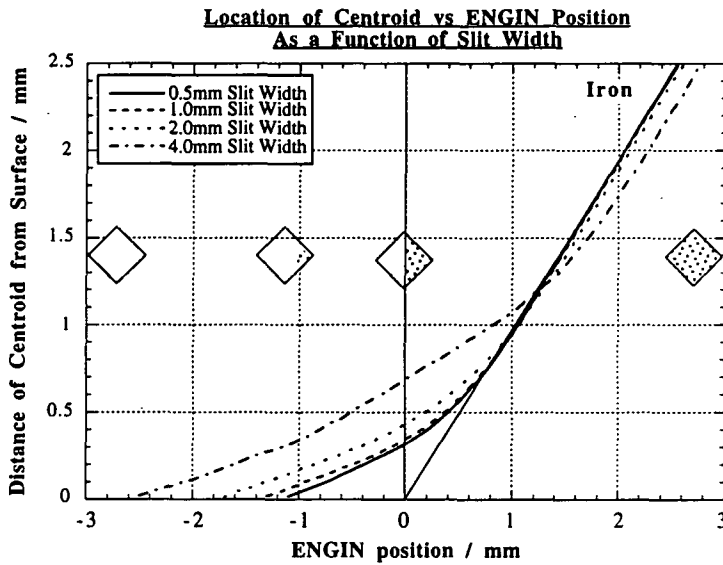


Fig 5.2: Position of the centroid in Fe as a function of the incoming slit width (Fe specimen - $\mu=0.118 \text{ mm}^{-1}$)

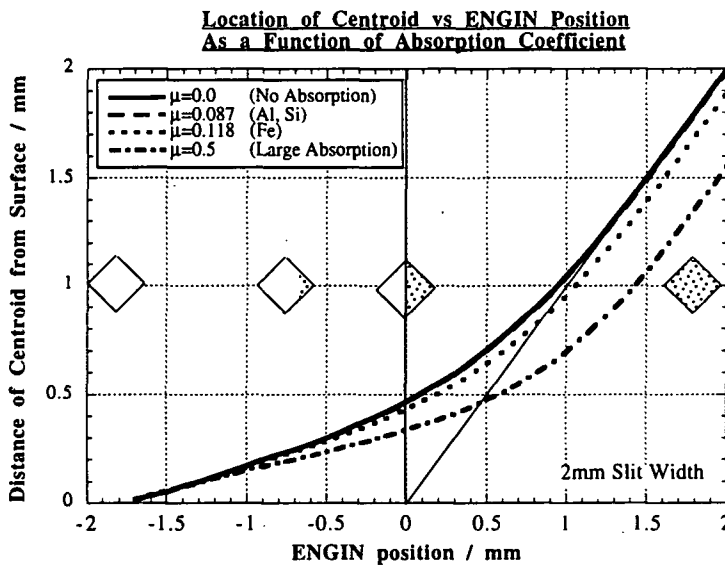


Fig 5.3: The effect of the neutron absorption coefficient on the position of the centre of gravity of the detected neutrons for a 2mm wide incident beam slit.

5.4 Lateral shift of the centroid

Because the gauge volume is not square and penetrates the surface from one corner, there will be a slight lateral shift (i.e. parallel to the specimen surface) of the centroid as the corner enters the specimen. This is shown in fig 5.4. As expected, a square gauge volume does not show any lateral shift of the centroid. The 1.4mm wide rectangular gauge volume shows a shift towards the detector, since the corner which first enters the gauge volume is closer to the collimator. The computer model, however, shows the opposite effect since the maximum width of the resolution function is approximately 2.8mm, so the first part of specimen to enter the gauge volume is below that point which will eventually be at the focal point of the collimator. The insets of fig 5.4 help to explain this pictorially.

The maximum lateral shift is around 0.3mm. This should therefore be born in mind if the exact position on the surface of the specimen of the measurement is critical, though it is likely that in this case, a smaller gauge volume would be used.

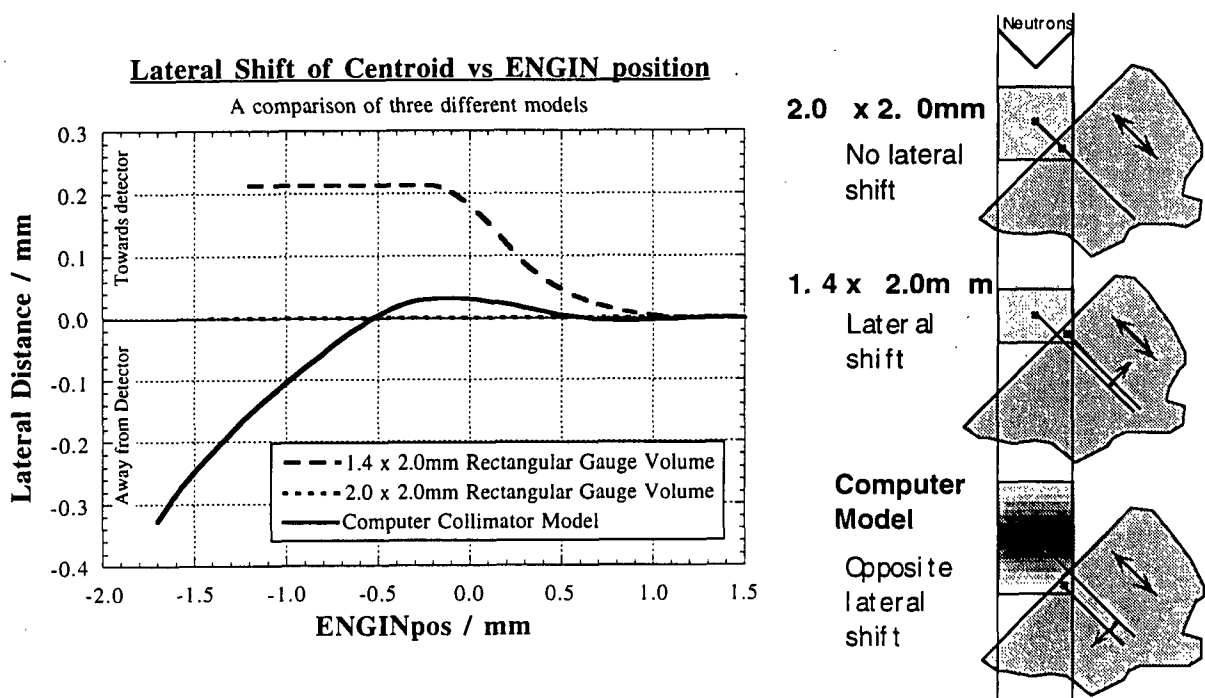


Fig 5.4 The lateral position of the centroid can vary by up to 0.5mm depending on the shape used to represent the gauge volume. (2mm incident slits)

5.5 Modelling the Shadowing effect on the Detectors

When the gauge volume is only partially filled, the focusing collimator foils cause the detectors to be incompletely illuminated, as shown in Figure 5.5. As a result, the profile recorded on each detector is shifted, and this can affect the overall position of the peak when the profiles from all the detectors are combined. This will result in a contribution to the calculated lattice strain which is not related to any residual stresses. Unless we correct for these "geometrical pseudostrains", the measured lattice strains will be in error for near-surface measurements. It is possible to predict and account for this effect using the computer model of the collimator described elsewhere in this report.

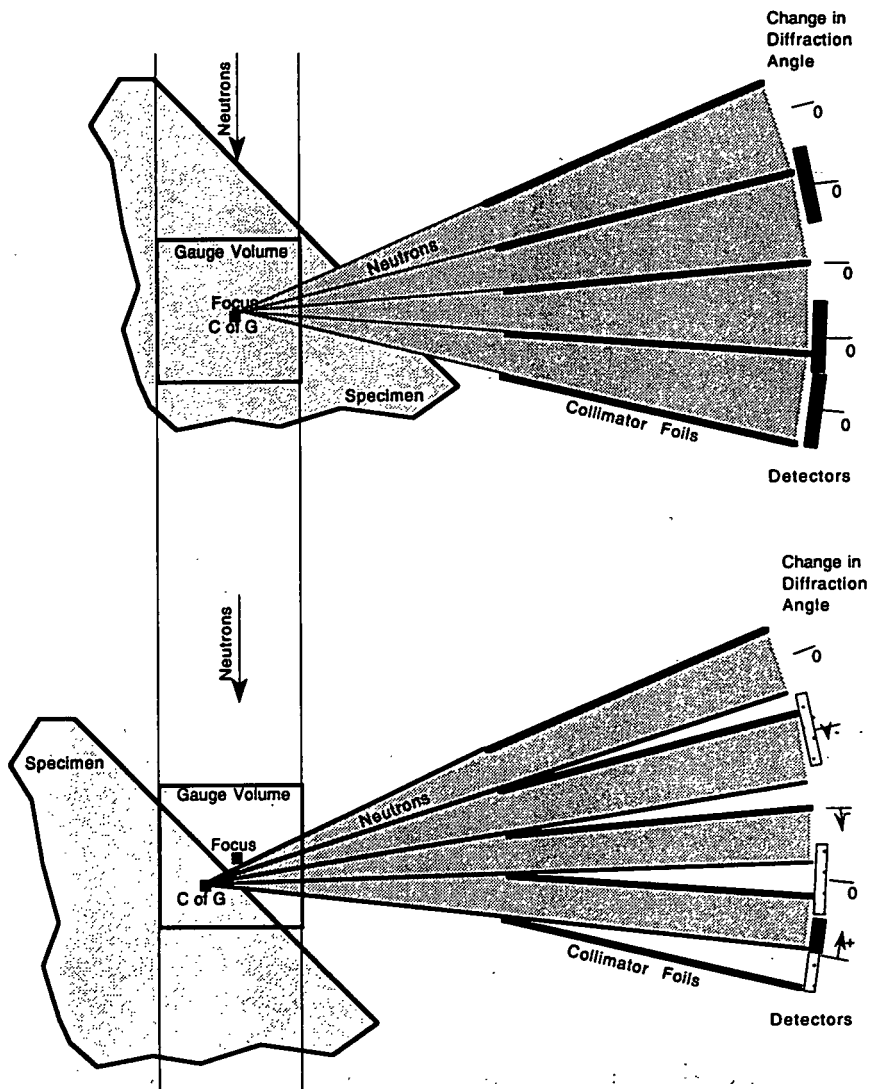


Figure 5.5 Schematic illustrating the shadowing effect caused by the collimating foils when the gauge volume is only partially full. This causes the peak profiles for each detector to be shifted differently and will, if not corrected for, result in a shift in the overall peak position.

5.6 Predictions of Near Surface Detected Intensities

Fig 5.6 shows the detected neutron intensity as the specimen surface is scanned into the gauge volume, as a function of the absorption coefficient. As expected, the larger the absorption coefficient, the closer the position of maximum intensity is to the surface. Or course, in order to most accurately locate the surface, it is best to concentrate on the rising slope of the graph, rather than trying to accurately find the position of the maxima amongst random noise. Note that the horizontal axis of the graph is the position of ENGIN, rather than the centroid since this is more useful when finding surfaces using surface scans.

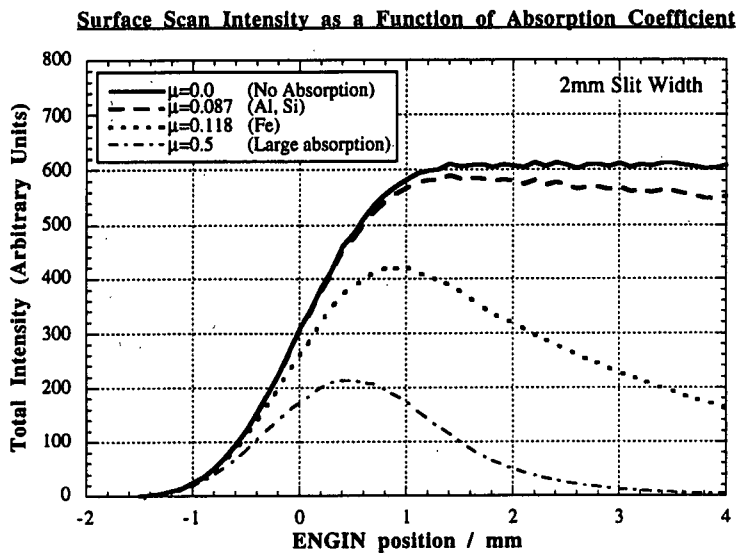


Fig 5.6: Variation in detected intensity as function of absorption as the specimen surface is scanned through the gauge volume. Unless the absorption coefficient is zero, the intensity decreases as the gauge volume is moved deeper into the specimen due to the increased neutron path length.

Fig 5.7 shows the effect of varying the slit width on the surface scan intensities. It is useful to note that the intensity when the surface goes laterally through the focal point of the collimator is approximately a constant fraction of the maximum intensity. This fact may therefore be used as a reasonable indicator of the surface position, when time does not permit the use of a full least squares fitting procedure.

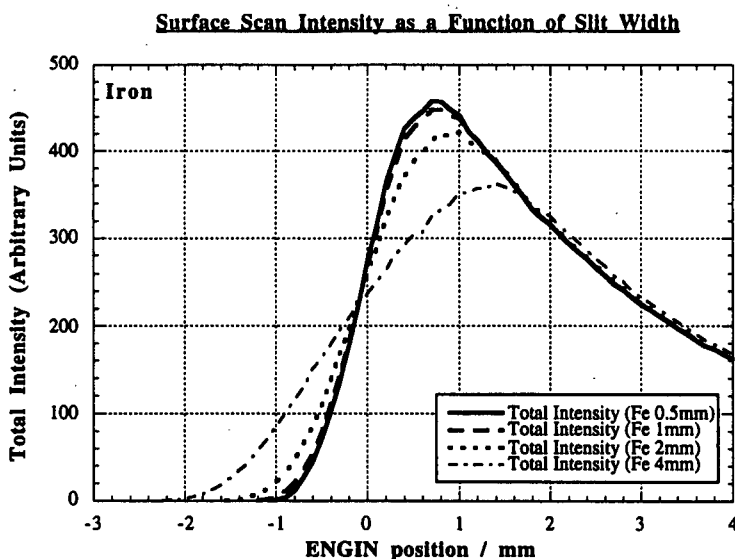


Fig 5.7: The effect of using different width slits to define the incident beam upon the intensity of a surface scan.

5.7 Predictions of Geometrical Pseudostrains

Because the computer model of the collimator and detector allows us to calculate the average value of $l \sin \theta$ for the detected neutrons, we can also use it to predict the geometrical pseudostrains which result from a gauge volume which is not completely filled with diffracting specimen. Although the collimator computer model does not predict the detector by detector response precisely, the predicted intensities and strains, when averaged over all the detectors, both agree well with experiment. The detector-by-detector differences lie in the period of the geometrical pseudostrains as a function of detector number, rather than their average amplitude. The results presented here are therefore considered accurate.

The average value of $l \sin \theta$ is calculated for each detector in turn, both for the specimen geometry being modelled and for an 11mm diameter cylinder with $\mu=0.0083\text{mm}^{-1}$ representing the silicon run. The average fractional change of the values of $l \sin \theta$ is then calculated and returned as the average pseudostrain. This is a direct analogy for what happens during focusing. The switch from silicon to ceria as the standard sample for the creation of focusing routines may have some very small effect upon the predicted strains due to having slightly differing absorbencies. Of course, in practice, if the experimental strains are being calculated by reference to a measured d_0 specimen, *the effect of the difference in absorption coefficient will be cancelled out.*

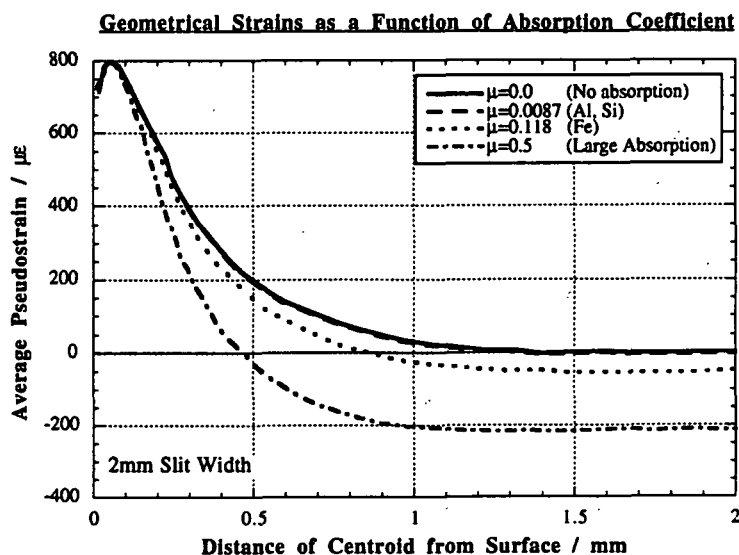


Fig 5.8: Geometrical surface strains as a function of absorption coefficient. Clearly, were such pseudostrains to remain uncorrected, large errors would be incurred when attempting to measure within 0.5mm of the surface.

Figure 5.8 shows the effect that the absorption coefficient has on the geometrical pseudostrains. It can be seen that there is little difference between the results, provided the absorption coefficient remains low. For abnormally absorbent specimens, there can be up to $200\mu\epsilon$ difference in the pseudostrains. The asymptotes of the graphs show that, for an iron specimen, even when the gauge volume is totally immersed in the specimen, there will be a $50\mu\epsilon$ pseudostrain caused by the difference in absorption coefficient between iron and ceria.

Fig 5.9 shows the effect on the predicted pseudostrains as a function of slit width. As expected, the pseudostrains are larger for large gauge volumes since the distances between the centroid and the focal point are larger. Provided the position of the surface is well known, this graph allows the correction of the raw data to obtain the true elastic strains.

The downturn of the pseudostrain when the gauge volume is less than 0.2mm from the surface is due to the fact that the predicted intensity in some of the detectors becomes zero. Not surprisingly, it is recommended that anyone wishing to make measurements very close to the surface should use a small slit width and should look carefully at the detected intensity in each detector.

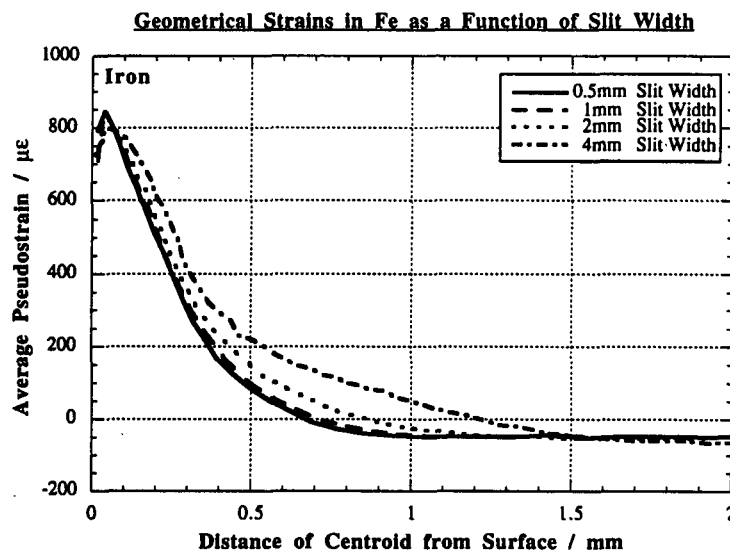


Fig 5.9: Geometrical surface strains as a function of slit width

5.8 Vertical and Horizontal Surface Scans

The above graphs all consider the case where a specimen is scanned through the gauge volume in the x-y plane. However, it is also possible to scan the specimen vertically through the gauge volume. In this case, the average angle of diffraction of the detected neutrons will not vary as the specimen is moved. The average path length will vary very subtly, but not enough to cause any measurable pseudostrains.

5.9 Experimental Measurements at Surfaces– A Quenched MMC Plate

A section of a quenched metal matrix composite plate was studied using ENGIN. This specimen has previously been measured at ISIS by Fitzpatrick (Fitzpatrick, 1995) and elsewhere by Hutchings (Hutchings, 1993). Previous measurements have always been restricted to being at least 1.5mm within the specimen to eliminate the need for surface corrections. In the recent study, however, measurements were made to within 0.33mm of the surface. Since the residual stress distribution is expected to be parabolic through the thickness of the plate, the near surface region is the most interesting as it is here that the highest stresses are to be found. This is important from a technological viewpoint as such stresses will inhibit fatigue crack growth in service.

The specimen studied was designated A695/11 and was made from BP217 MMC, manufactured by BP Metal Composites (now Aerospace Metal Composites). It consists of an Al 2124 matrix with 20wt% particulate SiC with an average initial particle size of $\sim 45\mu\text{m}$. The composite billets were formed by a powder route involving HIPping at $\sim 100\text{MPa}$ and $\sim 500^\circ\text{C}$. They were then forged at $\sim 400^\circ\text{C}$ and hot rolled to a thickness of 14.5mm. The specimen was solution treated at 505°C for one hour, followed by a cold water quench. It was subsequently naturally aged for $>1000\text{hr}$ before machining into a 14mm square, 100mm long test specimen. The geometry of the test specimen is shown in fig 5.10.

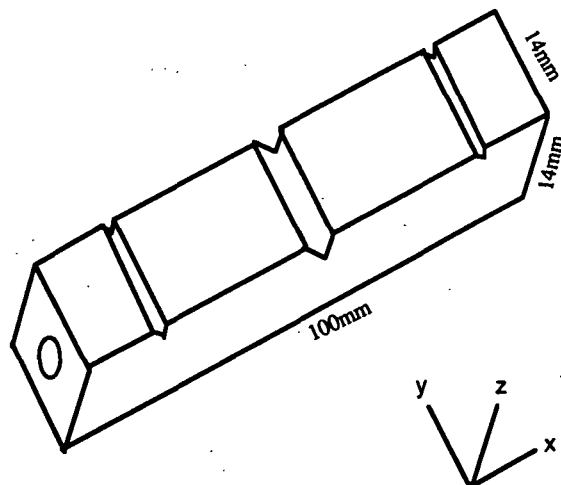


Fig 5.10: A695/11 bend test specimen geometry

5.9.1 Measurements

Two allocations of beam time (totalling 76h) were used in measuring the specimen. In the first, the specimen was held horizontally to measure ϵ_x and ϵ_z . The surface was scanned through a 10mm high x 2mm wide gauge volume by translating the y axis of the ENGIN positioner, therefore these measurements are referred to as the "Y Scan". Note that this refers to the positioner co-ordinates, not the specimen co-ordinates. In both experiments, the strains were measured as a function of z, the through thickness direction.

In the second experiment, the specimen was mounted horizontally, so that the two "in-plane strains" ϵ_x and ϵ_y were measured. The surface of the specimen was scanned through a 10mm wide x 2mm high gauge volume by moving the z axis of the positioner so these measurements are referred to as the "Z Scan".

The focused data was refined one phase at a time, with the REFI card set to -112 (rather than 112). This allows the Rietveld program to ignore peaks which do not belong to the phase being refined. The results are shown in figs 5.11 and 5.12.

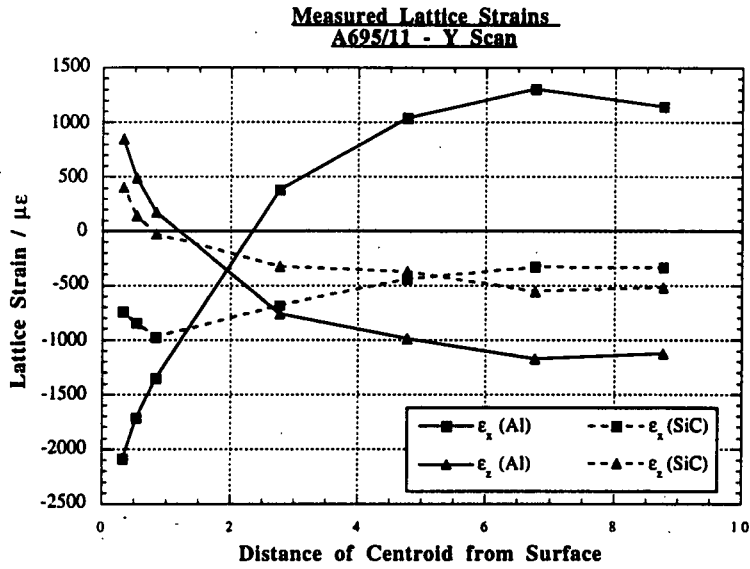


Fig 5.11: Measured residual strains in a quenched MMC plate. Note how the geometrical pseudostrains cause all the curves to move in the tensile direction as the surface is approached.

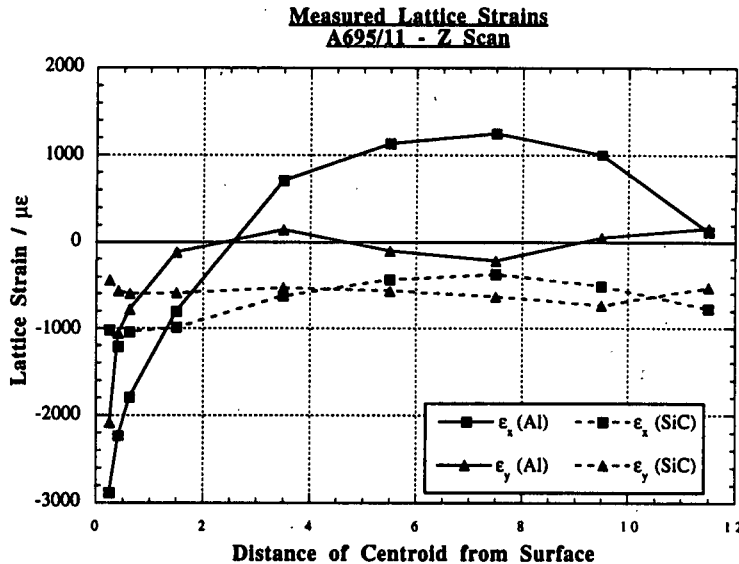
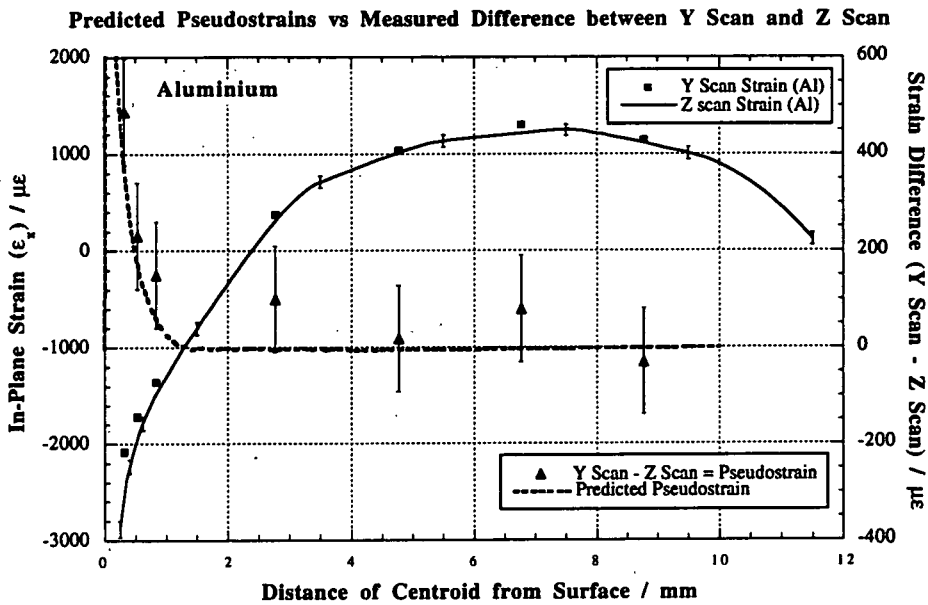


Fig 5.12: Measured residual strains in a quenched MMC plate. Note the absence of geometric "pseudostrains" near the surface.

5.9.2 Surface strains (i) - comparison of strains in x direction

The residual strains in the x direction were measured in both the Y scan and the Z scan. Since the geometric pseudostrains arise from a change in the average diffraction angle as the surface moves through the gauge volume, there should be no pseudostrains when the specimen is scanned vertically, since the average diffraction angle remains constant. The difference between the two sets of measurements therefore provides a means of testing the modelled geometric strains.

Figs 5.13 and 5.14 show the measured lattice strains (ϵ_x) for types of scan. The difference between the Y Scan values and a smooth fit drawn through the Z Scan measurements represents the induced geometric pseudostrain. The pseudostrains predicted by the computer model are represented by the dotted line. There is excellent agreement between model and experiment, and represents a positive validation of the computer model.



5.13: Comparison between modelled and experimentally measured pseudostrains for the Al phase in A695/11 MMC

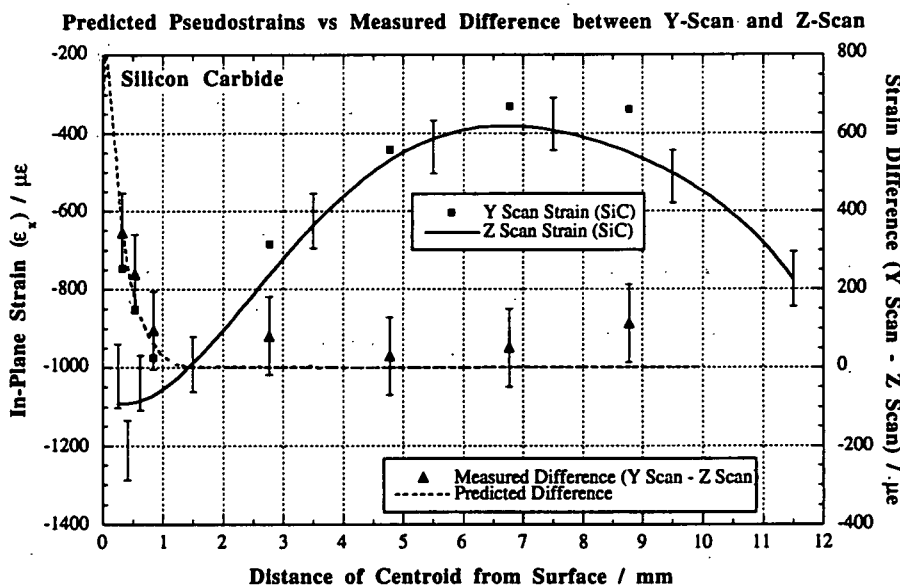


Fig 5.14: Comparison between modelled and experimentally measured pseudostrains for the SiC phase in A695/11 MMC

5.9.3 Surface strains (ii) - Correcting for the geometrical pseudostrains

The surface pseudostrains in the x direction have been shown to be accounted for by the computer model with great accuracy. Of course it was not possible to measure the strains in the z direction using a Z scan. Even if it were possible to measure surface strains perpendicular to the surface using this method, as well as those in the plane of the surface, there would still be a need to predict geometrical pseudostrains. This is because for Z scans,

a wide incoming slit is often necessary to obtain reasonable run times. In contrast to the high incoming slit frequently used for Y scans, a wide slit averages the strain over a large area in a direction in which the strain is often varying significantly.

Because of the good agreement between the predictions of the computer model and the difference between the two sets of measurements, we are now in a position to subtract the predicted geometrical pseudostrains from the measured data to deduce the residual elastic strains in the specimen, to within 0.33mm of the surface. These results are shown in fig 5.15. It can be seen that, after correction, the values are much more reasonable. The sharp upturn in the residual strain distribution has been completely eliminated and the results are much more like what we would expect the stress distribution within a quenched plate to look like.

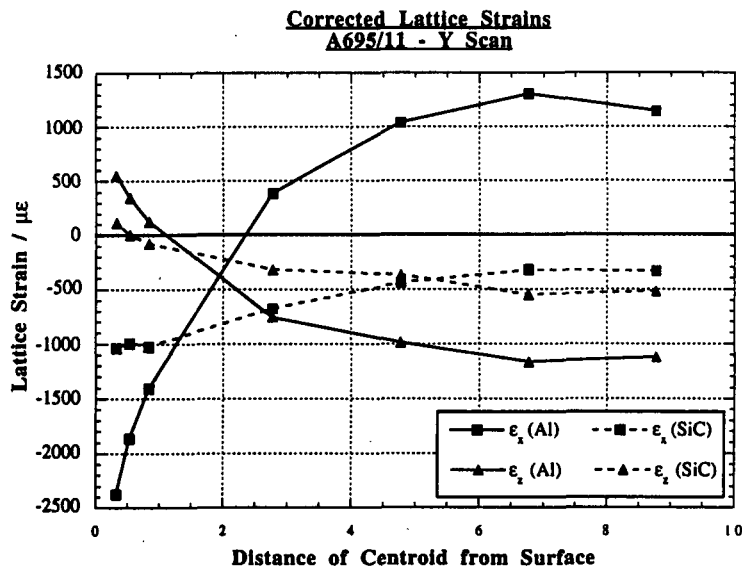


Fig 5.15: Residual elastic strains in A695/11, a section machined from a quenched MMC plate. The measurements near to the surface have been corrected for the effects of geometrical pseudostrains.

5.10 Conclusions

There are two causes of pseudostrains on scanning through a surface; i) movement of the sample centroid, ii) shadowing of the detectors by the collimating vanes. Both of these effects are present in 'Y scans' but, as we have shown, these effects can be corrected using suitable modelling techniques. Both effects can also be removed by performing 'Z scans', which do not give rise to pseudostrains.

6 Intergranular Stresses

The objectives of this part of the project were:

- to interpret the elastic strains shown by individual peaks in terms of macrostresses in the elastic region (i.e. to take account of elastic anisotropy)
- to interpret the elastic strains shown by individual peaks in terms of macrostress history in the plastic region (i.e. to take account of plastic anisotropy)

The experiments used to investigate anisotropy divided into those designed to measure the elastic anisotropy and those designed to measure the elastic microstrains caused by anisotropic plastic deformation i.e. the plastic anisotropy. Because elastic anisotropy is already well understood, most of the effort was targeted at measuring the effects of plastic anisotropy.

6.1 Measurement of elastic anisotropy

Different crystallographic planes exhibit different stiffnesses when loaded. Therefore, the strains calculated by measuring peak shifts will be different for each peak. The effects of elastic anisotropy are largely well understood and the current Rietveld program includes a term for cubic elastic anisotropy in the refinement.

Neutron diffraction is an ideal tool for the study of anisotropy since each diffraction peak corresponds to a specific relationship between the applied stress and the crystal lattice. The use of the ISIS spallation source means that many diffraction peaks (and hence lattice orientations) are measured simultaneously. If the Rietveld fitting programs are to be used to greatest effect, more needs to be known about the influence of anisotropy on internal stresses. The influence of elastic anisotropy in producing inter-granular stresses under load has largely been explained [Kroner 1967]. However, although the influence of texture has been taken into account [Sayers 1983], some work still needs to be done in this area.

Three cubic materials of differing elastic anisotropy (A) were chosen for preliminary analysis: aluminium ($A=1.3$), ferritic steel ($A=3$) and austenitic stainless steel ($A=2$). For each, a specimen was loaded in-situ and oriented with respect to the neutron beam so as to diffract the neutrons from planes perpendicular to the length of the specimen, so that the strains parallel to the load direction could be calculated using a number of diffraction peaks.

The Rietveld program has been checked against measurements obtained using the 'GEC' program for Genie. It is far more robust than GEC, allowing fits to be made on smaller peaks and giving generally greater accuracy when used to fit single peaks.

Fig 6.1 shows results obtained from an annealed mild steel specimen. The specimen was loaded in tension and measurements taken at a number of different elastic strains. The diffraction elastic constants (the compliance shown by a given peak) were calculated for a number of peaks and then plotted as a function of the cubic elastic anisotropy factor A_{hkl} (fig 6.2). The gradient of this line represents the anisotropy of the material. Expressed as a fraction of the {100} stiffness, we get a (dimensionless) measure of anisotropy of 1.14.

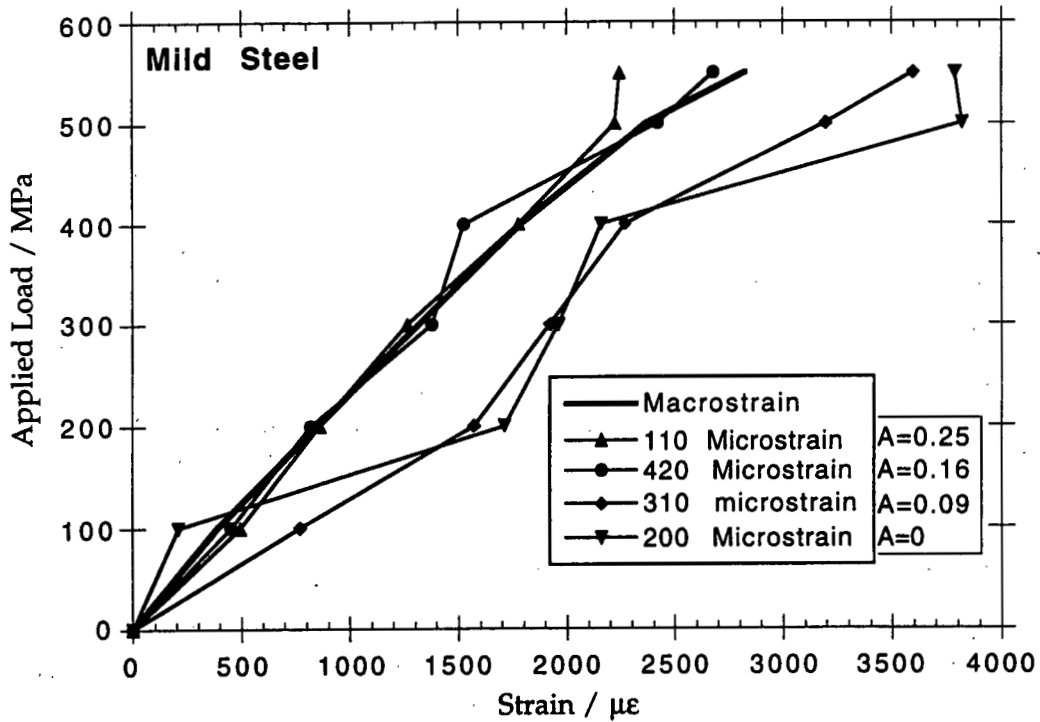


Fig 6.1: The lattice strains exhibited by different peaks as a function of the applied load, compared with the macroscopic response as measured by a strain gauge. The cubic anisotropy factors for the different peaks are also shown.

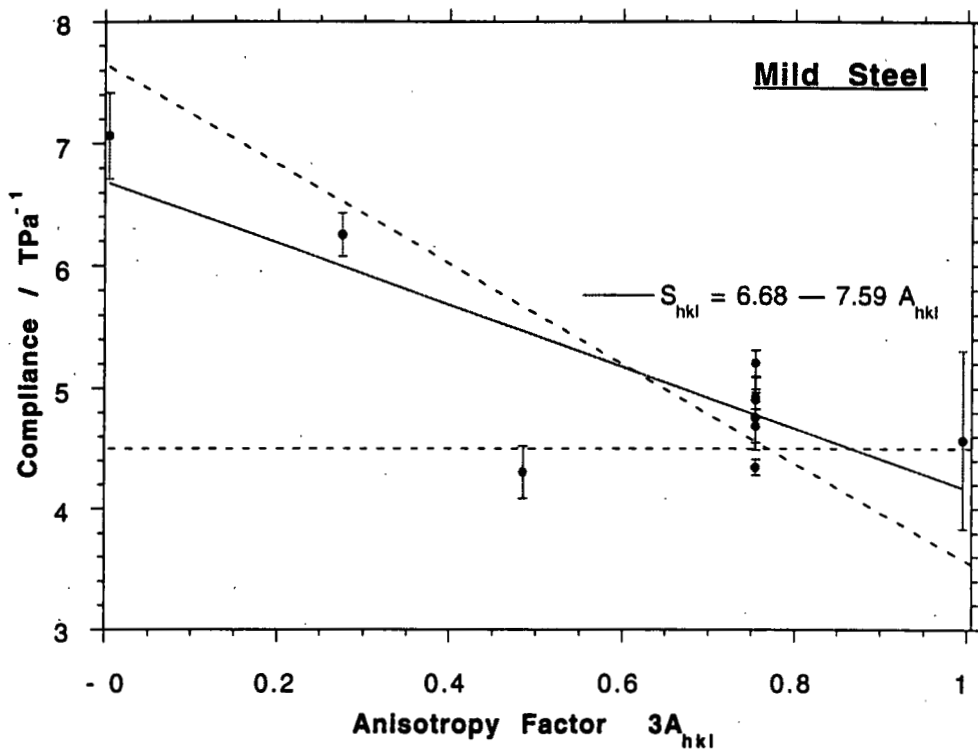


Fig 6.2: The compliances shown by different peaks, plotted against the cubic anisotropy factor. The dotted lines represent the Reuss and Voigt upper and lower bounds.

Rietveld refinement produced a value of 1.15 from analysing a single diffraction profile, showing the power of using this method. In future, the coefficient of elastic anisotropy will be included as a constant rather than refined to reduce the number of variables in the least squares and thereby increase the reliability of the results.

6.2 Measurement of plastic anisotropy in Cu-Zn alloys

6.2.1 Introduction

Anisotropic materials are difficult to analyse, because the measured lattice strains vary as a function of the Bragg peak. Superimposed on the long range (type I) residual stresses are grain scale (type II) residual stresses, caused by the anisotropy of the elastic and plastic deformation behaviour of the material. In the diffraction pattern, these type II residual stresses cause different peak shifts for the different Bragg peaks. If we are to determine the peak shifts due to the long range residual stresses, we must be able to subtract the peak shifts caused by type II residual stresses.

When measuring residual strains using single peak analysis from only one peak (such as when using reactor sources), the correction for anisotropy is difficult since there is no way to measure the variation in peak shift between peaks. Because elastic anisotropy is well understood, it is easily corrected for. The compliance exhibited by any particular peak may be calculated from the single crystal elastic constants, so the effect of elastic anisotropy is taken into account when converting from strain to stress. Elastic anisotropy is already automatically taken into account during profile refinements, if required. Plastic anisotropy, on the other hand, is less well understood so, for materials where it is considered important, the usual approach is to select a peak which is known to be relatively unaffected by the plastic anisotropy, that is its applied-stress/elastic-strain curve is linear. The peak usually chosen for FCC materials is the {311} peak.

Much work on modelling anisotropic plastic yielding has been carried out for many years. However, most of the effort has been devoted to texture prediction in FCC metals [Leffers 1992]. We find that the behaviour of the material is dependant on the stacking fault energy (SFE). Materials with a high stacking fault energy closely follow the Taylor model of plastic deformation and develop a "copper texture" when rolled, whereas materials with lower stacking fault energies are more closely described by the modified Sachs model and develop a "brass texture" when rolled. Computer simulations of the deformation of FCC metals suggest that the intergranular residual stresses should also vary between the high SFE Taylor model and the low SFE Sachs model. Broadly speaking, materials with a lower SFE are expected to exhibit higher intergranular stresses [Pedersen 1987].

Profile refinement produces a single lattice parameter representative of the gauge volume, together with other parameters describing the peak width and the anisotropy of the material. Because the results from profile refinement represent an average behaviour of all the diffraction peaks in the diffraction profile, the situation when dealing with plastically anisotropic materials is better. This is because we expect the average behaviour of the different peaks to be close to the macroscopic response of the material. Therefore, when analysing plastically anisotropic materials on ENGIN, it is far better to obtain an average over all the peaks using profile refinement, than to use a single peak fit, which represents a very small fraction of the detected neutrons.

A better understanding of plastic anisotropy would enable more accurate and representative profile refinements to be carried out and, when using a reactor source, would enable any peak to be used to calculate the residual stresses, rather than being restricted to the {311} peak.

The remainder of this section describes the progress of an ongoing set of experiments to investigate the effects of plastic anisotropy in Cu-Zn alloys (α -brasses) in the range 0 to 20% Zn. This alloy system was chosen for a number of reasons:

- Both Cu and Zn have large coherent neutron scattering cross-sections ($\sigma_c=7.26$ barns for Cu), so measurements can be made in a relatively short timescale. This is important since the data must be good enough to be able to carry out single peak fits on as many peaks as possible.
- The neutron absorption coefficient, μ , is reasonably low (0.811cm^{-1})
- In the range of Zn content used here, the Cu-Zn system is single phase. This is essential as the effects of a second phase material with significantly different mechanical properties could dwarf the effects of plastic anisotropy.
- The crystallographic structure of α -brass is FCC. This is much more easily analysed than BCC or other systems as there is only one set of slip systems operating – {111}<110>.
- The stacking fault energy as a function of composition is well known.
- Despite the relative softness of the material, the elastic strain at yield, after work hardening, is sufficiently high that large residual stresses are expected.
- The component metals have relatively low melting points and are easy to melt, cast and machine.
- The induced radioactivity of the material has a half life of only a few days so specimens can be taken back to the laboratory after measurement. (The induced radioactivity, and the half-life of another possible alloy system – Ni-Co - was much higher was rejected on these grounds).

6.2.2 Specimen Fabrication

Once an alloy system had been selected, the first step was to develop a processing route by which specimens could be produced repeatably, with controlled grain size, limited dendritic coring and near-random texture.

Initial experiments were based around sand casting reasonably large (20x20x150mm) blocks of alloy which could then be sectioned and specimens machined. However, whilst this approach worked adequately for pure Cu, the addition of Zn made the molten alloy more viscous and large scale porosity was caused. The approach was also not particularly repeatable, since indeterminate amounts of Zn vapour was lost into the atmosphere. A much more controllable method was therefore needed.

The fabrication sequence finally selected was as follows. Pure (99.9%) Cu and brass were machined into 15.5mm diameter rods and placed into a 16mm diameter quartz tube which is then evacuated and sealed under 0.05atm argon. This tube is then placed inside a stainless steel safety tube and put in a horizontal tube furnace at 1200°C. The steel tube protects people and furnace in the event of a tube implosion. The tube is left in the furnace for 30 mins in order to ensure the metal is completely molten. The tube is agitated in order to aid the mixing of pure Cu and Cu+Zn, ensuring a constant composition from one end of

the specimen to the other. The tube is then removed from the furnace into an upright position and allowed to cool in air.

Initial experiments used pure Zn along with the pure Cu. However, problems with large scale porosity were experienced. It is believed that this is due to the high vapour pressure of the Zn (the boiling point of Zn is above the melting point of Cu). Replacing the Zn with a high Zn content brass reduced the large scale porosity to tolerable levels.

The result of this initial stage is a specimen with significant porosity on all scales. The material is then machined back down to 15.5mm and remelted in an induction furnace. This reduces the macroscopic porosity and the turbulent mixing caused by the magnetic field ensures good chemical homogeneity on the cm scale. However, the resulting microstructure is dendritic, with up to 2% difference in Zn concentration from the centre of a dendrite to its edge. The scale of the dendrites is typically ~100µm.

In order to ensure chemical homogeneity on the scale of the grains, the material is now homogenised at 900°C for 50h. Using a simple model for diffusion :

$$x^2 = Dt$$

where

x = Distance diffused

D = Diffusion Constant for Zn in Cu at given Temperature

t = Time taken

we calculate that 7h at 760°C should be adequate for the excess concentration of Zn at the dendrite edges to diffuse half the dendrite spacing and equilibrate the chemical composition. However, EDX measurements taken after 24h at 760°C show that the effect upon the dendrites is minimal. For this reason homogenisation is carried out at the much higher temperature of 900°C for up to 50h. Such a large safety margin has the advantage that variations in dendrite spacing due to different compositions or cooling rates will not matter although it does have the disadvantage that oxidation becomes a real problem so precautions are taken to reduce the supply of oxygen to specimens (a vacuum furnace of the required size was not available).

The material at this stage has acceptable levels of porosity and is chemically homogeneous, but the grain size is too large to be used in neutron diffraction experiments. A sequence of cold working, followed by recrystallisation is therefore necessary. Initial experiments with cold working involved uniaxial forging of the rods using a hydraulic press. However, it was found that the deformation patterns induced by such action were not sufficiently homogeneous and there was significant variation of grain size over the cross section after recrystallisation (Hough, 1995). It was also very difficult to achieve repeatable results, due to the coarse control over both specimen alignment and degree of deformation on the available equipment. We therefore moved to cold swaging as a means of deformation.

Swaging not only produces specimens with more homogeneous deformation patterns, it also produces cylindrical specimens of a precisely controlled diameter, resulting in less wastage during machining. The final diameter of the swaging process was chosen to be 11mm, to allow easy manufacture of Hounsfield "D" specimens. The porosity of the material was also found to have decreased after swaging. It was suggested that porosity could be reduced still further if an initial sequence of hot swaging was carried out prior to the cold swaging. However swaging from an initial temperature of 600° was found to have little or no effect upon the porosity so the idea was abandoned.

Recrystallisation was carried out at 500°C, since this provides a uniform grain size of ~50µm and an asymptotically low hardness of 50VHN (Hough, 1995).

At lower recrystallisation temperatures the grain size is smaller, which is advantageous as it results in more grains in the gauge volume and hence better statistics. However, the hardness begins to increase rapidly, indicating that not all the cold work put in during swaging has been relaxed. Since the experiment measures the peak positions as a function of plastic deformation, it is necessary to start with fully annealed specimens. At higher temperatures than 500°C, no reduction of hardness was observed, although the grain size increased. It was therefore decided that 500°C is the optimum recrystallisation temperature.

After recrystallisation, the specimens are machined into standard Hounsfield 'D' specimens with a diameter of 7.14mm (nominal). This allows a beam up to 5mm wide to be used, providing very good counting statistics in a short time.

6.2.3 Preliminary measurements taken on ENGIN

Preliminary measurements were first made on a test specimen of Cu+5%Zn. The purpose of these measurements was to determine the run times for the main experiments. With a tantalum target and water moderator in place, a run time of 300µAmps, with incoming slits of 10mm x 2mm, enabled single peak fits to be made (using the Rietveld software) to sufficient accuracy on at least ten diffraction peaks, probably many more.

The other major reason for carrying out the preliminary measurements was the worry that a significant degree of recrystallisation texture would cause problems by causing diffraction peaks to become severely attenuated. At the time, an X-ray texture measurement was unavailable so a crude measure of the degree of texture was obtained by rotating the specimen on ENGIN. For plastic anisotropy measurements, a texture as close as possible to random is required since this makes any subsequent modelling easier. Comparison of peak intensities from plane normals parallel and perpendicular to the swaging direction indicate only a weak recrystallisation texture (less than 2 x random).

6.2.4 Initial study of plastic anisotropy in brass

Despite the fact that there are instruments, such as HRPD, with much better TOF resolution than ENGIN, the fact that ENGIN was designed to rapidly make large numbers of reasonably accurate measurements to quickly map out parameter spaces made it the ideal instrument for an initial study of the effects of plastic anisotropy. The first experiment carried out was therefore to study as many different peaks from as many different alloys with as many different values of total plastic strain as possible. The interesting combinations of these variables were then studied on a number of different neutron instruments.

The following table (table 6.1) lists which plastic strains the different alloy compositions were tested after. The readings taken on each specimen are grouped in braces. The plastic deformation was carried out using a portable Hounsfield tensometer, with a clip gauge being used to measure the total (elastic+plastic) strain. The strains quoted were calculated from the permanent extension at zero load.

Specimen composition	Plastic deformation / %
Cu	{0,1,2,5,10,20},{0,5,10,20}
Cu-1%Zn	{0}
Cu-2%Zn	{0,5,10,20}
Cu-5%Zn	{0,1,2,5,10,20,20,20},{0,0}
Cu-10%Zn	{0}
Cu-15%Zn	{0,1,2,5,10,20}
Cu-20%Zn	{0,5,10}

Table 6.1: List of measurements taken during the initial study of plastic deformation on ENGIN.

Each measurement took approximately 2.5hrs (400 μ Ahr with a tantalum target and methane moderator). Because so many measurements were required, a specimen rack was made which could hold up to six specimens, stacked vertically above each other. The required specimen was then selected using the z drive of ENGIN. The specimen rack also allowed the specimens to be accurately repositioned after removal for plastic straining.

The gauge volume used (2mm x 2mm) was the largest that would safely fit completely within the specimen, even after 20% plastic elongation. A large gauge volume size was necessary for three reasons. Firstly it reduces the measurement time required to obtain good statistics. Secondly it increases the number of diffracting grains within the gauge volume. Since we are looking at individual peaks, it is important that there are a large number of grains diffracting into each and every peak, in order to obtain good statistics. Thirdly the difference in constraint means that the surface of a cylinder being deformed will cause it to work harden more quickly than the interior. This will result in type I residual stresses which vary across the diameter of the specimen. A large gauge volume averages out the variation of these long range stresses so that the only stresses present are the grain scale (type II) residual stresses that we hope to measure.

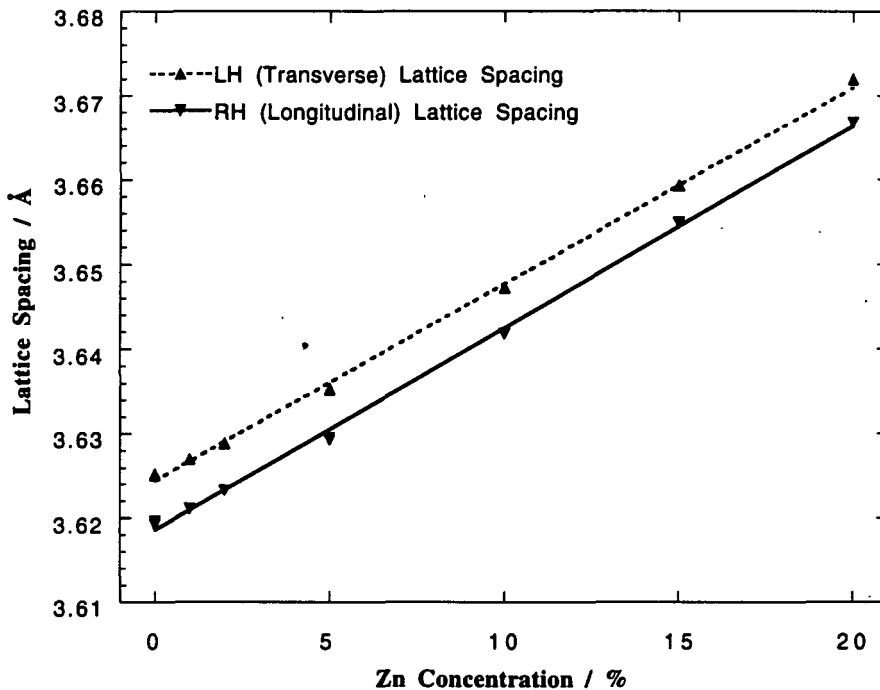


Fig 6.3: The lattice spacing of annealed Cu-Zn specimens, as a function of alloy composition. Error bars are smaller than the point markers.

6.2.5 Lattice spacing as a function of alloy composition

The lattice spacing of the annealed specimens, before deformation, is shown in fig 6.3 as a function of the alloy composition. It can be seen that the relationship is linear, as predicted by the Hume-Rothery rules. If we assume that the actual relationship is perfectly linear, then this graph enables us to determine the precise composition of each specimen, to a higher accuracy than EDX allows.

The difference between the two collimators can clearly be seen as an offset of approximately 0.0059\AA . This corresponds to a difference of $\sim 1600\mu\epsilon$, underlining the need to obtain separate lattice parameters for each detector. It is unclear how there can be such a difference between the results from the two detectors, since the focusing routine should eliminate it.

6.2.6 Residual stresses after plastic deformation

A selection of the data collected in this experiment is shown in fig 6.4. The graphs show the lattice spacings of specimens as a function of the plastic deformation which they have received. Two compositions are considered - pure Cu and Cu-15%Zn. These represent the two extremes of behaviour; copper deforms according to Taylor's model of plasticity whereas brass containing 15% Zn is described much better by the modified Sachs model. As seen from table 2, the Cu-5% Zn was also closely studied, since texture measurements in the literature have shown that it behaves in an intermediate fashion. Results from a full profile peak width are shown, together with those from a single peak fit on the {200} and {111} peaks. These were chosen as they represent the extremes of behaviour for elastic anisotropy. The full profile fit included all peaks from {111} ($N=3$) to {10 2 0} ($N=104$).

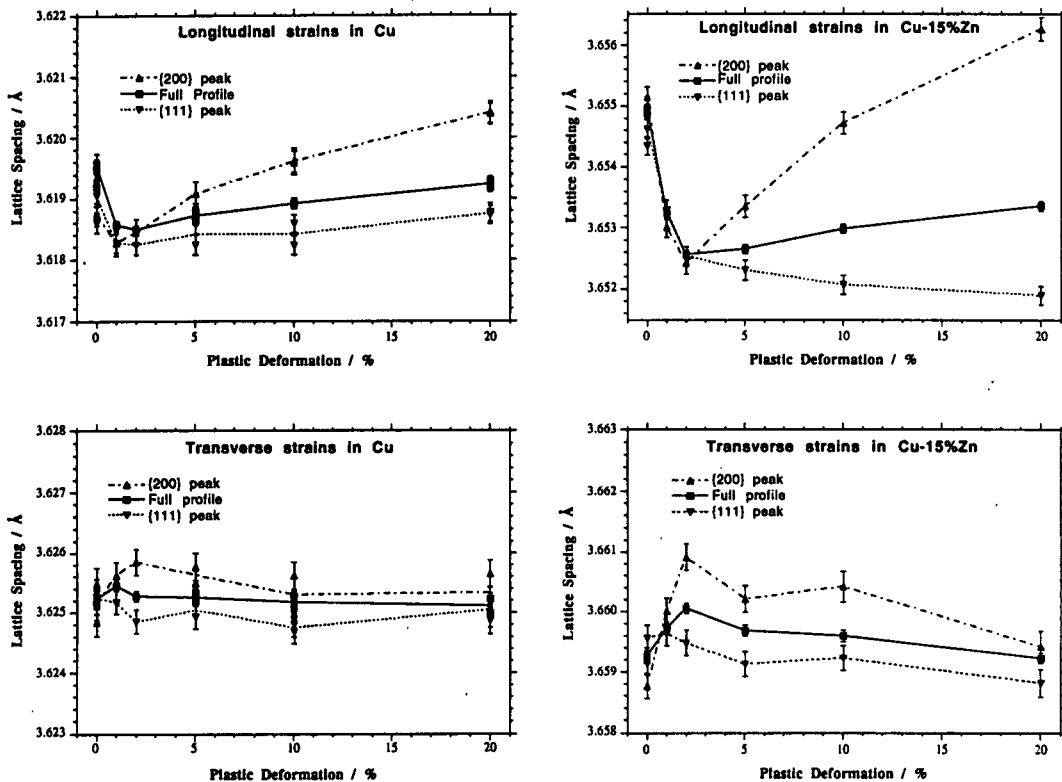


Fig 6.4: Lattice strains in two alloys in the Cu-Zn system as a function of the degree of uniaxial plastic extension after annealing. Results are shown for the {111} and {200} peaks, and for a full profile refinement of the whole profile.

The error bars of the full profile refinement can be seen to be much smaller than those from the individual peak fits, demonstrating the effectiveness of profile refinement over single peak analysis.

The first thing to notice about the curves is that the lattice spacings vary as a function of plastic strain. It was stated above that the profile refinement represents an average behaviour of the specimen. This is indeed seen to be true as, in most cases, the profile refinement lies between the {111} and {200} values. However, if the profile refinement really averaged out the effects of anisotropy induced residual stresses, we would expect the lattice spacing from the profile refinement to be flat, since there is no externally applied stress. It is possible that these effects are due to long range (type I) residual stresses being introduced by the deformation process. Because the specimens after annealing are known to have homogeneous grain size and composition, it is possible that the difference in constraint between the surface and the bulk is to blame. Experiments to test this hypothesis have been carried out at ILL, but the results have not yet been analysed.

Even more interesting is the fact that the graphs are not linear. Other workers researching plastic anisotropy by measurement of residual stresses have suggested that the relationships should be linear, if texture development is neglected. However all the results so far obtained from this data show that at around 2% plastic deformation, there is a sudden reversal of the residual stress development. This is unlikely to be caused by texture formation because it is happening at a very low total deformation. By contrast, the divergence of the {111} and {200} lines at high deformations is likely to be the result of texture development.

The most confusing, and worrying, feature of this data is the similarity between the behaviour of the different peaks at low deformations. We know that in a single phase material with no external loading, the integral of the residual stress from one free surface to another must be zero. However, these results show that after plastically straining annealed brass by 2%, *all* of the peaks show a residual compressive strain of $\sim 700\mu\epsilon$. Only two of the peaks are shown here but analysis of many others showed exactly the same trend. This effect cannot be due to plastic anisotropy. The most probable explanation is that the deformation was not homogeneous throughout the specimen. Inhomogeneous plastic deformation, such as that caused by the surfaces behaving differently to the bulk, or by inhomogeneous grain size, will cause long range (type I) residual stresses which could result in all of the peaks moving in the same direction. In order to test the theory of inhomogeneous plastic deformation, we can either perform a metallurgical analysis on the deformed specimens, or increase the size of the gauge volume to average over the whole specimen cross-section. The latter approach carries with it the risk of geometrical pseudostrains caused by small repositioning errors between measurements.

6.2.7 Peak widths after plastic deformation

There are a number of reasons why we would expect the width of the diffraction peaks to increase after plastic deformation. Firstly, plastic deformation increases the dislocation density in the specimen. The increase can often be several orders of magnitude, especially for materials with large work hardening rates, such as copper. Because there is a large strain gradient around each dislocation (due to the type III residual stresses), high dislocation densities will result in peak broadening.

Another cause of peak broadening is plastic anisotropy. The plastic strain in any particular grain (i.e. the mismatch between its current shape and its shape before deformation) will be

a function of its orientation and the stress history. The stress history, however, will depend upon the orientations of the neighbouring grains. There will therefore be a variation of the plastic strain, even for identically oriented grains. Diffraction, however, gives information about the elastic (not the plastic) strain in a population of identically oriented grains. The elastic strain will be a function of the difference in plastic strain between a grain and its neighbours (the so-called "plastic mismatch"). We therefore see that the elastic strain in an individual grain depends strongly on the orientation of its neighbours. This will result in a contribution to the peak broadening which will increase as a function of the plastic anisotropy exhibited by the material, and the total plastic deformation the specimen has been subjected to.

In the long term, it is hoped that it will be possible to separate the two contributions to peak broadening, and, in conjunction with the peak shifts, give information on the deformation history of the specimen.

Fig 6.5 is similar to fig 6.4, but shows peak widths, rather than lattice spacings. The measure of peak width used was the refined value of SIGM2. This represents the Gaussian component of the diffraction peak. The lines drawn are best fit straight lines through the data. The uncertainties of the PKCN1 values are larger than those for the lattice spacings but there are still clear trends visible in the data.

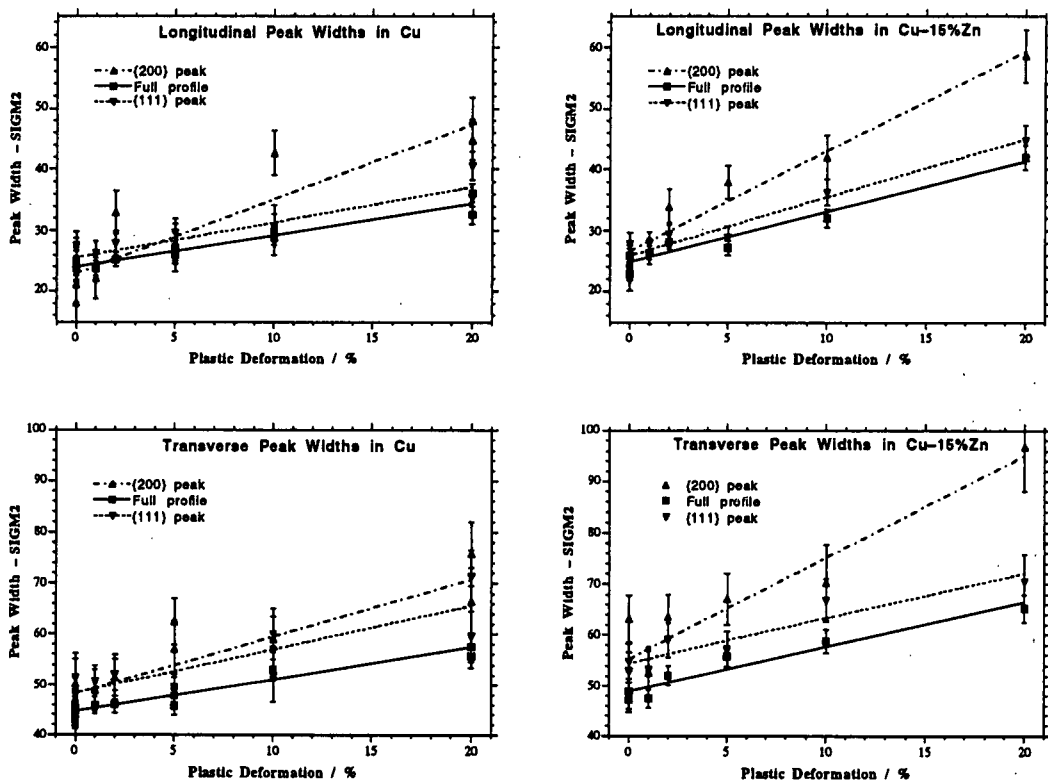


Fig 6.5: Peak widths for two alloys in the Cu-Zn system as a function of the degree of uniaxial plastic extension after annealing. Results are shown for the {111} and {200} peaks, and for a full profile refinement of the whole profile. SIGM2 – the Gaussian component of the peak was used for the comparison.

The peak widths of the longitudinal data (collected in the RH detector) are generally significantly sharper than those of the transverse data. It is believed that, as in figure 6.3, this is attributable to differences in the performance of the collimators and detectors, rather than to any materials effects. However studies of this sort would greatly benefit from having the same quality of data from both detectors.

Whilst the peak widths of the {111} and the {200} peaks are virtually the same in the annealed specimen, the {200} peak width increases much more quickly with plastic deformation. One possible explanation for this is as follows. The primary slip system operating in FCC materials is the {111}<110> type. As with electron diffraction in a TEM, a dislocation will be "invisible" to neutron diffraction if $g \cdot b = 0$. The Burgers vector of a dislocation on the primary slip system will be of the <110> type. Therefore, for some of the diffracting {111} planes, some of the dislocations will be invisible. For example dislocations with $b = [110]$ will not affect peaks diffracted by the {111} planes ($g = 1\bar{1}1$). The result of many of the dislocations being "invisible" to the {111} peak is that there will be less peak broadening of this peak. The same will be true for the {200} peak (e.g. dislocations with $b = [110]$ will not affect the {002} planes). However, when all the different combinations of slip system b and diffracting plane normal g are considered in turn, we find that half of the dislocations will be invisible to the {111} peak, whereas only one third are invisible to the {200} peak. The {200} peak would therefore be expected to be broader than the {111}. Whilst this is a possible explanation for the observed differences in broadening, more peaks must be studied to be confident that it is the correct one.

The width given by the profile refinement is, in all cases, the lowest of the three values plotted. The reason for this is unclear as we would expect the average "percentage invisibility" for all peaks to be very low. When higher order peaks are considered, it is very rare for the $g \cdot b = 0$ condition to be fulfilled. For example all dislocations will be visible to, and contribute to the broadening of, the {7 1 2} planes. It is possible that a poor quality instrument parameter file is partially to blame (see previous section), but this would not explain why the gradient is so low. Much more analysis on peak width, and shape, will soon be carried out on higher resolution data from HRPD.

6.3 References

Kroner, E.J. (1967), *J. Mech. Phys. Solids* 15 pp 319-329

Sayers, C.M. (1983), "The strain distribution in anisotropic polycrystalline aggregates subjected to an external stress field", *Phil. Mag. A* 49 pp 243-262

Leffers, T. & Lorentzen, T. (1992) "The Plastic Regime, Including Anisotropy Effects", in "Measurement of Residual and Applied Stress Using Neutron Diffraction", ed Hutchings, publ. Kluwer Academic Publishers, pp 171-187

Pedersen, O. & Leffers, T. (1987), "Modelling of Plastic Heterogeneity in Deformation of Single Phase Materials", in "Constitutive Relations and Their Physical Basis", ed Andersen S.I., pp 147-172

7 Neutron Diffraction Determination of the Complete 3D Residual Stress Distribution Surrounding a Cold Expanded Hole

7.1 Abstract

Cold expansion of holes in aircraft structures to combat fatigue is now common practice. Expansion is achieved using commercially available equipment which includes a lubricated sleeve and prescribed levels of mandrel interference. The optimum degree of mandrel interference for a particular application will however depend on the local geometry of the component and fatigue life predictions of structures containing such expanded holes rely critically on estimates of the residual stress distribution surrounding the hole. The 3D residual stress distribution around 9.52mm, (3/8"), holes in a high strength aluminium alloy that have been expanded using a commercial split sleeve method have been measured non-destructively using neutron diffraction and compared to previous measurements using a destructive modified Sachs method. Differences in residual compressive hoop stress distribution were detected through the thickness of the specimen with hoop stresses being smaller at the 'inlet' side of the hole, (where the mandrel first engages), when compared to the 'outlet' side. Good agreement between the neutron diffraction measurements and those from the modified Sachs method is obtained if the effect of gauge volume averaging is taken into account. It is also shown that diffraction peak width varies with macrostrain gradient suggesting that peak width can be used as an indicator of the level of macrostrain gradient in a material.

7.2 Introduction

Rising demand for longer lives in both civil and military aerospace is likely to ensure that the economical lives of some aircraft structures will be dictated by their long-term fatigue performances. Generally, the primary source of fatigue damage (cracking), is at mechanical joints and the problem becomes more vital as the demand for minimum structural weight to improved aircraft performance increases. Mechanical joining methods are commonly used in aircraft structures. The transfer of loads from one structural assemble to another is accomplished either through the bolts in shear or by friction at the contacting surfaces by means of fastener clamping. So particularly at high shear load transfer joints, where thin or thick assembles are jointed, fastener holes can become the major source of fatigue cracking [1,2].

Cold expansion techniques have been used for over thirty years to produce fatigue life enhancement and have been reviewed by Champoux [3]. Superposition of the residual stresses near the hole with service loads leads to improvements in fatigue life either by delaying or suppressing crack initiation or more often by reducing fatigue crack growth rates. Expansion is achieved using prescribed levels of mandrel interference. The optimum degree of mandrel interference for a particular application will however depend on the local geometry of the component and fatigue life predictions of structures containing such expanded holes rely critically on estimates of the residual stress distribution surrounding the hole. Increasing importance is being given to the three dimensionality of the residual stress distribution produced by split sleeve expansion. It has been suggested from fractographic evidence that the residual stress distribution

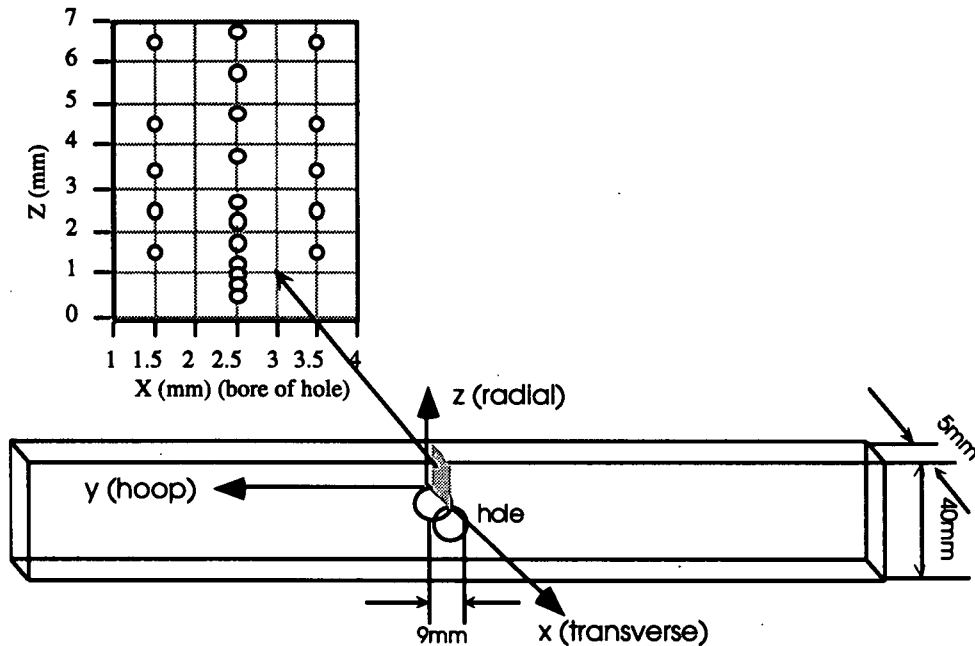


Figure 7.1 Dimensions of the cold expanded hole specimen

varies across the thickness of the plate [4,5]. In particular it has been suggested that a larger residual compressive hoop stress is generated at the mandrel outlet face of the plate than at the mandrel inlet face. Although measurements of the 3D residual stress distribution near the hole had been made by a destructive method - a modified Sachs method [6], this paper reports non destructive neutron diffraction measurements used to validate the destructive modified Sachs method.

7.3 EXPERIMENTAL DETAILS

7.3.1 Precise determination of measurement position

The measurements were carried out on the ENGIN diffractometer which. In order to obtain the high spatial measurement precision required for accurate 3D work on a relatively fine scale, a number of careful experiments were carried out to precisely determine the position of the gauge volume with respect to the specimen surfaces. The full stress tensor approach used here also required measurements to be made accurately along the three principal axes which were known due to the symmetry of the hole expansion process. To achieve the former condition the position of the gauge volume with respect to the component was obtained to an accuracy of better than 0.1mm by fast surface scanning and fitting the obtained integrated intensity data to a model describing the intensity variation as the gauge volume enters the material [7]. The latter condition was achieved by placing the specimen at the centre of a square prismatic orthogonal frame which was constructed so that the point equidistant from the two most orthogonal faces was known. Using a high accuracy metrology table a known point on the specimen was located at this point before the frame was transported to the neutron source. As ENGIN possesses two 90° collimated detectors, this enables measurements to be made along the three principal directions to within 1° using only a single quick specimen re-alignment.

7.3.2 Stress distribution around the cold expanded hole

The dimensions of the specimen are shown in figure 7.1. A series of measurements of the hoop and transverse strains were made along the zx plane at the positions also shown in figure 7.1. The frame and hence the specimen was then rotated by 90° and measurement of the radial and transverse strains were made at the same positions in the zx plane of the component. Analysis of the obtained spectra was carried out using a Pawley refinement method to calculate the lattice parameter, a. The least-squares average (LSA) strain, may then be calculated thus:

$$\epsilon = \Delta a/a_0 \tag{1}$$

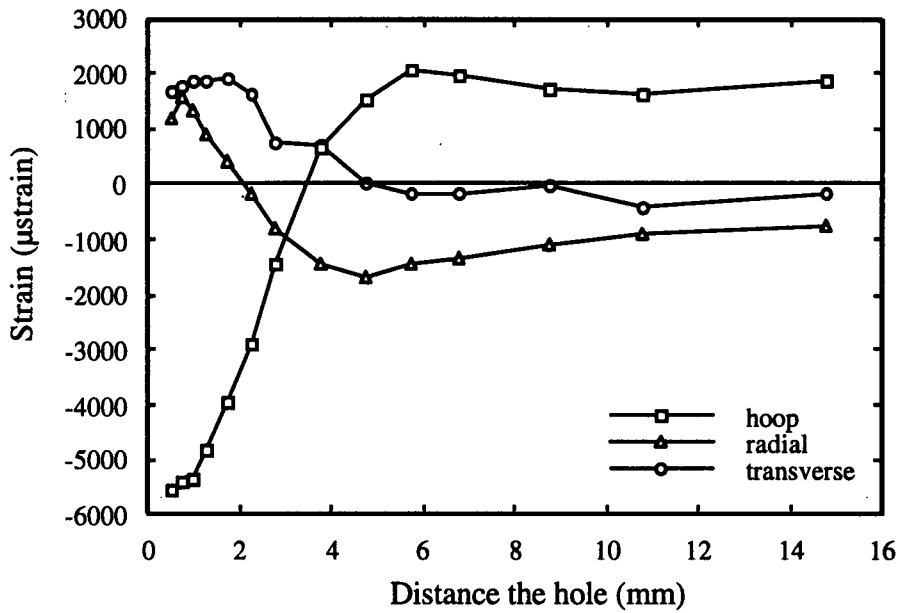


Figure 7.2 Residual strain distribution in the mid-plane of the plate.

where Δa is the lattice parameter shift, and a_0 is the strain-free lattice parameter. The strain-free value, a_0 , was obtained by measuring a point 100mm away from the hole. Figure 7.2 shows the residual strain distribution along the mid-thickness of the plate ($x=2.5\text{mm}$). The stress distribution in isotropic polycrystalline materials is calculated from the measured strain distribution by

$$\sigma_{ij} = \frac{E}{1 + \nu} \epsilon_{ij} + \frac{\nu E}{(1 + \nu)(1 - 2\nu)} \delta_{ij} \epsilon_{kk} \tag{2}$$

where k is a dummy suffix summing over all k (i.e. $\sigma_{kk} = \sigma_{11} + \sigma_{22} + \sigma_{33}$); E , the Young's modulus; ν , the Poissons ratio; and δ , the Kronecker's delta function. The residual stress distribution was calculated from the strain distribution measured by neutron diffraction, using equation (2). The resulting residual stress distribution at the centre of the plate is given in Figure 7.3.

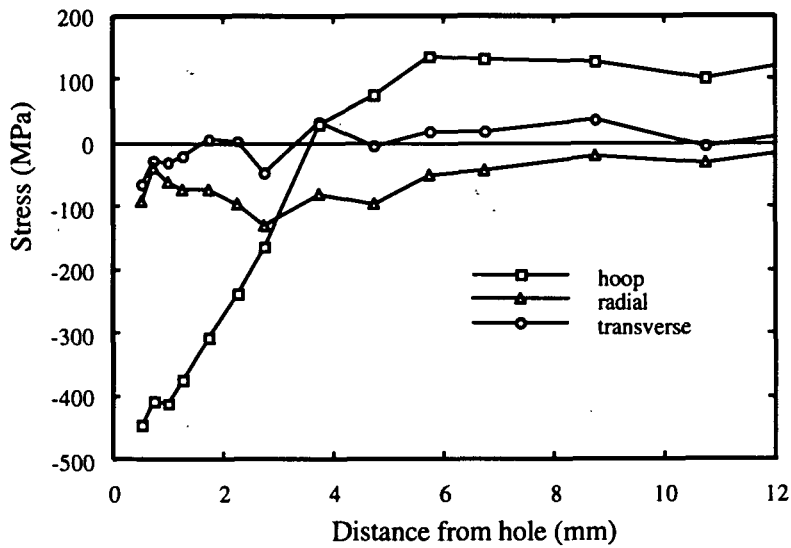


Figure 7.3 Residual stress distribution in the mid-plane of the plate.

It can be seen from figure 7.3 that the general shape of the residual stress distribution is as expected and shows reasonable correlation with previously published estimates of the distribution obtained from destructive mechanical tests [6] except that there was no evidence of stress relaxation near the hole. The accuracy of these measurements is dependent on how well we can control or compensate for systematic errors. These are the errors which will make the experimental results different from the “true” values. The peak positions and hence the lattice parameters may be affected by a greater or lesser degree by type I, II and III residual stresses, prior plastic deformation and near surface [8]. In this analysis we focus on the effects of near surface measurement and the use of a gauge volume which is large compared to the scale of the residual stress gradient.

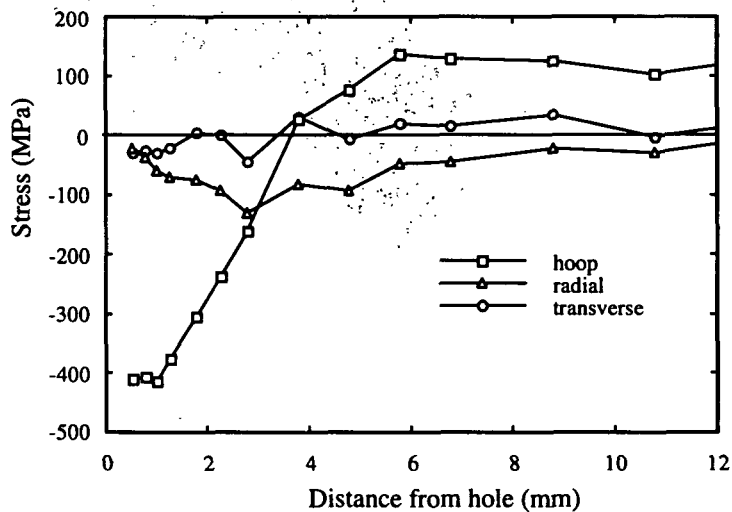


Figure 7.4 Residual stress distribution after correction for near surface effects.

7.4 DISCUSSION

7.4.1 Correction for near surface effects

A pseudo-strain is produced in most neutron diffraction measurements of residual stress when the gauge volume straddles the sample surface so that only part of the collimated detector sees all of the gauge volume [9]. For the case of the cold expanded hole in the aluminium plate, only the radial strain measurement was affected as the other strains were measured by scanning the gauge volume vertically through the component surface (ie using a 'Z-scan'). An empirical instrumental correction was achieved based on the knowledge that the radial stress should become zero as the surface is approached. Inspection of the radial stress as it approaches the surface of the hole in figure 7.3 shows that there is clearly something wrong as it deviates sharply from zero just where we expect the surface effect to become significant. Thus the radial strains in this area were linearly extrapolated so as to produce a zero radial stress in this area.

The subsequent corrected results of the residual stress distribution along mid-thickness line is shown in figure 7.4. Although the residual stress distribution is substantially unchanged there is now some evidence of stress relaxation near the hole. Based on these corrected results (only one point corrected) and in combination with surface residual stress measurements made by X-ray a 3D hoop residual stress map can be constructed using the principal of minimum curvature and is plotted in figure 7.5. It also can be seen from figure 7.5 that there is a larger residual compressive hoop stress at the mandrel outlet face of the plate than at the mandrel inlet face. Since these measurements, the near surface effect on ENGIN has been further studied and both numerical modelling and experiments on stress free powders have shown that the correction utilised here is accurate [9].

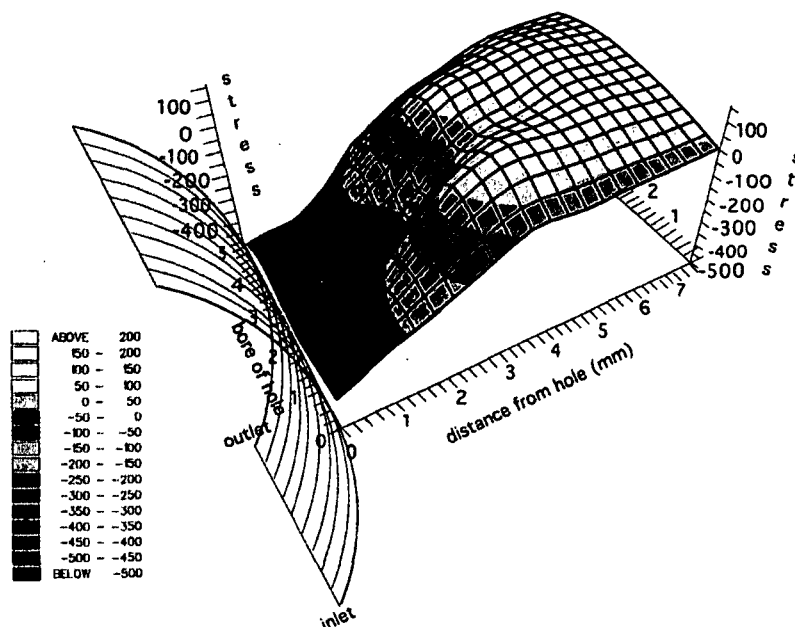


Figure 7.5 Full 3D residual stress distribution as measured by neutron diffraction.

7.4.2. Effect of gauge volume averaging

The measured strain distribution from neutron diffraction is likely to be different from the real strain distribution in areas of rapidly changing strain gradients due to the finite size of the gauge volume [9]. This is why the evidence of hole relaxation seen in the neutron measurements (figure 7.5) is not as pronounced as in the mechanical measurements made using the modified Sachs technique (figure 7.6).

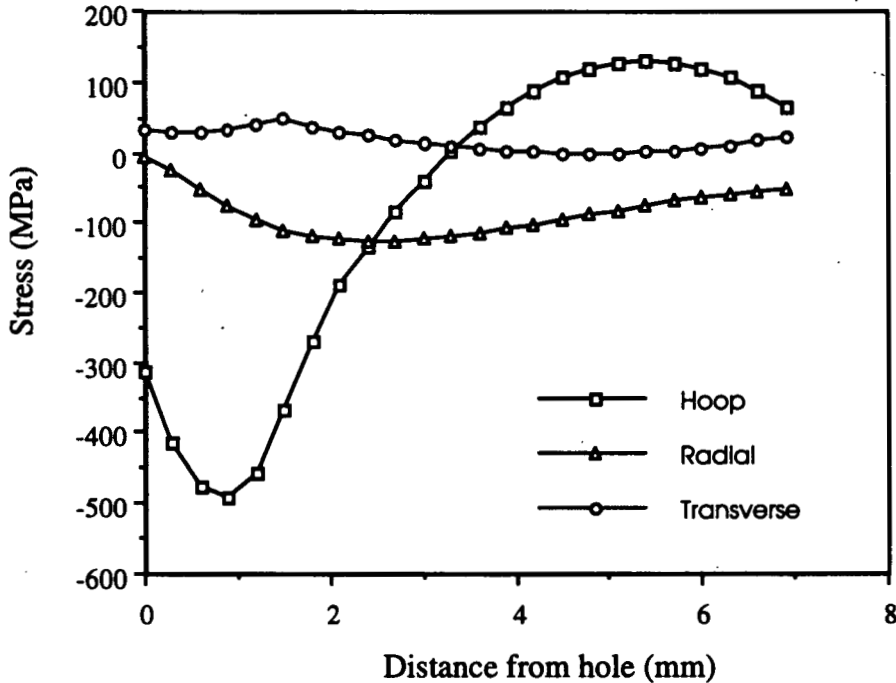


Figure 7.6. Residual stress distribution as measured by the modified Sachs technique [6].

Unfortunately, deconvolution of the 'averaged' neutron strain measurements to the 'real' distribution is difficult, but an interesting comparison is to compare the neutron distribution to the distribution produced by averaging the strain distribution measured by Sachs measurement over a similar gauge volume dimension i.e. 2.5 mm. Such a Sachs "average" and the neutron strain data for the middle plane position ($x=2.5$) are plotted in figure 7.7. A similar effect is found with plots of the 3D residual stress distribution around the hole with a Sachs "average" plot appearing virtually identical to figure 7.5. So the residual stress distribution that we measure around a 4% FTI expanded hole is ostensibly identical when measured by both neutron diffraction and a destructive modified Sachs technique. As the two methods use entirely different physical principles it is clear that the residual stress field can be said to be characterised with a high degree of confidence and is capable of being used for damage tolerance life prediction purposes.

7.4.3 Peak broadening as an indicator of strain gradient

It is well known that microstrain can affect peak width. More interestingly it is possible that macrostrain gradient also may cause peak broadening. To consider this, peak broadening has been estimated using the peak-shape functions of GENIE, the analysis software used at ISIS. The peak shape depends on several physical factors, notably the pulse shape,

moderator physics, instrumental resolution and sample effects. A reasonable approximation to the powder diffraction peak shape has been found to be [11]

$$P(t) = \frac{t^2}{2\tau_f^3} \exp\left(-\frac{t}{\tau_f}\right) * \{(1-R)d(t) + R\left(\frac{1}{\tau_s}\right) \exp\left(-\frac{t}{\tau_s}\right)\} * \frac{1}{\sigma\sqrt{2\pi}} \exp\left(-\frac{x^2}{2\sigma^2}\right) \quad (4)$$

where t is time of flight, τ_f is the fast decay constant, τ_s the slow decay constant, R the switch function, related to a Boltzmann function, $\exp(-E/E_0)$, σ is the Gaussian width parameter, and $*$ represents convolution.

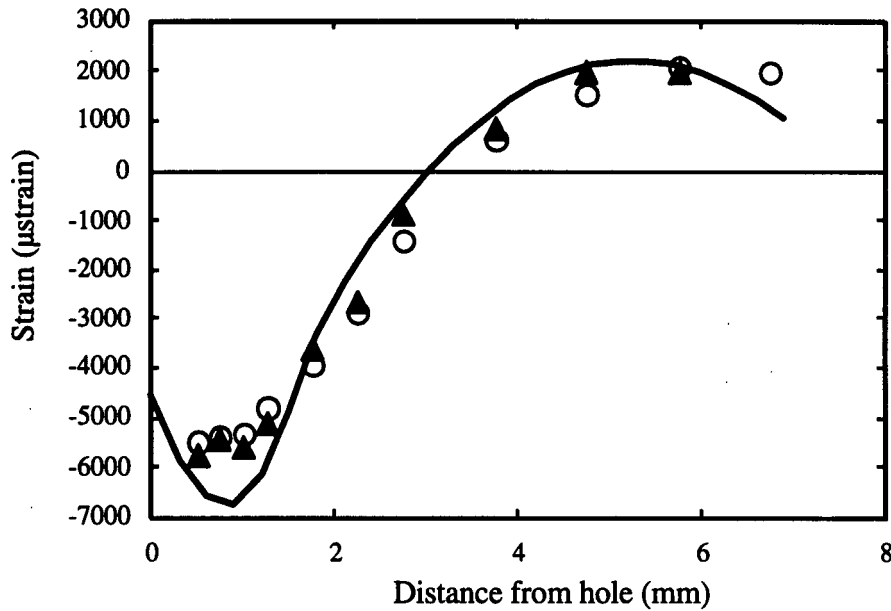


Figure 7.7 Comparison of 'averaged' Sachs and neutron strain measurements.

The first two terms in this expression, representing the moderator physics were described by Ikeda and Carpenter (1985) [12]. Both the Gaussian and Lorentzian terms (last two terms) are associated with instrumental and sample effects. In Pawley refinement, there are three parameters to describe peak broadening. The Gaussian parameters [11]

$$\sigma = (\sigma_1 + \sigma_2 \lambda^2 + \sigma_3 \lambda^4)^{1/2} \quad (5)$$

where σ_1 is due to the finite width of the neutron pulse and paracrystallinity in the sample and is normally negligible, σ_2 is the most significant term in the expression and includes the effect of strain in the sample and a small contribution from the $\Delta\theta\cot\theta$ term in the instrumental resolution, and σ_3 is a very small contribution due to particle size effects and stacking faults.

For strain measurement, the contribution from the term, $\Delta\theta\cot\theta$, can be ignored as the diffraction conditions are constant. σ_2 is governed by strain effects, such as microstrain as well as macrostrain gradient. Since there is only 4% plastic deformation at the cold expanded hole the effect of the varying microstrain on σ_2 is also negligible. Therefore, σ_2 should characterise the variation of the macrostrain gradient near the hole.

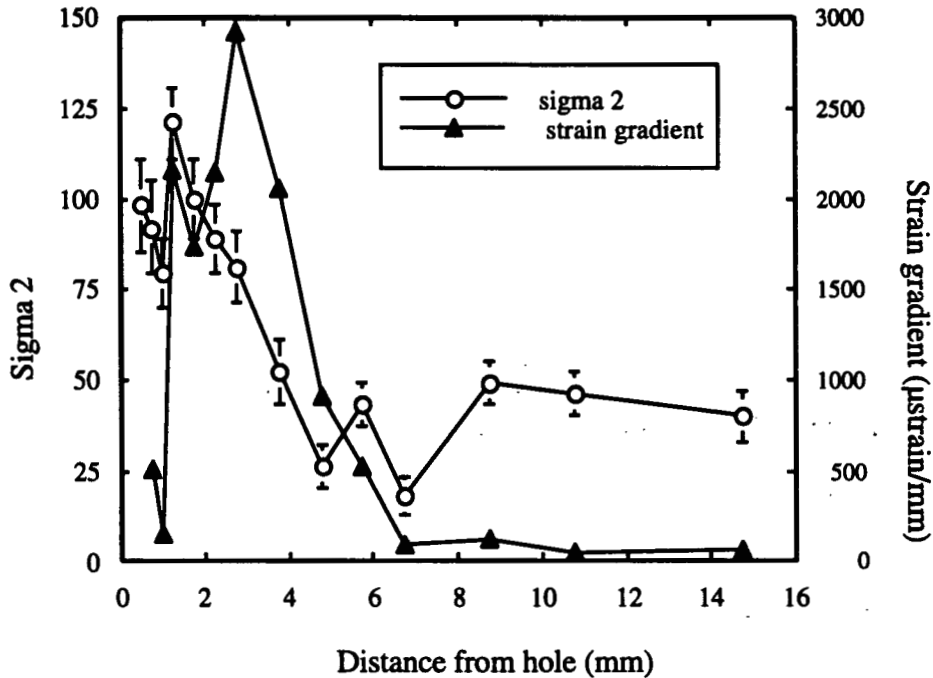


Figure 7.8 Correspondence between sigma 2 and hoop strain gradient

To test this hypothesis the hoop macrostrain gradient, directly derived from the neutron diffraction measurement, is plotted against the LSA (least-square average) sigma 2 in figure 7.8. The LSA sigma 2 reflects the trend in the macrostrain gradient well.

7.5 CONCLUSIONS

1. A 3-D stress measurement has been made at a 4% FTI expanded hole in high strength aluminium alloy using neutron diffraction.
2. Differences in residual compressive hoop stress distribution were detected through the thickness of the specimen with hoop stresses being smaller at the 'inlet' side of the hole, (where the mandrel first engages), when compared to the 'outlet' side, similar to the result from mechanical measurement.
3. The comparison between the measurements from neutron diffraction and modified Sachs method is feasible providing the gauge volume average effect in neutron diffraction is taken into account.
4. The variation of peak width can be used as an indicator of variation of type I strain gradients in the materials.

References

- [1]. Mann, J.Y. and Jost, G.S., Metals Forum, 6(1983)43-53.
- [2]. Schwarmann, L., International Journal Of Fatigue, 2(1982)105-111.

- [3]. Champoux, R.L., "An overview of cold expansion methods", in *Fatigue Prevention and Design*, ed. J.T. Barnby, Chamelon Press, London, 1986, pp.35-45.
- [4]. Ozelton, M.W. and Coyle, T.G., "Fatigue life improvement by cold working fastener holes in 7050 aluminium" in *Fatigue In Mechanically Fastened Composite And Metallic Joints*, ed. Potter, J.M., ASTM STP 927, 1986, pp.53-71.
- [5]. Pell, R.A., Beaver, P.W., Mann, J.Y. and Sparrow, J.G., *Fat. Fract. Eng. Mat. and Struct.*, 12(1989)553-567.
- [6]. Ozdemir, A.T, Wang, D.Q. and Edwards, L. "Measurement of the 3D residual stress distribution at split sleeve cold expanded holes, in *Proceedings of the Fourth International Conference on Residual Stresses* Baltimore, USA, ed. James, M.R., publ. Society for Experimental Mechanics, USA.1994 pp. 1144-1153
- [7]. Wang, D.Q. and Edwards, L., "Precise determination of specimen surface position during sub-surface strain scanning by neutron diffraction", elsewhere in this publication.
- [8]. Wang, D.Q. and Edwards, L., "Systematic error analysis associated with residual strain measurement by neutron diffraction", to be published.
- [9]. Wang, D.Q., Harris, I.B., Withers, P.J. and Edwards, L., "Near-surface strain measurement using neutron diffraction", elsewhere in this publication.
- [10] W.I.F.David, D.E.Akporiaye, R.M.Ibberson and C.C.Wilson, *The high resolution powder diffractometer at ISIS - an introductory users guide*, Rutherford Appleton Laboratory Report, RAL-88-103, 1988
- [11] S.Ikeda and J.M.Carpenter, *Nucl.Inst.Meth.* A235(1985)553

8 Investigation of Vibrational Stress Relief

8.1 Objectives

The characterisation of stress relief procedures requires systematic investigation of the three-dimensional stress state before and after treatment. It was the objective of the Institute of Pure and Applied Nuclear Physics group, University of Kiel, within the current Brite/EuRam project, to evaluate the efficiency of different stress relief procedures, as applied to actual engineering components.

Vibratory stress relief is said to be a method which avoids thermal treatment and the subsequent danger of microstructural changes that may be caused, but it is still an open question how, and to what extent, the relief takes place and whether the method induces any damage.

It is assumed that stress relaxation takes place by microplastic deformation, in which the movement of dislocations redistributes the residual elastic stresses and microstresses [cf. M.R.James, *Relaxation of Residual Stress - An Overview*; Internat. Guidebook on Residual Stress, A.Niku-Lari edit., Pergamon Press 1987].

8.2 Samples

The steel samples (St52) to be investigated were produced according to the requirements of the German company VSR Industrietechnik GmbH., Mühlheim/Ruhr, who also carried out the vibrational treatment. This was done using their commercial equipment and technical know-how in the field of vibrational stress relief. For a successful stress relief process using a commercial instrument (in our case a "FOURIERMATIC V.2.01" from VSR) a minimum specimen weight of 50 kg is necessary, which leads to the outlines of the sample given in Figure 8.1. For a material, a conventional construction steel (German specification: St 52-3) with a minimum yield strength of 520 MPa was chosen.

Since measuring all samples twice (both before and after stress relief treatment) could not be achieved in one beam time period, three separate samples were produced. In order to achieve an identical initial "as received" stress state for these samples, the production of the rings started from a large 1570 x 1600mm steel plate which was first bent to an "open" pipe with a gap of 33mm. The ends of the pipe were elastically bent together and then the stress state was fixed by welding. Then this pipe was cut into 6 rings with heights of 250 mm. Having a weight of about 60 kg each, the rings were also good examples to demonstrate the capability of ENGIN to investigate real engineering structures.

For the neutron diffraction investigations three of these rings were used. One had no further treatment (AS RECEIVED sample) in order to determine the starting stress state, one got a stress relief heat treatment at 550°C for 5h (HEAT TREATED). The third one was vibrated by VSR. The vibration was done by mounting the vibration motor at two different positions and vibrating 3-4 times for five minutes at predetermined Eigen-frequencies of the sample.

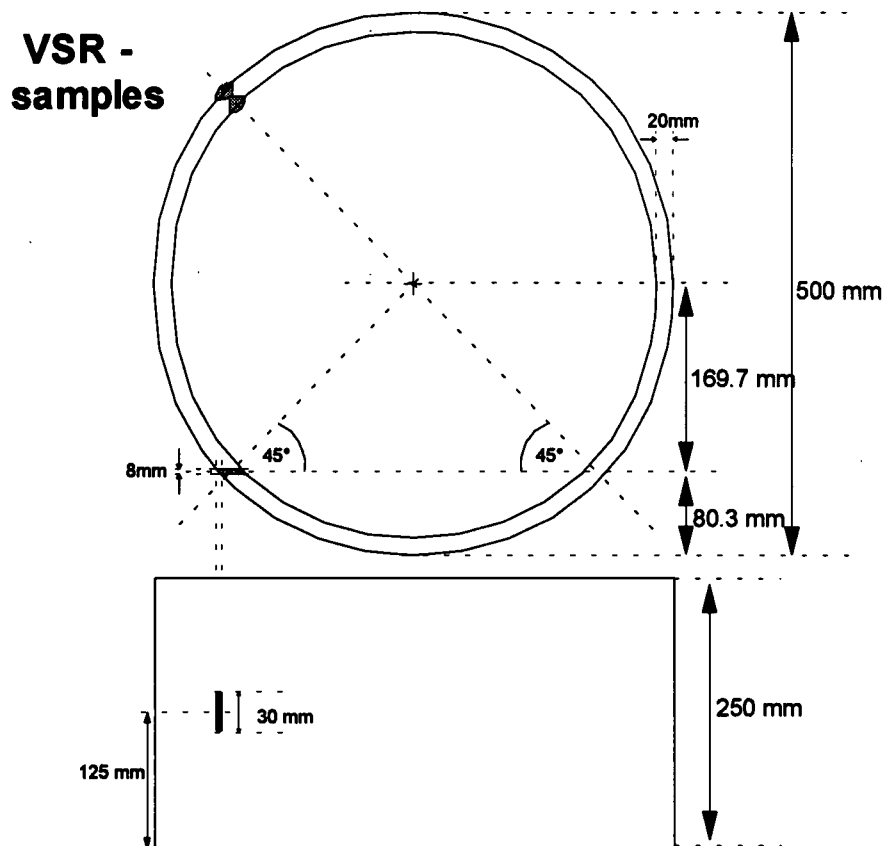


Fig 8.1.: Outlines of the VSR-samples with the size and positions of the machined hole

8.3 Preparation of the samples

In order to measure the strain in the hoop direction the samples had to be oriented so that the neutron beam would have to penetrate the samples twice (Fig. 8.2). The neutron flight path within the sample in this case would have reduced the intensity to 0.3% of the incoming intensity. Therefore slits of 8x30 mm were machined at the point of the first penetration of the neutron beam.

To make sure that the stress state at the measuring position was not influenced by the removing of material, strain gauges were applied at the measuring point and were monitored during the machining process. For all three samples the strains at the measuring points caused by the machining were smaller than $50\mu\epsilon$ and for that reason the stress state can be assumed not to be affected by the machining. Machining the slits resulted in a reduction of the neutron flight path within the steel by 50% and the useful neutron intensity was at an acceptable value of approx. 6% of the primary beam intensity.

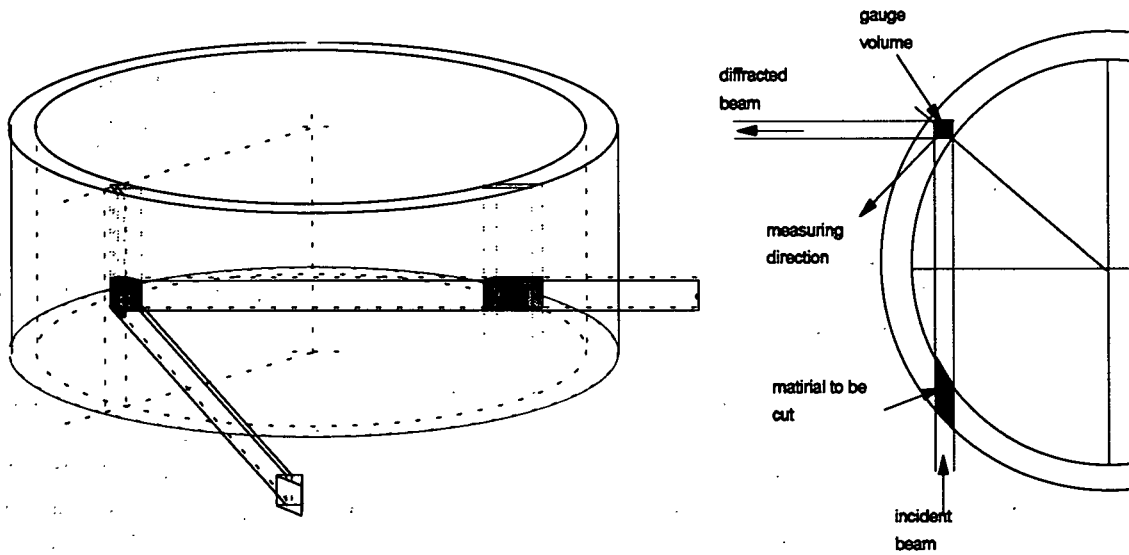


Fig. 8.2 Positioning of the VSR rings in the neutron beam for measuring the hoop direction

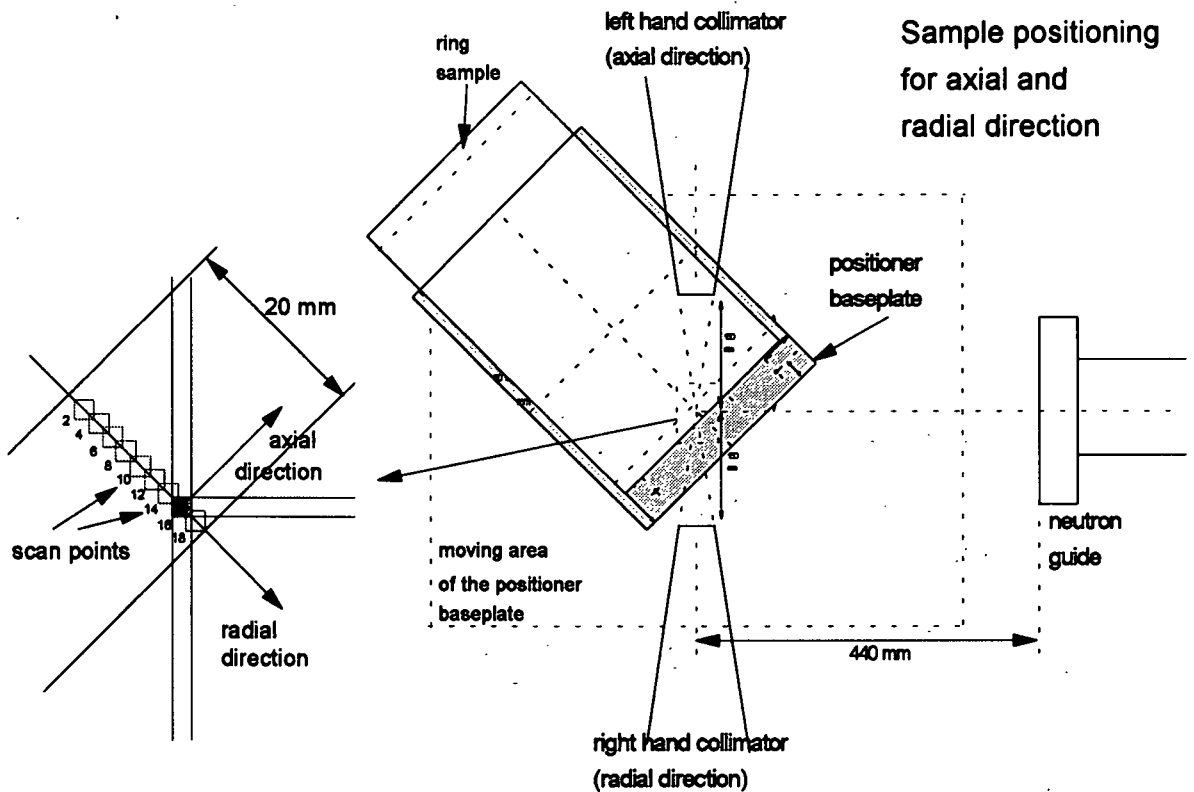


Figure 8.3 Schematic top view of the positioning of the rings for simultaneous strain measurement in axial and radial direction

8.4 Neutron diffraction measurements

The aim of the neutron diffraction measurements was to determine the stress tensor for all three samples at different distances from the inner radius. It is sufficient to measure the lattice strains in the three principal directions (hoop, axial and radial direction) of the sample, since the principle stress directions can be assumed to be known from the geometrical symmetry of the sample and its production process. In order to avoid any influence of the welding, the strains were measured at the opposite sides to the weld.

8.4.1 Axial- and radial direction

The new detector set-up with two collimators allowed to measure the axial and radial directions simultaneously. Therefore the samples were mounted vertically at 45° relative to the incident beam line as shown in Figure 8.3 (right).

The scans of the axial/radial direction were separated into two parts, in order to avoid a critical decrease of the scattering intensity of the right hand detector due to absorption when the inner points were reached (Fig. 8.3 - left). This was achieved by rotating the sample by 180° after the central point had been measured. The left hand detector gives approximately the same count rates for all points of the scan, since the neutron flight path through the material is always the same.

With the sample in vertical position the height of the gauge volume causes a shift in the radial measuring position and a change in scattering angle as shown in Figure 8.4.

In order to check whether these errors have to be taken into account for a precise stress measurement, the values depending on the height H of the gauge volume and the sample radius at the measuring position must be calculated:

$$\text{From the figure follows: } \sin \alpha = \frac{h}{R} \cong \frac{\Delta r}{h} \Rightarrow \Delta r \cong \frac{h^2}{R}$$

With the height H of the gauge volume the shift Δd in radial position is

$$\Delta d = \frac{1}{(H/2)} \int_0^{(H/2)} \Delta r dh = \frac{H^2}{12R}$$

$$\text{From the upper equation: } \alpha = \arcsin \frac{h}{R}$$

The average change in diffraction angle $\Delta \bar{\alpha}$ can be derived as:

$$\begin{aligned} \Delta \bar{\alpha} &= \frac{1}{(H/2)} \int_0^{H/2} \alpha(h) dh = \frac{1}{(H/2)} \int_0^{H/2} \arcsin \frac{h}{R} dh \\ &= \frac{1}{(H/2)} \left[\frac{H}{2} \arcsin \frac{H}{2R} + \sqrt{R^2 - \frac{H^2}{4}} - R \right] \end{aligned}$$

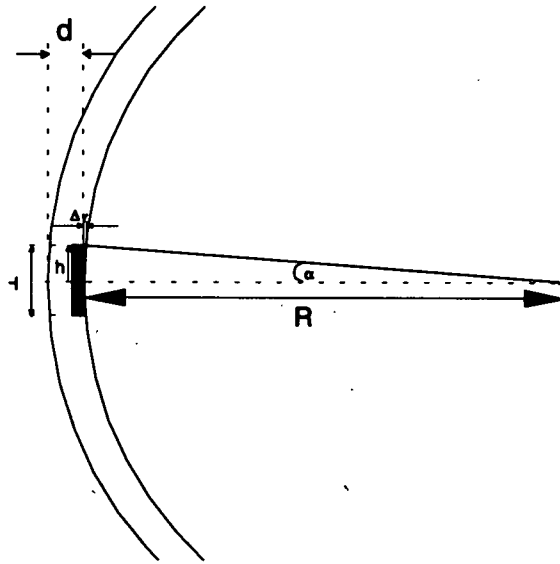


Figure 8.4 The beam/slit height causes a shift in the radial measuring position Δr and a change in the angle between the sample normal and the scattering direction

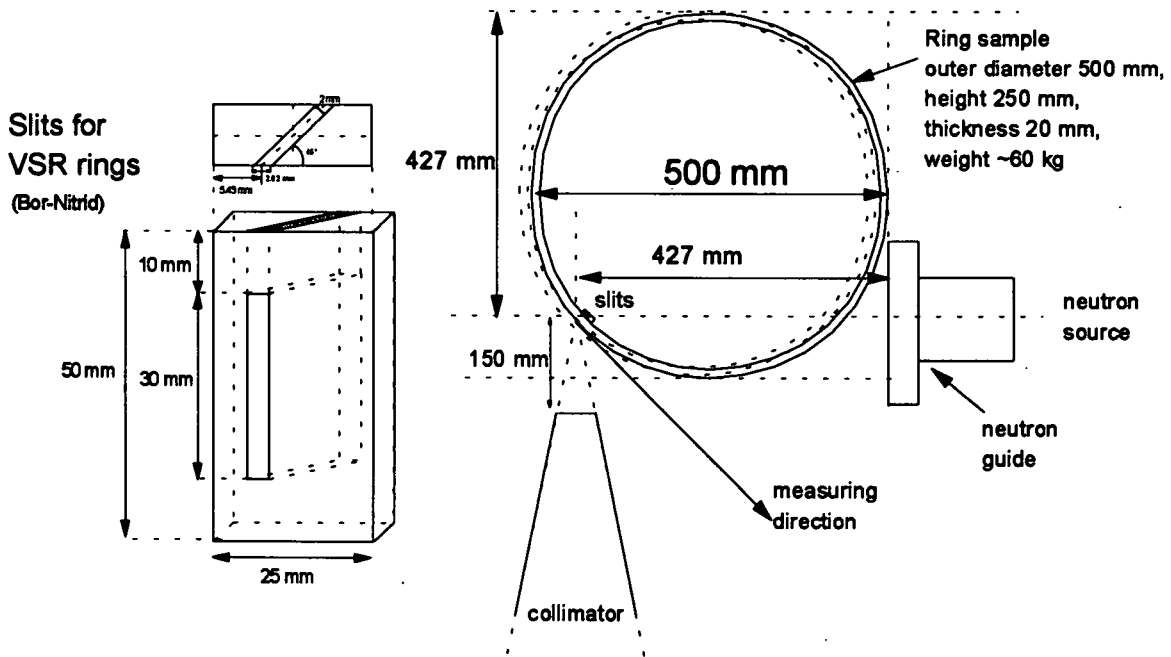


Figure 8.5 Positioning of the rings for hoop direction measurements (right) and Boron-Nitride slits

8.4.2 Hoop direction

The position of the samples for hoop direction measurements is shown in Figure 8.5. The 500 mm diameter of the ring has been found to be the upper limit of the outlines for ring samples, since the ring is nearly touching the neutron guide tank. For larger samples the tank would have to be removed. For hoop direction measurements, special slits with 45°

degree geometry were machined from boron nitride blocks of 10 mm thickness and glued directly onto the samples, which gave an optimal defined gauge volume of 2x2x30mm.

8.4.3 Sample Positioning using the Neutron Beam

Due to the large sample dimensions, positioning the sample exactly by using only the telescopes was impossible (see Fig.8.3 and 8.5). Therefore intensity scans in a direction perpendicular to the sample surfaces were executed to determine the sample position relative to the neutron beam

A calculation of the relationship between the scattered intensity, $J(A)$, and the depth of penetration, d , of the gauge volume into the sample's surface follows. For calculating this relation, a gauge volume of 2x2x30 mm³ was considered. The scattered intensity was calculated with regard to the area (grey), which has already penetrated the surface and to the absorption coefficient μ . Due to the gauge volume geometry one gets three analytic terms related to the penetration depth, d , for the scattered intensity at the right hand collimator .

Intensity decrease due to absorption: $I(x, y) = I_0 e^{-2\sqrt{2}\mu_0 y}$.

Substituting $I_0 = 1$ and $\mu = 2\sqrt{2}\mu_0 \Rightarrow I(x, y) = e^{-\mu y}$

Region I: $0 < d < \sqrt{2}$:

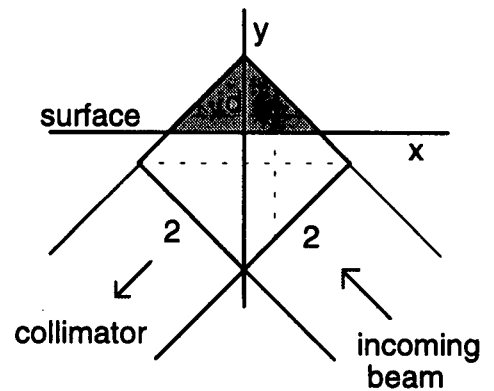
$$J(A) = 2 \int_0^d \int_0^x I(x, y) dy dx = 2 \int_0^d \int_0^x e^{-\mu y} dy dx = -\frac{2}{\mu^2} (1 - \mu d - e^{-\mu d})$$

Region II: $\sqrt{2} < d < 2\sqrt{2}$:

$$J(A) = \frac{2}{\mu^2} (1 - \mu(d - 2\sqrt{2}) + e^{-\mu d} (1 - 2e^{\sqrt{2}\mu}))$$

Region III: $2\sqrt{2} < d$:

$$J(A) = \frac{2}{\mu^2} (e^{-\mu d} (1 - 2e^{\sqrt{2}\mu} + e^{2\sqrt{2}\mu}))$$



In Figure 8.6 an example of a measured intensity scan is compared to this calculation. For fitting the calculated function to the measured intensities it was necessary to take an absorption coefficient of $\mu = 1,52 \text{ cm}^{-1}$. The different absorption coefficient to that of pure iron ($\mu_{\text{iron}} = 1,18 \text{ cm}^{-1}$) can be explained by an increase of the total neutron cross section at lower energies, the manganese content of the steel and an increased path length due to geometrical effects.

As a result of these investigations one can see that it is possible to determine the position of the sample's surface to a high accuracy (error < 0.1 mm).

Surface scan (vibrated sample), RH-collimator

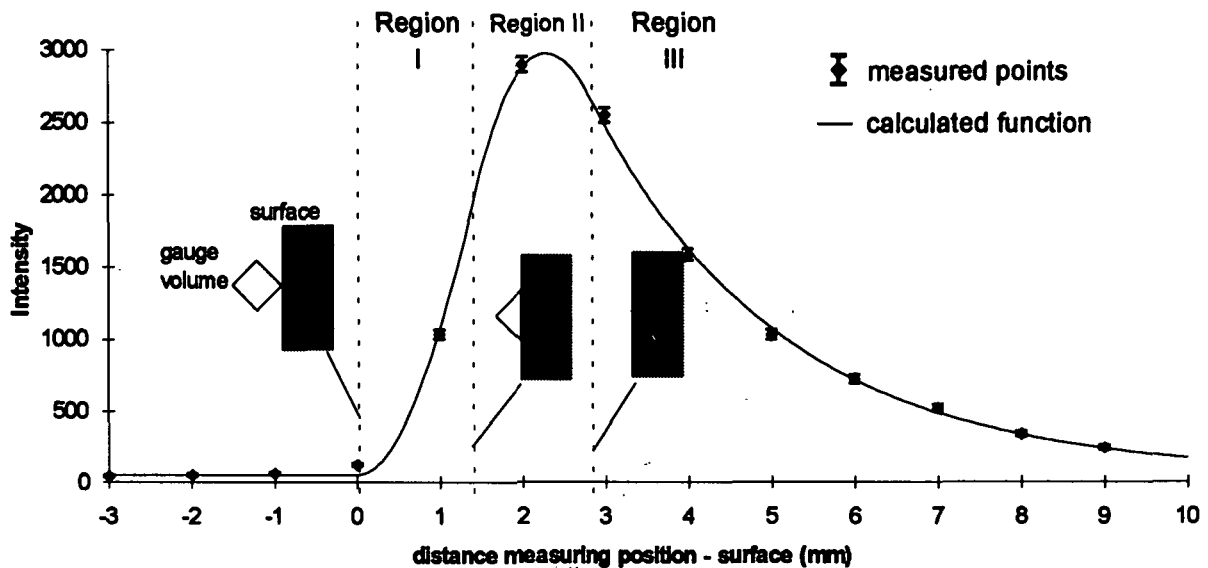


Figure 8.6 Surface scan fitted with the calculation seen above using least-squares-method

8.5 Macrostress measurements on ENGIN

Strain measurements have been performed in the three main directions (hoop, axial and radial) at nine points in different depth of the specimen walls. These positions were named according to the distance from the inner diameter in mm (position 2 to 18). In the following figures the different samples were marked in the following way:

as received (AS) □

vibrated (VIB) ●

heat treated (HT) ○

The diffraction data were analysed using the NISISREF batch refinement routines based on the CCL software at ISIS. The diffraction pattern were refined in the TOF region between 4000 μ s and 12500 μ s, which includes the bcc- reflections (110), (200), (211), (220), (310), (222), (321) and (400).

Using the lattice parameters and the d_0 -values the strain values could be calculated. The literature values of macroscopic elastic constants for ST52-3 were used:

$$E = 207 \text{ GPa}$$

$$\nu = 0,28.$$

The calculated values are plotted in Fig. 8.7 - 8.9. Using the error of the lattice parameters from the refinement procedure an uncertainty of the stress values of $\Delta\sigma = 20 \text{ MPa}$ was calculated.

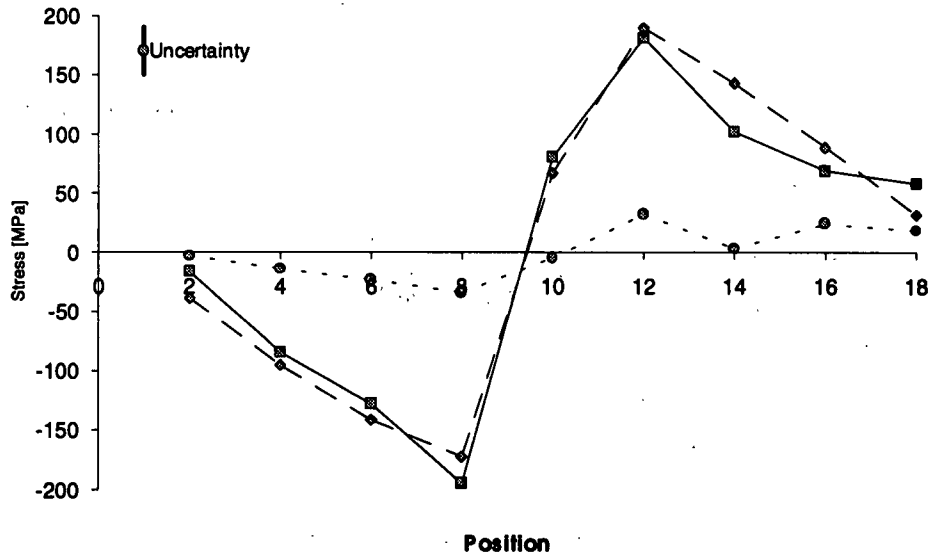


Fig 8.7 Stress state in hoop direction

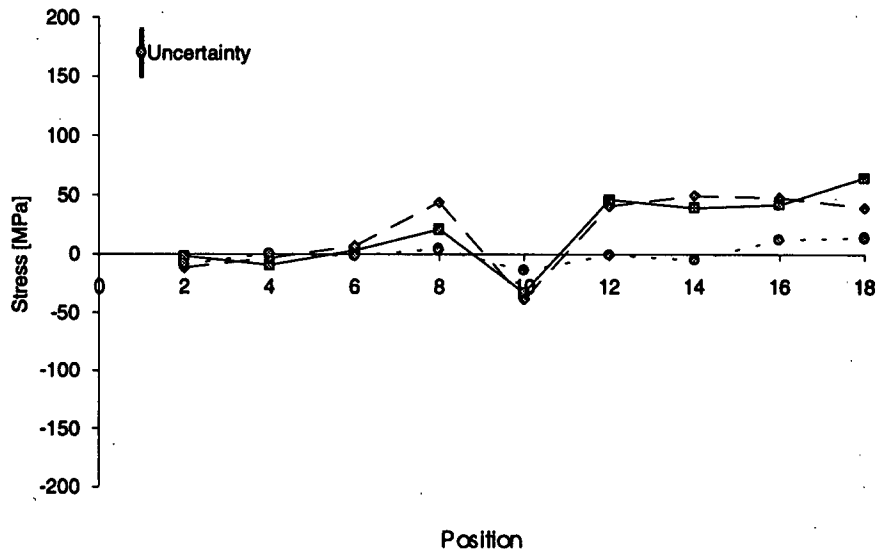


Fig 8.8 Stress state in radial direction

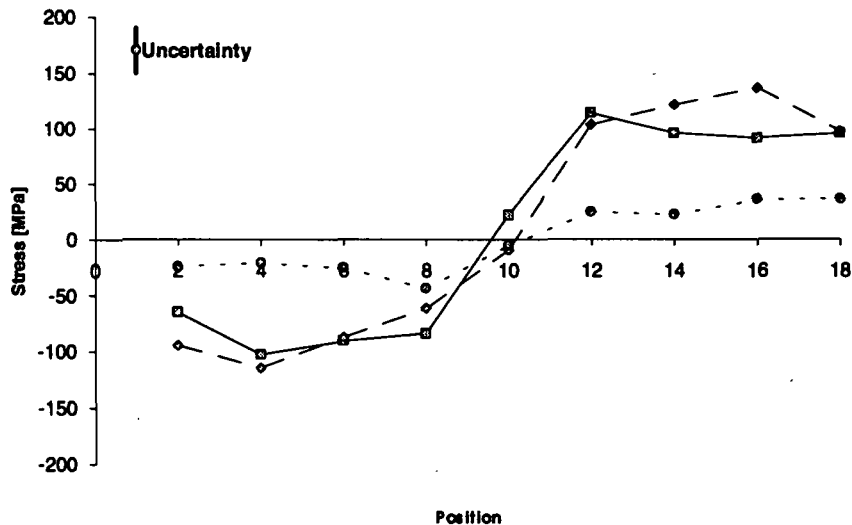


Fig 8.9 Stress state in axial direction (○ heat treated; □ as received; ◆ vibrated)

The measured stress state is mainly caused by two processes during the production of the samples: The plastic deformation from circular shape rolling of the plates results in tensile hoop stresses in the inner and compressive hoop stresses in the outer regions of the ring walls (cf. FSS-data). A similar behaviour is shown for a bending test reported in the literature.

This stress state is overlapped by elastic stresses due to the bending and welding, which produces a compressive hoop stress in the inner and tensile stress in the outer regions. The measured stress state is a result of the superposition of the plastic and elastic deformation of the rings, whereby the stresses due to the elastic bending are dominating.

The stress calculation shows, that the relatively large strains, which have been measured in radial direction, are caused by Poisson contraction and not by radial stresses.

The neutron diffraction measurements gave no significant macrostress relief by the vibrational treatment. If the uncertainty is taken into account, it can be said, that all nine points in all three directions give the same value for the 'as received' and vibrated sample. Most investigations on vibrational stress relief show similar results.

On the other hand the heat treated sample is almost stress free. In all directions the values of residual stresses smaller than 50 MPa were found. Thus the neutron diffraction measurements show an almost complete stress relief by the heat treatment.

In addition to the strain measurements at ENGIN further investigations were made at the Reverse-Time-of-Flight instrument FSS at the research reactor FRG-1 in Geesthacht. The aim was to investigate the strain distribution at the ENGIN measuring positions after relief of elastic macrostresses by cutting the sample along the welding seam.

The influence of stress relief treatments on microstresses was also looked for by investigating peak widths. The analysis of the data was done by single peak fitting. The RTOF-method used allows peak-fitting with a well determined peak shape function.

8.6 Peak widths

To investigate the influence stress relief procedures have on microstresses the sample dependent peak widths were analysed. Gaussian peak parameters for the sample's component of the total peak widths result from the fitting procedures were used.

While the peak widths in hoop direction are obviously affected by the stress relief by annealing, peak widths of the vibrated sample don't show any significant influence of stress relief neither in hoop nor in radial direction. This was also shown by the width data (expressed as σ_{Ref}) derived from Rietveld-refinements on ENGIN spectra. This can be seen in the following figures.

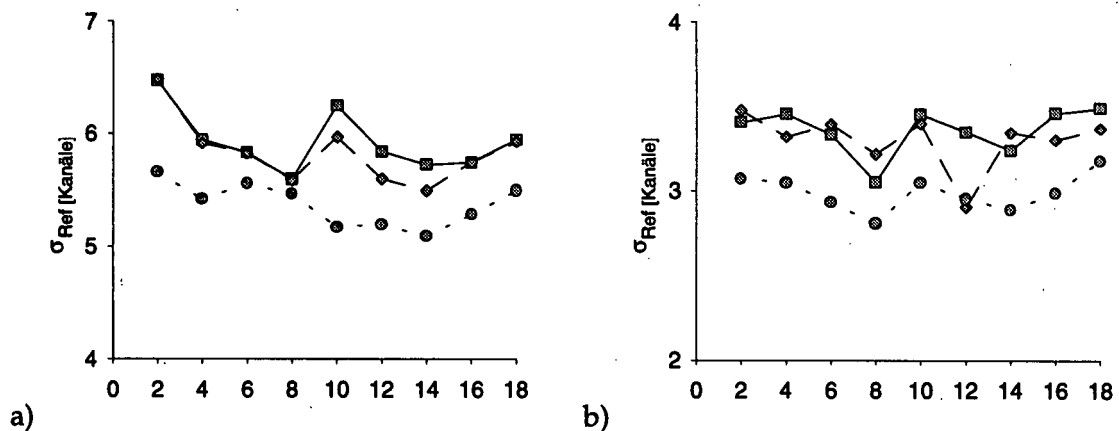


Fig 8.10: Peak width parameters (channels), hoop direction, a): (110)-reflections, b): (211)-reflections (○ heat treated; □ as received; ◆ vibrated)

Interestingly Fig.8.12 a) shows a significant difference between the Gaussian parameter of the heat treated sample and the vibrated sample. Data for the as received and the vibrated sample shown in Fig.8.12 b) are equal within the error.

Similar results were obtained from the FSS measurements as well.

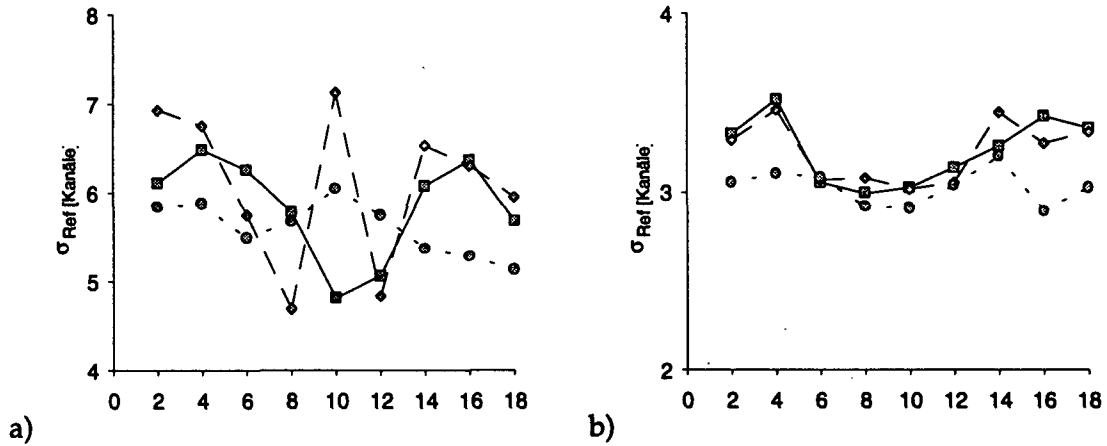


Fig 8.11 Peak width parameters (channels), radial direction, a): (110)-reflections, b): (211)-reflections (O heat treated; □ as received; ◆vibrated)

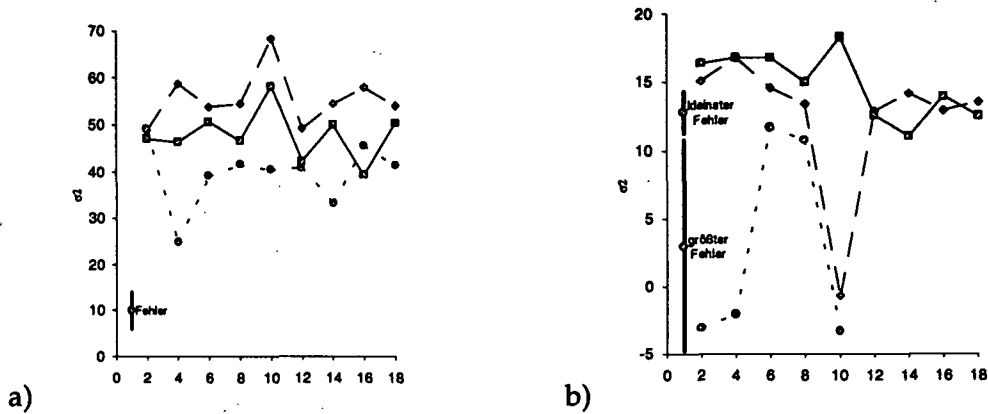


Fig 8.12 σ_2 -parameters from Rietveld-refinement over the region 4000 to 12500 μs . a):hoop direction, b): radial direction (O heat treated; □ as received; ◆vibrated)

8.7 Results & conclusions

Instrument performance

Besides the results on the VSR procedure the measured data also gives information on what measuring time is needed on steel samples. The standard time during our runs was 1 hour, using a gauge volume of $2 \times 2 \times 30 \text{mm}^3$.

For the right hand collimator the path length and therefore the error in strain was dependent on the measuring position in the sample. In Figure 8.13, the increase of the errors due to higher absorption in the centre of the sample is shown. For the right hand collimator, the errors vary between $35 \mu\epsilon$ and $75 \mu\epsilon$. For the left hand collimator a constant error of $60 \mu\epsilon$ was achieved. A higher accuracy was observed for the left hand collimator, if the longer penetration depth through the sample is taken into account.

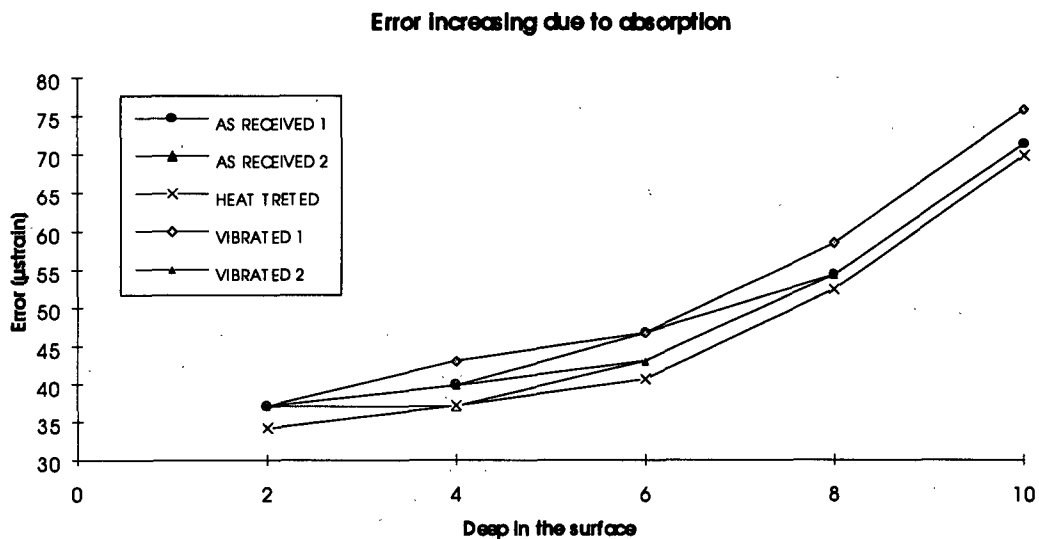


Figure 8.13 Measured errors due to decreasing intensity when reaching the sample centre

Putting the errors in the stress-strain relationship, stress values could be derived with an error of 25-30 MPa, if the elastic constants of the material are assumed to be well known. Because the absorption coefficient of the material is known, the intensity decrease due to absorption can be translated into a decrease of the measuring time for the points in the centre. For example, the centre point has an equivalent measuring time of only 6 minutes with strain error of about $70\mu\epsilon$. Hence the relationship between measuring time and error is approximately quadratic. For an error of $100\mu\epsilon$ a 3 minute measurement at a point 2mm below the surface is sufficient (gauge volume $2 \times 2 \times 30 \text{mm}^3$). This can be very useful, since the runs of the surface scan, which take 10 Ahrs could be used for also for strain measurements, if the strain caused by geometrical effects can be separated from the strain at the surface.

d₀ sample

For accurate stress/strain measurement the knowledge of the stress free lattice parameter is extremely important, since all data are related to this value. Producing a stress free sample is always problematic. The use of a cube spark eroded from the original material measuring close below the surface was found to give usable values. The assumption, that such a cube must be stress free, was proven by finding no significant changes of d-spacing when measuring the value in different directions of the cube.

Positioning of the d_0 -sample and the slit alignment also have a great influence on the experimental result. For example in our case, specially designed slits for the hoop direction were glued directly on the sample. When using strain values calculated from the original d_0 , measured with the conventional slit alignment, the stress equilibrium equations were not valid. Therefore the stress equilibrium equations were used to calculate a "new" d_0 in order to shift the strain values by a constant amount, sufficient to cause stress balance.

Vibrational stress relief

The differences of the strain in radial and axial direction between the 'as received' and the 'vibrated' sample are small. When using the code 2 refinement option the shape of the scans of the 'vibrated' becomes smoother and the maximum strain values decreased. The heat treated sample shows such a strong strain decrease, that it can be assumed to be almost stress free.

Another point of the investigation of the vibrational stress relief procedure should be a possible change in the microstresses, which have an influence on the peak shape and width which are parameters of the Rietveld refinement. From the analysis of the actual data no significant changes in the peak shape parameters were found.

The macrostrains resulting from the FSS-measurements show the same effects of the stress relief procedures as the ENGIN-measurements. Macrostress relief is only found for the annealing process, but not for the VSR-treatment.

The most interesting part of these investigations was the peak widths measured as Gaussian parameters fitted to single peaks. It was hoped that the assumed effect of the VSR-treatment on dislocation distributions could be found in smaller peak widths for the VSR-treated sample. This effect could not be shown by the measurements. The reason for this may be that it is not possible to measure a decrease of dislocation densities by the widths of Bragg reflections.

9 Investigation of Advanced Welding Methods and Postweld Heat Treatments

9.1 Introduction

In the manufacture of engineering components welded joints are often a critical component. The advanced properties of Nickel based superalloys (high temperature stability and strength) make them the material of choice for many applications. However, such materials are also difficult to weld, and advanced welding techniques such as the electron-beam or laser welding are often necessary.

In co-operation with the German aircraft manufacturer MTU Deutsche Aerospace (Motoren- und Turbinen-Union München GmbH) the residual stress state on laser welded (LW) and electron-beam welded (EBW) Inconel 718 plates have been measured by neutron diffraction.

On an identical set of samples a post weld heat treatments (PWHT), conforming to the method used by MTU, were performed. In order to test the efficacy of this stress relief procedure, the three-dimensional stress states before and after the heat treatments were measured.

This work was performed by the Institute of Pure and Applied Nuclear Physics group, University of Kiel.

9.2 Samples

The samples were supplied by our endorser MTU München. Instead of cylindrical components usually under investigation at the MTU welding research department, a simpler geometry of plates were chosen in order to simplify the neutron diffraction measurements. Two plates at a time of 8 mm thickness and dimensions of 90 mm x40 mm (100 mm x40 mm for the EBW) were welded together to result in the sample outlines shown in Fig. 9.1.

Overall four different samples were under investigation. Two of these samples were laser welded under identical conditions, the other two electron-beam welded. One sample of each welding type got a post weld heat treatment. After a heating ramp at 10deg/min the samples were held at 635°C for 4 hours. The treatment was finished by an accelerated cooling process achieved blowing air around the samples. The notation of all samples is given in Table 1.

The material of all plates was Inconel 718® (NiCr19NbMo), a Ni-based superalloy mainly used in high temperature applications (up to 700°C) like turbine and reactor construction. The chemical composition is given in Table 2.

Sample	Condition	Dimension [mm]
MTU1	LW, PWHT	90x80x8
MTU2	LW	90x80x8
MTU3	EBW, PWHT	100x80x8
MTU4	EBW	100x80x8

Tab 1. Sample notation and dimensions

Al	Co	Cr	Fe	Mo	Nb+Ta	Ni	Ti
0.6	0.5	19	18.1	3.1	5.3	52.5	0.9

Tab. 2: Mean chemical composition of Inconel 718 in weight percent

9.3 Measurements on ENGIN

9.3.1 Measurement Positions

Welding methods differ in their heat impact on the components, which causes the development of the residual stress state in and around the weld. The aim of the neutron diffraction measurement was the investigation of principal differences in quality and quantity of the 3D-stress field between a laser and an electron-beam weld. Another major aim was the investigation of the efficiency of the heat treatment process in reducing the welding stresses.

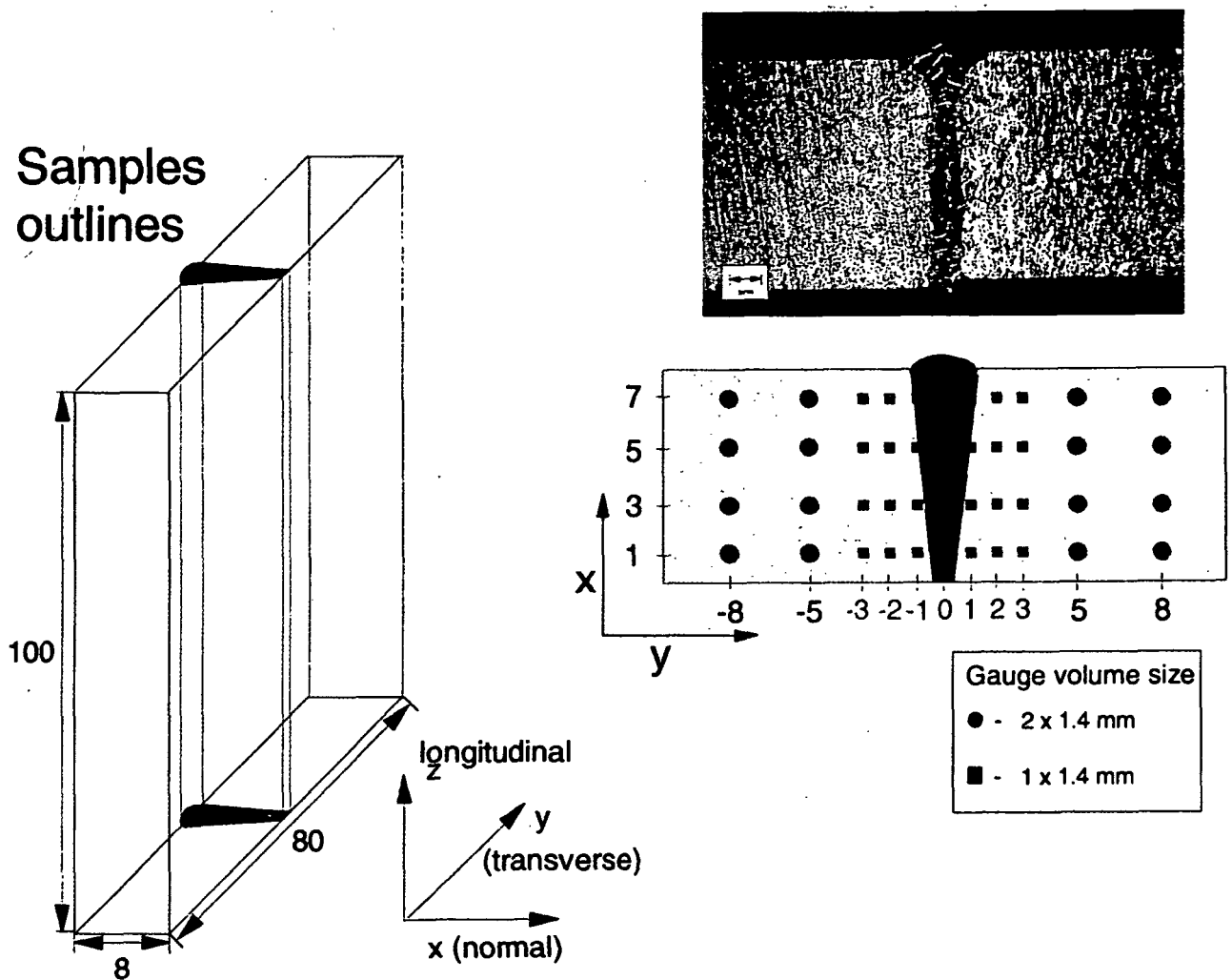


Fig 9.1. Sample outlines and definition of the measuring directions and positions

NORMAL + TRANSVERSE

NORMAL + LONGITUDINAL

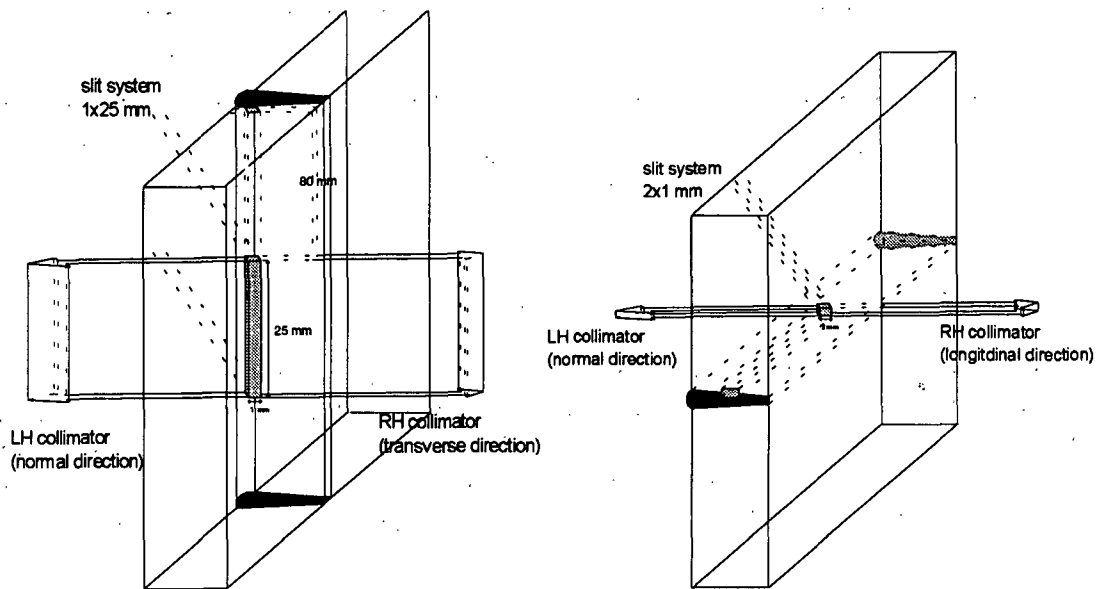


Fig 9.2 Gauge volume definition and sample orientation for different measuring directions

The measurements have been performed during the 'PREMIS' cycles in May 1995 by measuring the 'as welded' (AW) condition (samples MTU2 + MTU4) and in July 1995 ('heat treated' (PWHT) condition (MTU1 + MTU3)). Lattice strain has been measured in three directions of the plates (normal, transverse and longitudinal to the welding direction) as defined in Fig 9.1 and 9.2. Under the assumption that the principle strain directions follow these directions, the stress state could be calculated. However, this assumption should be treated with caution, as recent investigations have suggested that this may not be true [1].

Characteristic of both welding methods is the narrow welding seam and heat affected zone (HAZ), which are just a few millimetres wide. Due to the high energy flux density in the focused laser/electron-beam depth-to-width ratio up to 5:1 for the weld line are possible. Compared with a typical ratio of 1:1 for conventional WIG welding this is a great advantage of the two investigated welding methods, since narrower welds and HEZ reduce the heat impact and shrinking forces, which leads to lower residual stresses and distortion.

Hence, for the neutron diffraction measurements the most distant point of the strain map was chosen to be ± 8 mm perpendicular to the weld line. The measuring positions for the stress mapping are shown in Fig 9.1 (left). Although the stress field on both sides of the weld should be symmetric, both sides were actually measured for reliability reasons.

Large stress gradients which were expected close to the weld call for a the slit width of 1 mm at measuring points less than 3 mm from the weld line. Since the stress state centre of the sample was uniform along the Z axis, a slit height of 25 mm for normal/transverse direction measurements was appropriate (cf. Fig 9.2). Hence, the gauge volume became 1x1.4x25mm.

For the measuring positions 5 mm and 8 mm from the centre of the weld the slit widths was doubled to save measuring time, since this region shows almost no stress. In order to achieve an uncertainty in the strain values of about $100 \mu\epsilon$ the typical measuring time for one point was 40 - 20 μ Ahrs (i.e. 15 - 7.5 minutes) for the inner/outer region where the sample beam path was about 12 mm.

For the measurement in the longitudinal direction a 90° rotation of the sample was necessary (Figure 9.2 right). In this position the beam height defines the measuring region relative to the weld. With a slit width of 2 mm the gauge volume decreases to 2x1.4x1 mm (2x1.4x2 for points at 5 mm and 8mm). For the longitudinal strain values an uncertainty of 200-300 $\mu\epsilon$ after 100 μAhrs had to be accepted due to the large number of positions under investigation. To achieve the same accuracy as in the normal/transverse direction 480 μAhrs (3 hours of measuring time) would have been necessary for each point.

9.3.2 Surface scans

Due to the small sample thickness, a precise alignment of the sample was necessary. Therefore after the optical alignment with the telescope a surface scan was performed on all samples, before the strain mapping started. Usually the surface position determined from the optical alignment has to be corrected by about 0.5 mm (see Fig. 9.3). This correction value shows, that if positioning to better than 0.5 mm is needed, it is worth to spend half an hour to perform a surface scan before starting a strain map scan.

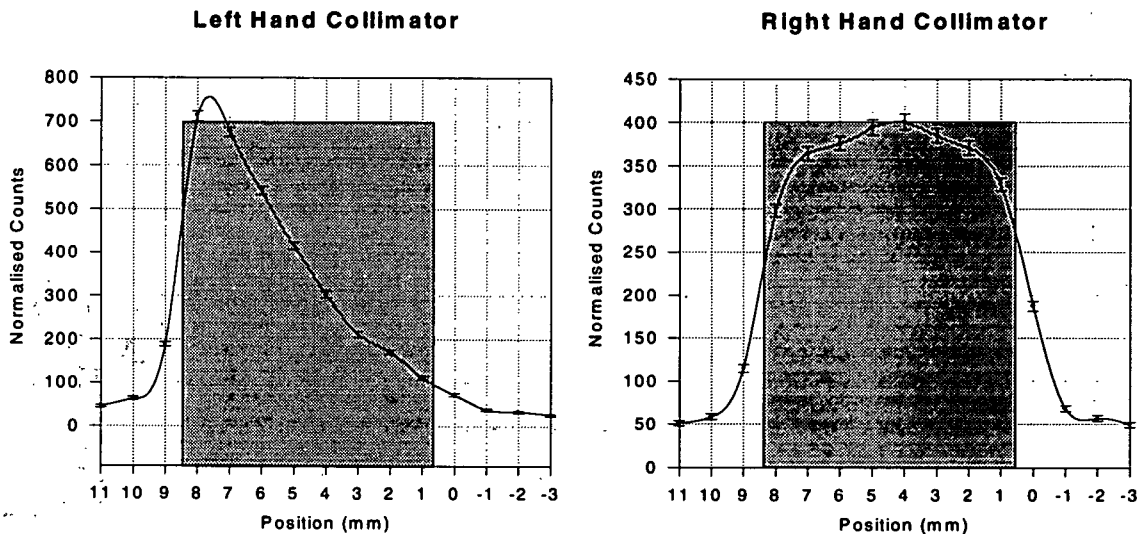


Fig. 9.3: Typical result of a surface scan (performed on the MTU3 sample)

9.3.3 d_0 -values

From experience and preliminary investigations it was known, that a noticeable stress state exists just in a narrow range around the weld line. Therefore it was decided to use the d_0 -value observed on a point on the sample 1.5 mm below the surface (gauge volume fully inside) and 20mm distance from the weld line as the stress free reference value.

9.3.4 Strain maps

All diffraction patterns were refined in the TOF region 4000 to 12500 μs [fcc-reflections (111), (200), (220), (311), (222), (400), (331), (420) and (422)] using the batch refinement routines based on ISISREF code. From the lattice strain a stress state could be calculated by using the macroscopic elastic constants for Inconel 718: Young's modulus: $E=205$ Gpa, Poisson's ratio: $\nu=0.286$. On the following pages the calculated stress values are plotted for all samples in figure 9.4 to 9.7.

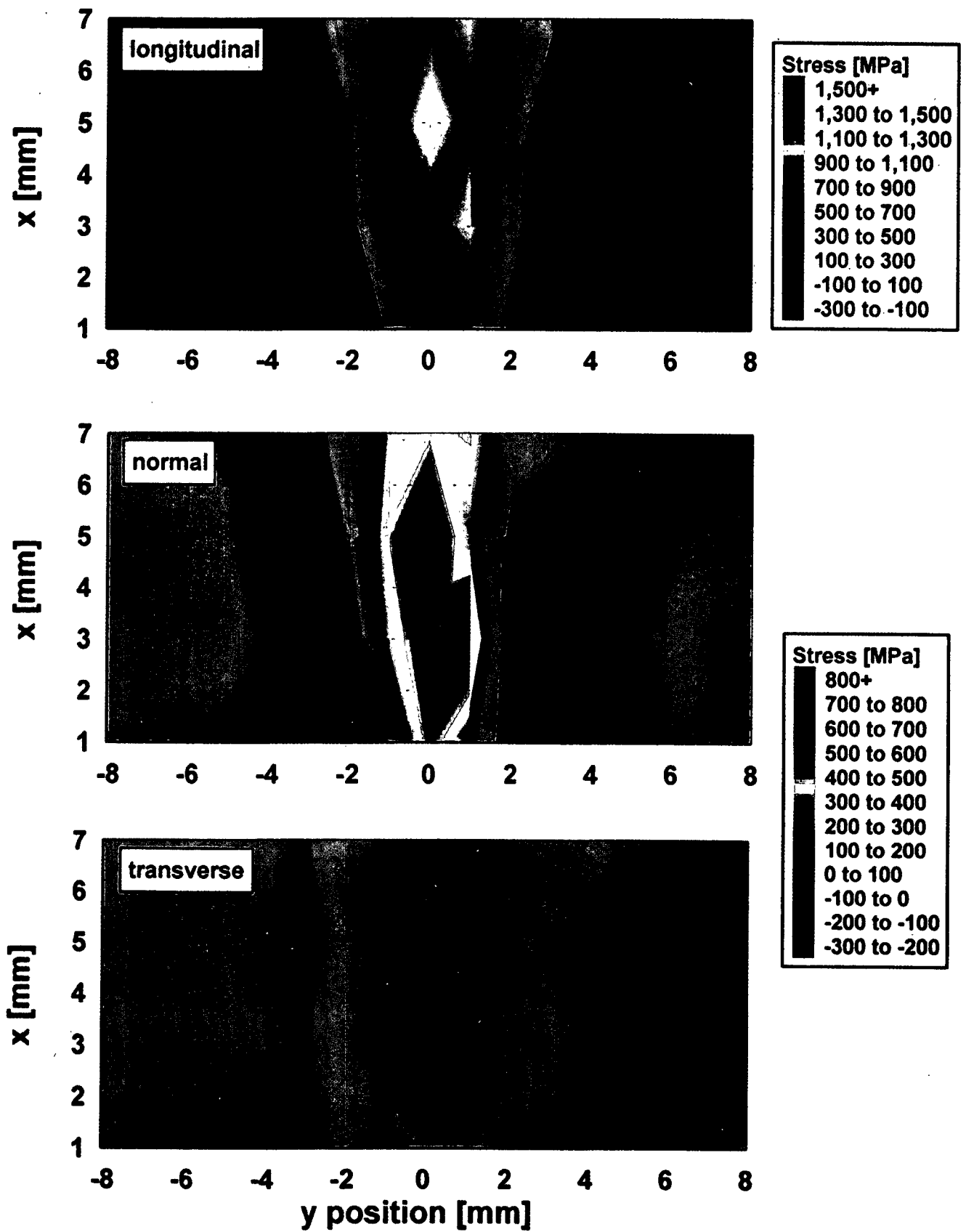


Fig. 9.4 Stress state of the laser-welded sample after heat treatment (no pseudostrain correction)

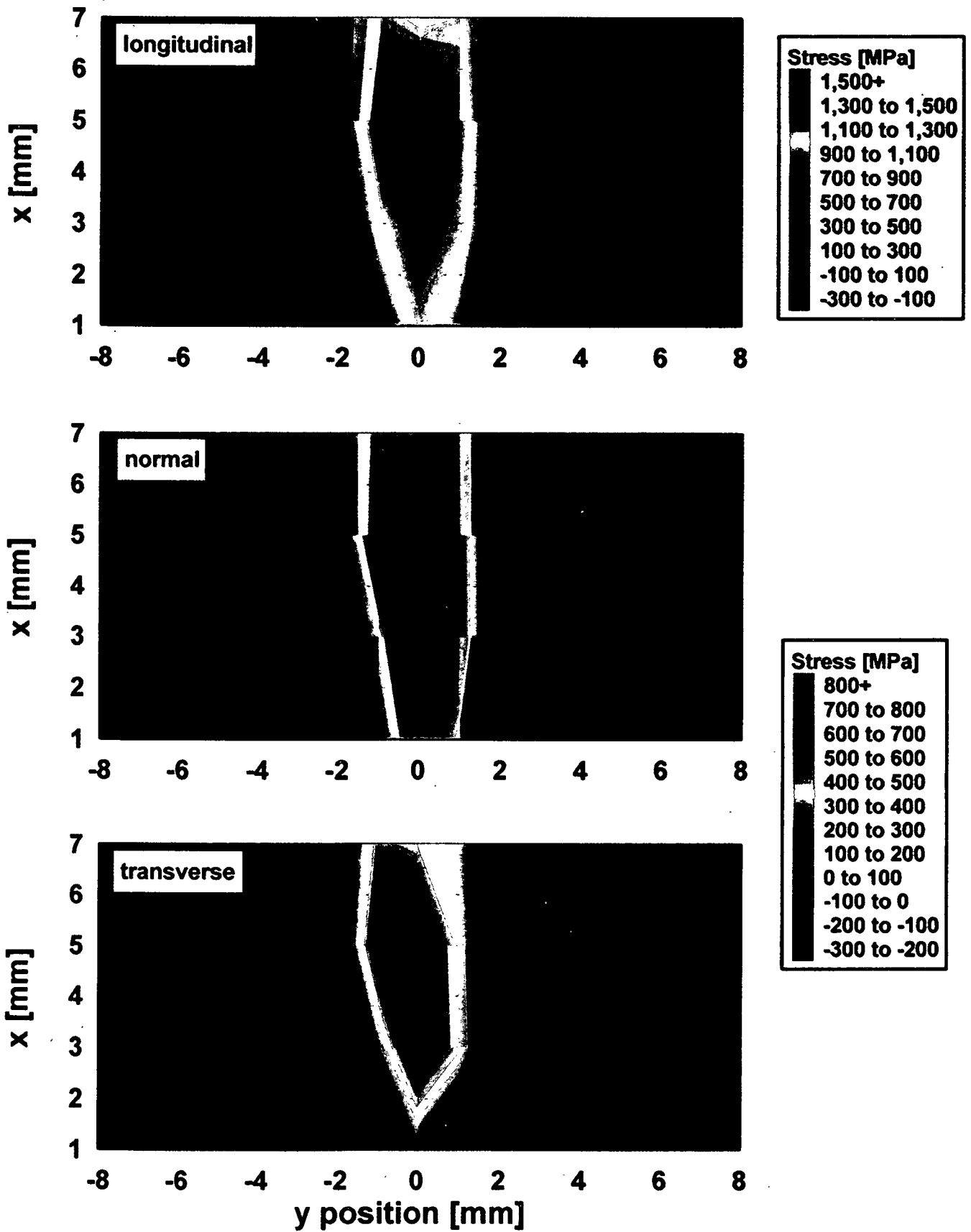


Fig. 9.5 Stress state of the laser-welded sample 'as welded' (no pseudostrain correction)

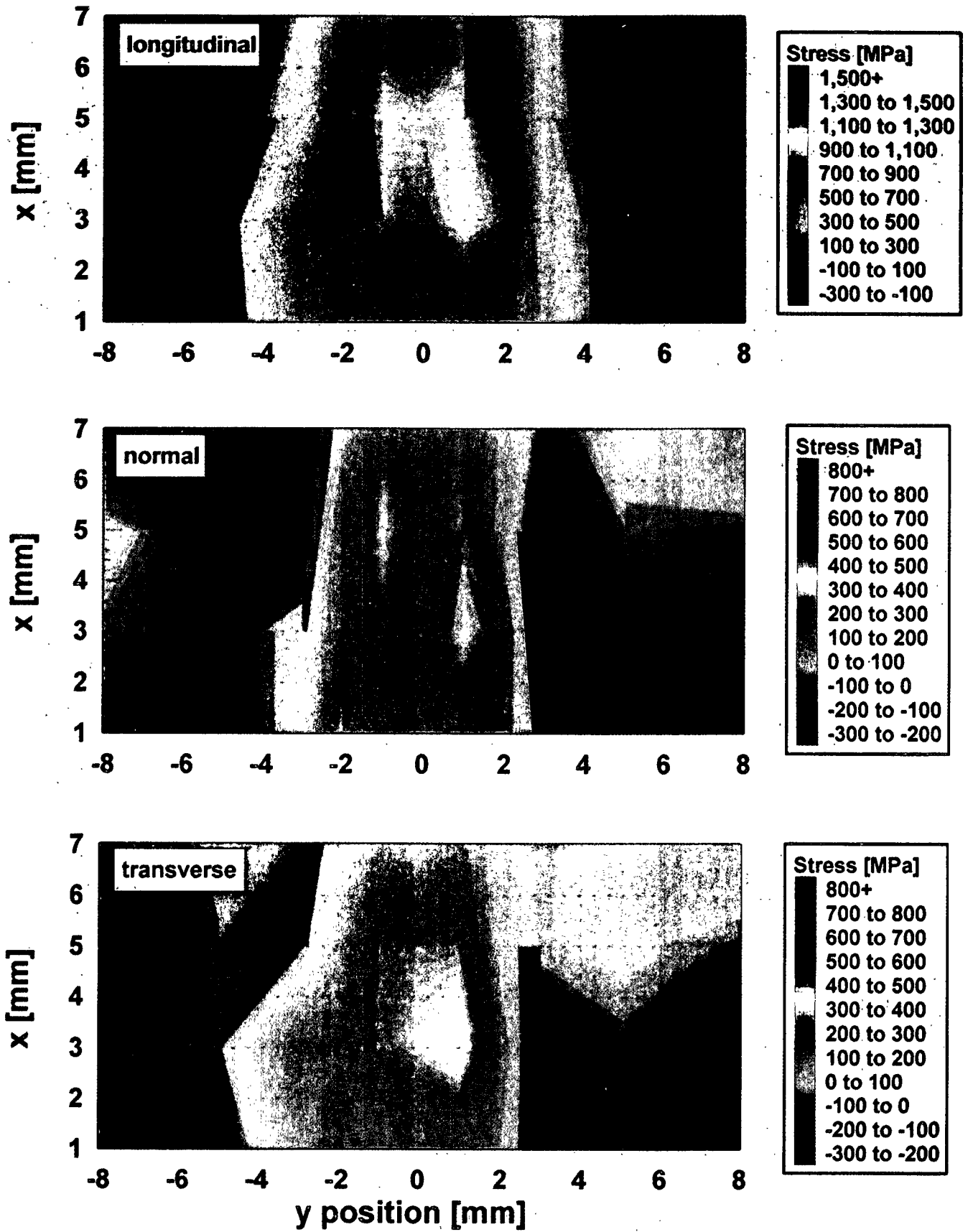


Fig. 9.6 Stress state of the electron beam welded sample after heat treatment (no pseudostrain correction)

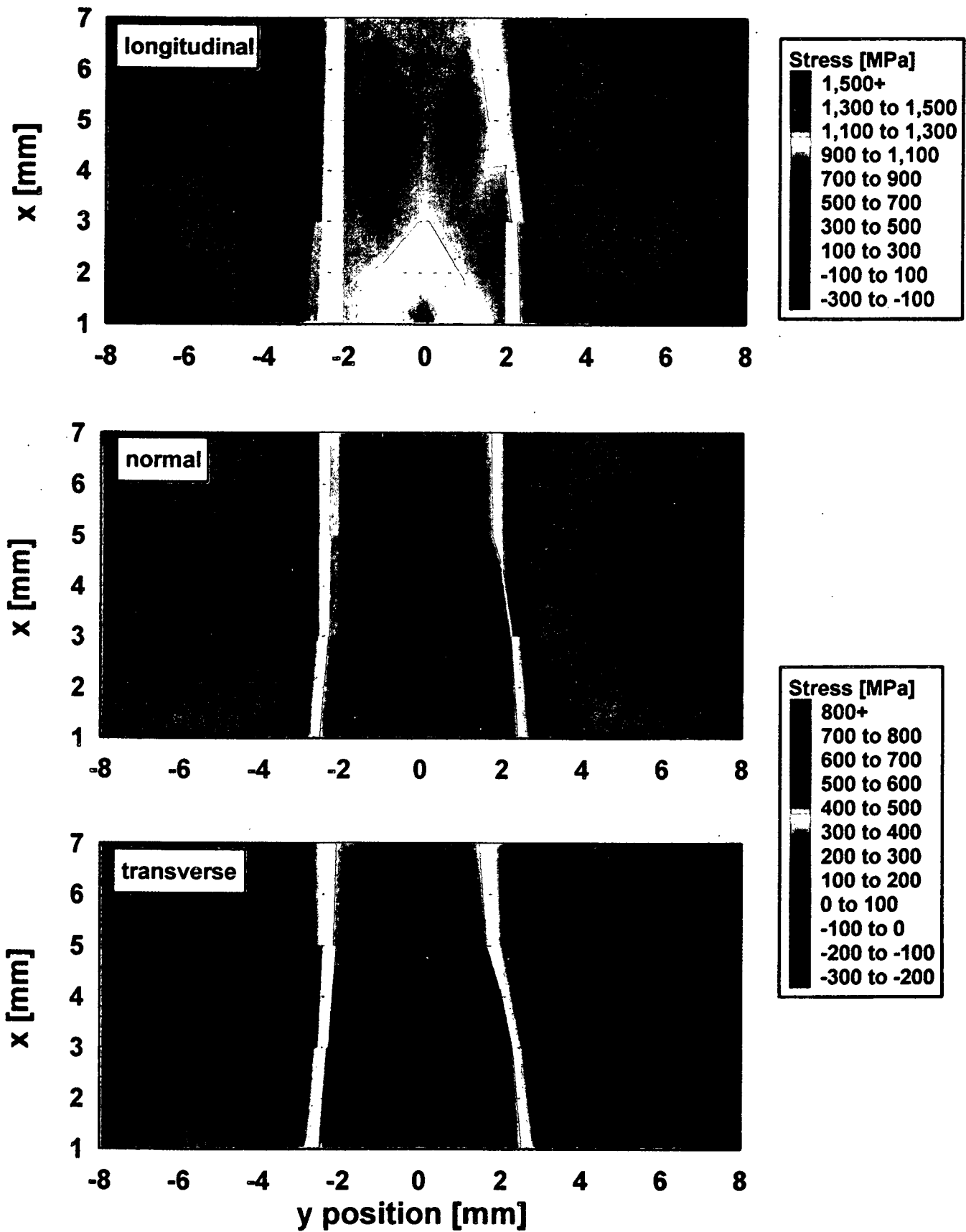


Fig. 9.7 Stress state of the electron beam welded sample 'as welded' (no pseudostrain correction)

9.4 Compositional strain

When analysing the data from the 'as welded' samples MTU2 and MTU4 measured at the first cycle in 1995, extremely high tensile stress values were calculated from the lattice strains. Values in the range (and sometimes above) the yield strength of Inconel 718 (at 1200 MPa) were found for the points in the weld line. After a discussion of these results with the research department of our endorser MTU, we were sure this was an artefact from compositional change in the weld and the heat affected zone, which causes a 'compositional pseudostrain'.

In Nickel based superalloys a very well defined compositional structure is created by a special heat treatment process in the production (e.g. for Inconel typically: solution treatment at 955-980°C (1h), cooling by air/water, precipitation hardening at 720°C (8h), cooling at 50°C/h to 620°C, holding at 620°C (8h)). After this process the compositional structure consists mainly of three components: γ -solid solution, the γ' -matrix and various carbides. In the diffraction pattern the γ - and the γ' -matrix could not be separated.

The undefined heat deposition in the weld and HEZ during the welding process causes a modification in the compositional structure and a change in the lattice parameter measured in the weld. Such a 'pseudo'-strain is often observed in diffraction strain measurements in welds. For example, in our research group at the GKSS Research Centre during residual stress investigations on an Inconel 718/Waspaloy inertia welded tube, where neutron diffraction strain measurements have been performed mainly at the AECL [2]. In this work a correction value was defined (so called Δ^{chem}), which was calculated from stress balance conditions and was dependent on the distance from the weld line. The position dependence of this Δ^{chem} -value is plotted in Figure 9.8. In this case a correction had to be made over the weld and HEZ. It's value decreases with increasing distance from the weld.

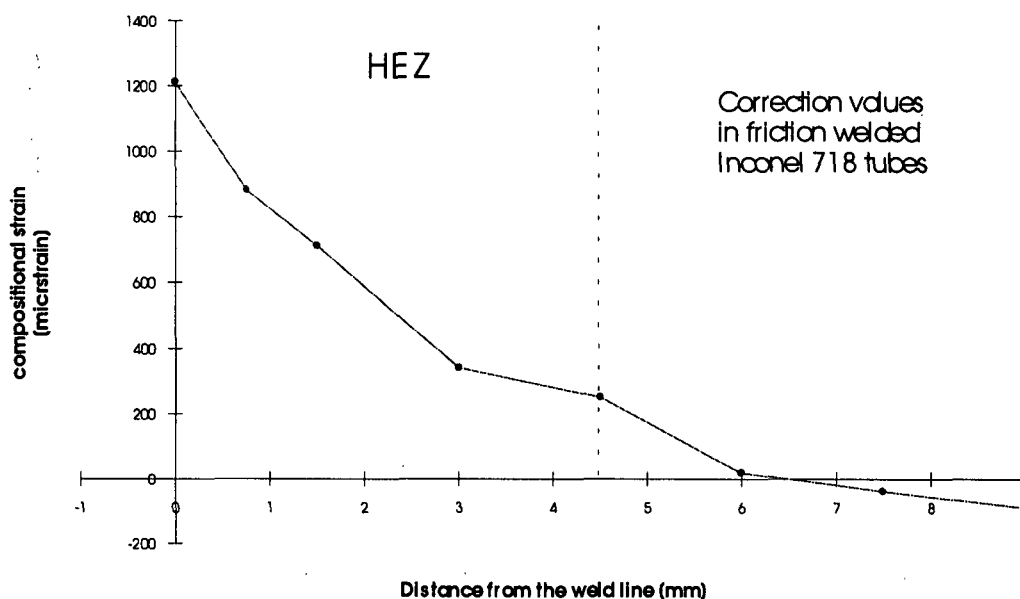


Fig.9.8 : Correction values observed on an inertia welded Inconel 718 tube

9.5 Stress balance calculations on the LW sample MTU2

In order to determine the influence of compositional change on the lattice parameter and to get a correction value -at least for the centre of the weld of one sample-, it was decided to spend a part of the beamtime scheduled for the PWHT samples in cycle 2/95 on the measurement of additional points to allow a stress balance calculation.

In order to perform a stress balance calculation in general the three-dimensional stress has to be measured covering the whole sample. As a practicable approximation to this requirement, for the laser beam welded sample MTU2 the plane in the centre of the weld was scanned using a gauge volume size of $10 \times 1 \times 1.4 \text{ mm}^3$ for the normal/transverse direction and $1 \times 2 \times 1.4 \text{ mm}^3$ for the longitudinal direction (Figure 9.2). The strain/stress values were computed by varying the d_0 -value until the transverse stresses were 'balanced'. The stress maps calculated in the weld plane are also plotted in Fig. 9.9.

By comparing the d_0 -value computed from stress balance with the lattice parameter measured at the position 20 mm from the weld, which was used before as the stress-free d -spacing, the 'pseudo'-strain could be calculated. The correction value was 0.0052 \AA or $1470 \mu\epsilon$. These calculations show the large influence of compositional change on residual stress measurements in welds. It has to be notified, that $1470 \mu\epsilon$ is close to the value of $1210 \mu\epsilon$ for the weld line of the friction welded tube on the same material. In principle the compositional strain has to be measured for all distances from the weld and for both welding methods. Due to the large number of points and limited beamtime this was not practicable.

However, the significance and use of these calculations must still be examined. Can the compositional changes be assumed to be the same for all measuring directions? And why should it be uniform over the plane, since it is known, that the outer and inner regions got a different heat impact? How to separate between 'pseudo' strains and hydrostatic stresses which could develop in the weld? All these questions have to be kept in mind when using such corrections.

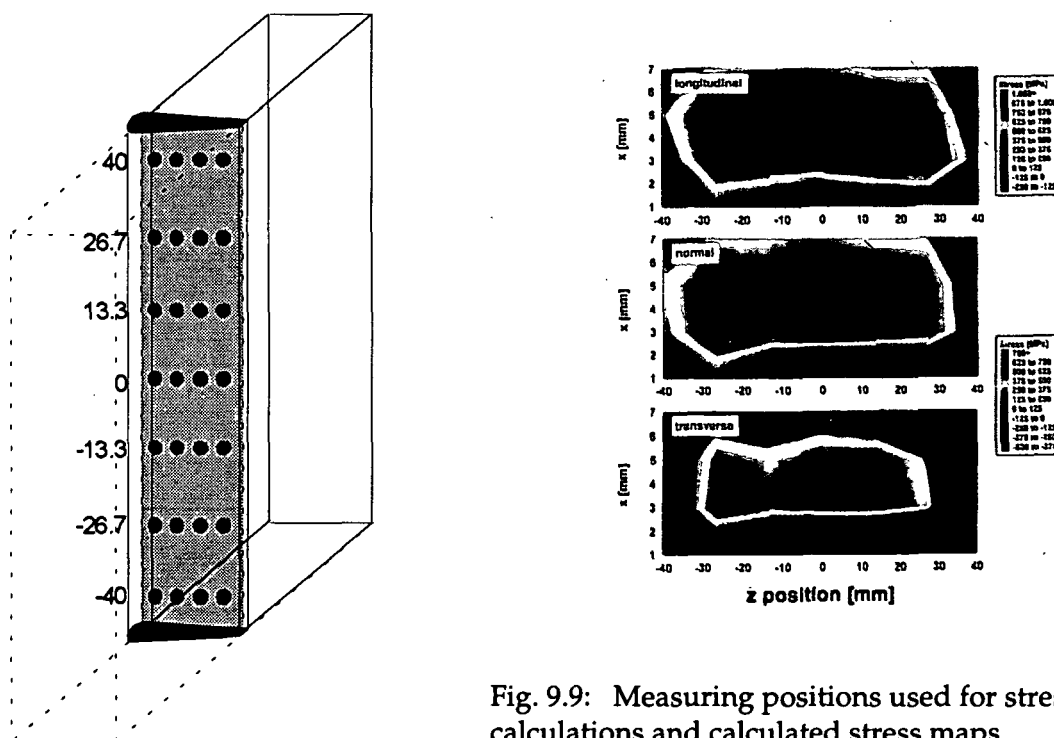


Fig. 9.9: Measuring positions used for stress balance calculations and calculated stress maps

Further investigations could prove, whether the application of a unique correction value for each distance from the weld is sufficient. Therefore the next step will be to cut the weld region of the sample into little cubes (about $1 \times 1 \times 10 \text{ mm}^3$ in size) and get position-dependent stress free lattice spacings. The removal of the surrounding material should eliminate most of the macroscopic residual stresses from the welding. This sectioning has been applied successfully in various diffraction stress investigations on welds. In addition, MTU will perform stress measurements on several positions using the hole drilling technique.

9.6 Corrected stress values for the MTU2 sample

In principle it is impossible to evaluate the correct stress values in the weld just by using one correction value computed from stress balance conditions in the weld. But, in order to get a rough idea about the actual stress state the following assumptions were made for the laser welded sample:

1. The heat affected zone is 2 mm wide.
2. The compositional 'strain' has the same value in all sample directions and decreases linearly with the distance from the weld line.

With this assumption the strain parameters were shifted and the 'true' stress state computed. In Fig 9.10, a comparison between the longitudinal stress state before and after the correction is plotted. A dramatic quantitative and qualitative change in the stress state could be seen easily. In the corrected stress map the maximum stress is found in the HEZ and not in the weld line (see stress map 'correction 1'). Also the maximum stress values decrease from about 1500 MPa to 1000 MPa, which is still a high value, but is now smaller than the yield strength of the material.

9.7 Comparison of the stress state of the electron and laser beam weld

Although the absolute stress values could not be worked out yet, some difference between the stress state in the laser welded and the electron beam welded sample could be seen already from uncorrected stress maps. As usually found in welds for both samples the high tensile stresses were measured for the longitudinal (=welding) direction.

The main difference between the two welding methods was found in the geometrical range of the stress field. While the laser welded sample MTU2 was almost stress-free at 3mm distance from the weld, in the EB welded sample MTU4 up to 500 MPa were measured in longitudinal direction. In the EBW sample the highest stress values were found 1 mm from the weld line in the HEZ. In the laser welded sample MTU2 the uncorrected data give the highest stresses in the centre of the weld were the 'pseudo' strain correction shifts the maximal values to the HEZ.

The stresses in normal and transverse direction are smaller but also tensile in the weld region. Apart from the width the stress states of the EBW and LW samples are comparable in their distributions and values.

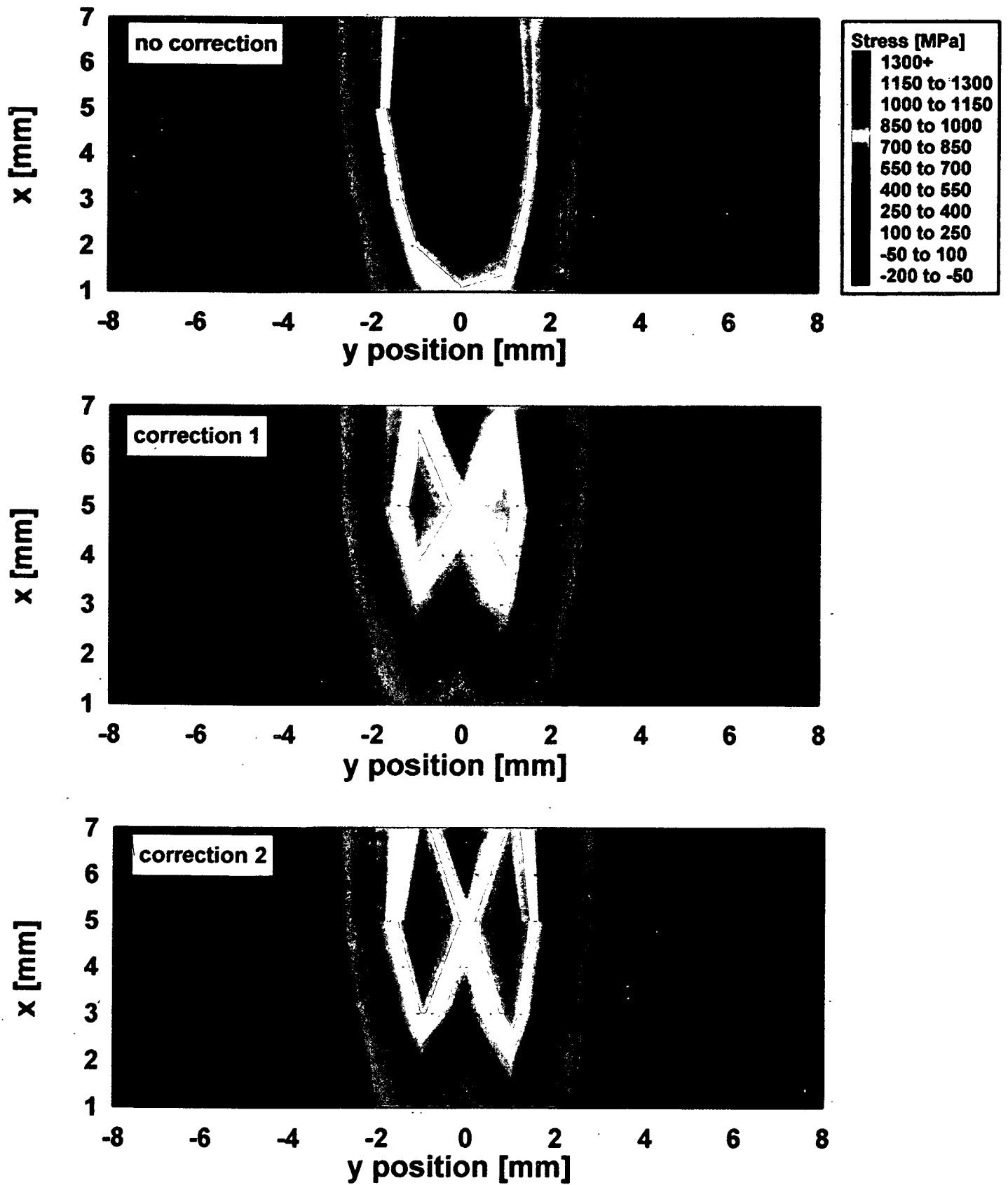


Fig. 9.10 Longitudinal stresses MTU2 sample for different pseudostrain corrections

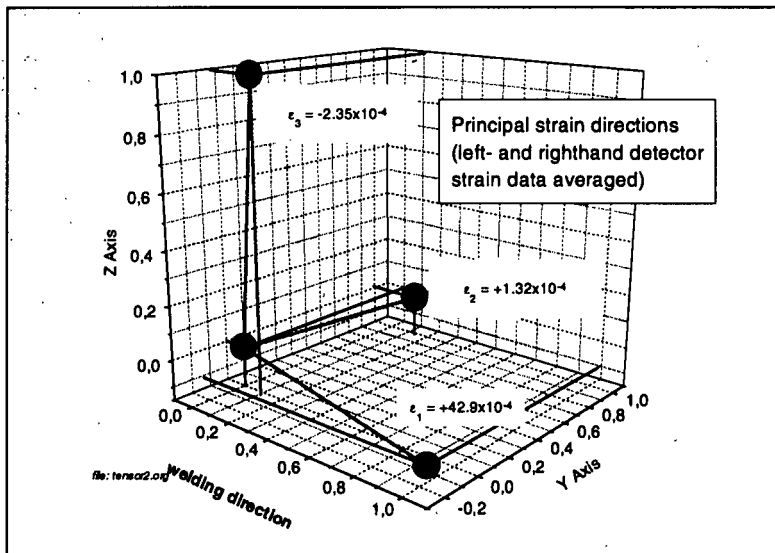


Fig. 9.11 Principle strain directions derived from 24 angular positions of a centre-of-weld scattering volume

Full Tensor Measurement

In order to check the assumption made during the stress calculations, that the principal stress directions correspond with the sample axis, a full tensor measurement was performed at the centre-of-weld of the LW sample MTU2. The gauge volume size was $2 \times 2 \times 1.4$ mm. Lattice strain was measured in 12 different angular positions on both detectors. Although the left and right detector give a slightly different strain tensor, the Eigenvector (principal strain directions) of the average of both detectors is almost parallel to the sample axis system (see Fig. 9.11).

9.8 References

- [1] R.A. Winholtz and A.D. Krawitz: The Relaxation of Residual Stresses with Postweld Heat Treatment in a High-Performance Weld Measured with Neutron Diffraction; Metall. Trans. A, 1995, Volume 26A, pp. 1287-95
- [2] J. Schröder: Untersuchung über den Eigenspannungszustand in reibgeschweißten Rohren von Superlegierungen mit Hilfe hochauflösender Neutronendiffraktometrie], Dissertation TU Hamburg, Harburg 1993

10 Time-Resolved Studies of Thermal Cycle-Induced Strains in Composites

10.1 Introduction

The overall objective of this aspect of the PREMIS project was to develop a technique for measuring rapidly varying thermal cycle strains within composite materials. To achieve this end the project aims were:

- to develop a system capable of monitoring the dynamic variation in the elastic strain in two phase systems undergoing much more rapid thermal cycles than any previously possible measurements.[1, 2], both with and without an applied load
- to record the strain variation within the phases of an Al/SiC whisker composite as a function of the thermal cycle and to compare this with finite element models

If these objectives could be reached, the programme would have provided the *first* direct measurements of creep and plastic behaviour occurring during thermal cycling.

10.2 The New Experimental Technique

Since the data collection time required to acquire sufficient diffracted intensity to determine phase strains on ENGIN is usually over an hour, a new method needed to be developed to record strain variations during thermal cycles of about 10 minutes duration. In order to escape from the constraints dictated by long collection times we have developed a **novel stroboscopic data collection system**. The idea being to divide up the thermal cycle into a number of segments, typically 16. Neutrons collected during each time segment are stored separately to give 16 separate diffraction profiles representing the mean lattice spacing during that segment. Neutrons from a particular segment from the following cycles are added to those from the same segment in the first until enough neutrons have been collected to produce statistically significant results. This stroboscopic system relies on the fact that, once a short incubation period has been exceeded, the strain changes during each cycle are the same - a fact verified by experiment.[3, 4].

In order to realise this idea a rig was constructed by the Kiel group to allow rapid and accurate variation of the temperature of the composite specimens. This uses two water-cooled, elliptical reflector, infra-red furnaces. This offers a direct line-of-sight to the neutron beam and allows external monitoring of the specimen dimensions by means of a scanning laser extensometer. This method of heating, with efficient water cooling of the furnaces combined with heat input localised to the focal point of the elliptical reflectors, was chosen because of the high temperature sensitivity of the mylar vanes of the focusing collimator. In order to protect the collimators, a thermally sensitive safety switch monitors the external temperature of the system, shutting off all power to the furnace if the collimator temperature exceeds 40°C. Further, a static load can be applied by a dead-weight system. The rig is shown in Figure 10.1. Central to the successful completion of this experiment, is the stroboscopic data binning system described above. The recording bin is incremented by a pulse from the furnace controller when the correct part of the thermal cycle has been reached. Registry between the thermal cycle and the acquisition cycle is maintained by a characteristic double pulse at the start of each cycle. This acquisition process requires approximately 16Mb of RAM to record the 16 diffraction profiles simultaneously.

While the recording of thermal mismatch strain variation for different thermal cycles and applied loads can go a long way to explaining the behaviour of two phase systems, deeper insights can really only be gained by the interpretation of the results in the light of models of their behaviour. For this reason two types of model were also developed. The Eshelby model is a very powerful approach for predicting the internal stresses in two phase systems and is especially good for behaviours dependent upon field-averaged stresses or strains, such as thermal expansion or stiffness. However, it is of limited use for inelastic effects, such as plasticity and creep, which are dominated by local conditions. For this reason a finite element model was also developed. Clearly modelling a real distribution of reinforcing whiskers would place huge demands upon computing resources. The approach followed has therefore been to approximate the randomly distributed, but well-aligned short whiskers by a regular array of aspect ratio 5 whiskers. The appropriateness of this assumption has been discussed elsewhere [5, 6]. The behaviour of the matrix is modelled using constitutive equations based on the tests carried out by Clauer and Hansen [7] on nominally identically prepared unreinforced material. Two three dimensional arrangements of fibres were studied; a staggered and an aligned case, as proposed by Levy [8], and the details are given elsewhere [5, 9]. A range of models have been used to describe the matrix behaviour, but these can be divided into those in which the matrix is perfectly plastic, and those in which both plasticity and creep can occur.

10.3 Results

The experimental neutron strain results have been extremely exciting; giving the first recorded information about the elastic strain changes occurring during rapid thermal cycles, which could also be correlated with conventional macroscopic observations. The ENGIN data acquisition system, including the stroboscopic software binning, worked with few problems. A wide range of experiments have been monitored, both with and without applied loading. Cycles ranging from a top temperature of 425°C to a minimum temperature of 150°C have been followed, with ramp rates up to 50°C/minutes, and loads of 25, 35 and 45MPa. Space does not permit us to show the whole series of results here, but much of the work is described in the following papers [5, 9-12].

Reference stress-free lattice parameters were determined for free SiC whiskers placed in a quartz tube at both room temperature and 350°C, thus allowing a (linear) CTE to be determined. An unreinforced alloy produced by the same route as the composite was examined at several temperatures between 25°C and 425°C in order to determine the CTE curve and stress free lattice spacing of the matrix. These values (i.e. $\alpha\Delta T$) were subtracted from the composite strains in order to deduce the elastic strains.

10.3.1 A comparison of static and thermal cycling creep rates

The drastic acceleration of composite creep behaviour under load brought about by thermal cycling can be seen clearly in Fig. 10.2. Here the macroscopic strain determined by laser extensometry experiments is shown [5]. The thermal cycle excursions were from 150 to 350°C, the isothermal test was carried out at the diffusional mean temperature of 300°C (i.e. the static temperature at the which the creep rate for the unreinforced alloy would be the same as the average over the 150 to 350°C thermal cycle). Yet even at less than half the applied load, the thermal cycling strain rate is much larger than the isothermal rate.

10.3.2 The effect of Increasing the Temperature Excursion ΔT on the creep increment

The effect of changing the magnitude of the temperature excursion can be seen in Fig 10.3a). Here the maximum temperature of the cycle has been fixed and the magnitude of the cycle excursion increased by lowering the minimum temperature. The fact that the strain per cycle increases from left to right despite the fact that the mean cycle temperature is being reduced, indicates the crucial role of the increased thermal misfit stresses in dictating behaviour. Upon decreasing ΔT , the misfit stress arising from the misfit strain ($\Delta\alpha\Delta T$) eventually becomes less than the matrix yield stress and the creep rate asymptotes to the 'isothermal' creep rate, i.e. that which would occur in the absence of thermal misfit stresses.

The difference between the longer duration constant ramp rate (therefore longer time) cycles and the constant time cycles is the result of the extended opportunity for creep. Note that the strain rate in 'isothermal' plateau (i.e. when ΔT become small) is very low in figure 3b compared with 3a because of the lower 'isothermal' creep rate associated with the lower diffusional mean temperature in this case. Thus to obtain large net cycle strains, both creep effects (high T) and plasticity (large ΔT) are required.

10.3.3 'Poisson's ratio' changes during thermal cycling

The monitoring of axial extension alone can give limited information about the inelastic processes occurring. We have therefore monitored both axial and transverse extensions in order to determine an instantaneous or differential Poisson's ratio; $-d\epsilon_{\text{trans}}/d\epsilon_{\text{axial}}$. The Eshelby elastic value shown in Fig. 10.4 is the transverse composite C.T.E. divided by the axial composite C.T.E. Any deviation from this value points to the occurrence of inelastic events. Despite the noise of the values, we see a deviation from elastic behaviour during the high temperature part of the cycle, and at the base of the cooling ramp.

10.3.4 150-425°C cycle with no applied load

The generation and relaxation of the internal elastic strains (i.e. with the stress-free thermal changes (α_T) removed) as a function of the cycling temperature can be clearly seen in Figure 10.5. Each of the 16 data points show the mean lattice strain during a cycle segment. Due to an advantageous 111 texture and good whisker alignment, the diffracted intensity in the axial direction is much greater than in the transverse, giving rise to much better statistics in this direction. This, combined with the fact that the expected strain changes in the axial direction are much larger, means that the axial data is much less affected by measurement errors than the transverse. This data shows clearly the very rapid change in internal strain as the temperature is increased from the cold dwell, the matrix becoming less tensile, the whiskers less compressive, due to the large coefficient of expansion of the matrix. It is also clear that the rate of change decreases at high temperature and reverses above about 350°C as the matrix stress becomes much smaller (Fig 10.5). It is also clear that the gradient reaches its maximum (i.e. elastic) value in the middle of the cooling ramp - this is due to yielding at high temperature due to the low yield stress, and at low temperature due to the large misfit stress generated.

10.3.5 175-400°C cycles with an applied load of 25MPa

Fig. 10.6 shows the development of axial and transverse strain in the two phases during the 175-400°C cycle with a 25MPa applied load. The measurement errors tend to be larger for the SiC whiskers principally due to the smaller phase content, i.e. to the lower signal intensity.

In trying to understand the shape of Fig. 10.6 we need to consider a number of effects. It must be remembered that we are trying to interpret a three dimensional stress field using average strain measurements in one direction. For instance this means that a zero axial elastic strain does not necessarily correspond to zero axial stress. Nonetheless, conclusions can be drawn regarding the stress state of the composite. Both phases are strained axially by the imposed load, which if we ignore thermal and plastic effects would produce an axial strain of $275\mu\text{strain}$ in the Al and $160\mu\text{strain}$ in the SiC (elastic FE model). The effects of Poisson restraint evidenced in these results are shown by a comparison to an equal stress (Reuss) assumption which results in $50\mu\epsilon$ in the SiC, $370\mu\epsilon$ in the Al. Secondly, differential thermal expansion leads to elastic misfit strains and hence to a linear decrease in the tensile strain in the Al phase and the compressive strain in the SiC as the temperature is raised and the reverse when it is lowered. Excellent agreement with the FE slopes is achieved. The inelastic relaxation of axial strain is most obvious during the high temperature dwell.

Figure 10.7 shows more clearly the hysteresis in the curves, i.e. the inelastic changes driven by the internal stresses. The solid lines represent Eshelby predictions, i.e. purely elastic changes. There is a clear deviation from the elastic around 275°C in the heating ramp, which continues as the temperature increases further and the systems ability to support elastic strains decreases, curving right back round at the very top of the cycle. The very top of the cooling ramp again shows deviation from elasticity, then there is a region of elastic behaviour, followed by plasticity at the very base of the cooling ramp as the rate of elastic strain generation decreases. This is in good agreement with the evidence for inelastic changes in section 10.3.3.

10.3.6 The effect of Increasing the Temperature Excursion ΔT on Internal Strain

Figure 10.8 shows the strain in the Al with changing excursion ΔT . The lines have been shifted to have the same strain in the cold dwell to make relative changes clearer. Clearly the absolute values of strain during the cold dwell will change as T_{esf} moves to reflect increases in ΔT . It is clear that there is surprisingly little difference between the matrix strains stored for the different cycles. The Eshelby lines are for completely elastically accommodated thermal misfit stresses and thus predict the strain variation over the cycle to increase in proportion to the thermal excursion, i.e. for the gradient of strain change to increase with ΔT in Figure 10.8. While there is some evidence of a larger gradient at the low temperature end of the heating ramp and at the base of the cooling ramp for the largest experimental ΔT cycle it is clear that the overall strain variation is approximately the same for all the ΔT excursions. This is because the yield stress of the matrix limits the generation of thermal misfit strain in the 225 and 200°C cycles to approximately the same as that for the largely elastic 175°C cycle.

10.4 Discussion

In the initial work programme it was planned to set up a stroboscopic measurement system for time resolved studies of thermal cycling with;

- **< 5 secs time resolution** - to date 16 time bins have been used to measure thermal cycles to a resolution of about 30 seconds. There is no reason however why, by counting for 6 times longer, the time resolution should not be 5 seconds.
- **simultaneous monitoring of two phases** - simultaneous monitoring of both phases (Al and SiC) and both axial and transverse to the loading axis has been achieved for Al/SiC composites, both with and without an applied load.
- **development of strobing software** - in collaboration between scientists at the Rutherford Appleton Laboratory and Cambridge University software capable of

storing up to 16 diffraction profiles stroboscopically has been designed and implemented

- **synchronisation of data acquisition & furnace software** - this has been achieved through the use of synchronisation pulses sent by the furnace to the data acquisition system. These pulses shift the data acquisition bin register. Special precautions are taken to ensure continued registry throughout the experiment (section 10.2).
- **design & build in-situ furnace with 5 minute cycle time** - a furnace capable of 0-800°C cycles has been built by the Kiel group allowing super fast heating times (>50°C/min) and cycle times as short as 3 minutes as well as simultaneous external applied loading. Special precautions have been taken to ensure that the furnace does not overheat the focusing collimators (see section 10.2).

This part of the programme has matched our greatest expectations providing the first insights into strain variations within thermal cycles. It has also shown the potential for pulsed source instruments for the measurement of cyclic phenomena generally.

10.5 Conclusions

- The stroboscopic data collection system is an extremely powerful method for the examination of thermal cycling
- Fatigue loading and other rapidly cycling phenomena could also be studied using this technique
- The furnace rig can achieve very rapid (50°/min) heating and cooling rates without damage to the collimator system
- Strain changes in Al and SiC have been made to 50×10^{-6} strain accuracy with a time resolution of 30 seconds for the first time.
- Creep and plasticity are necessary to explain the observed internal strain behaviours during cycling

10.6 Tables/Figures

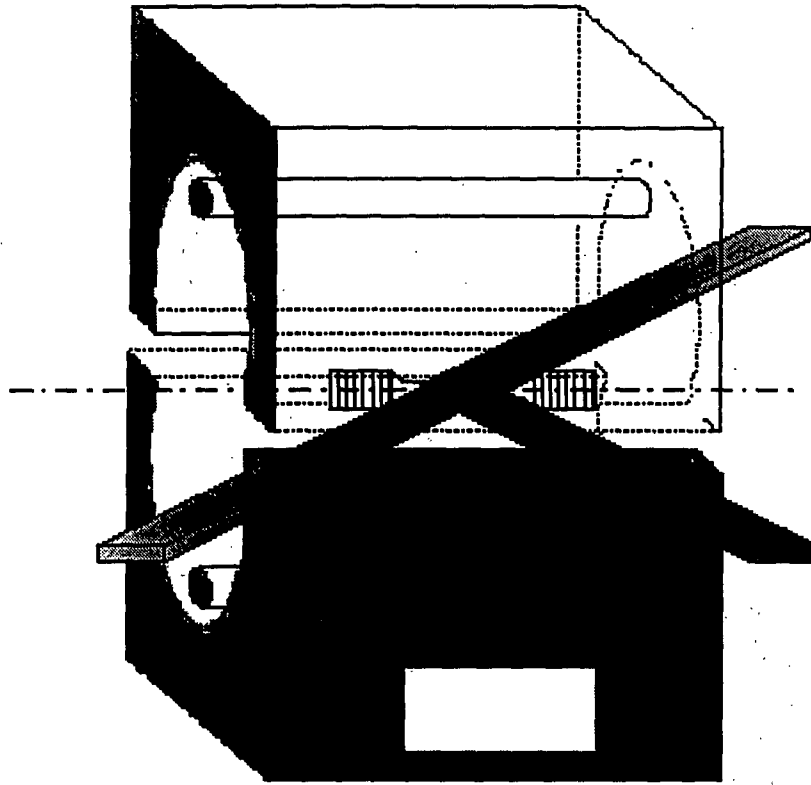


Figure 10.1: A schematic of the rig built at Kiel.

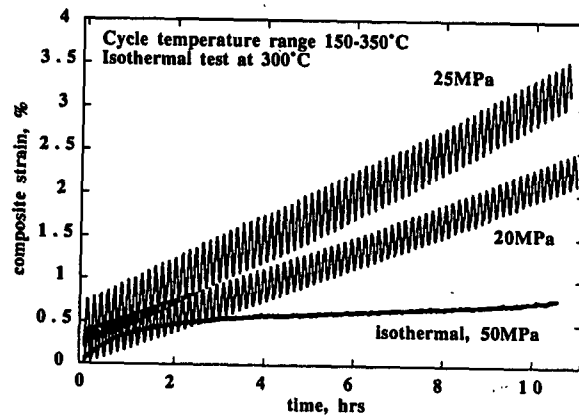


Figure 10.2 A comparison of the relative creep rates for isothermal and thermal cycling creep

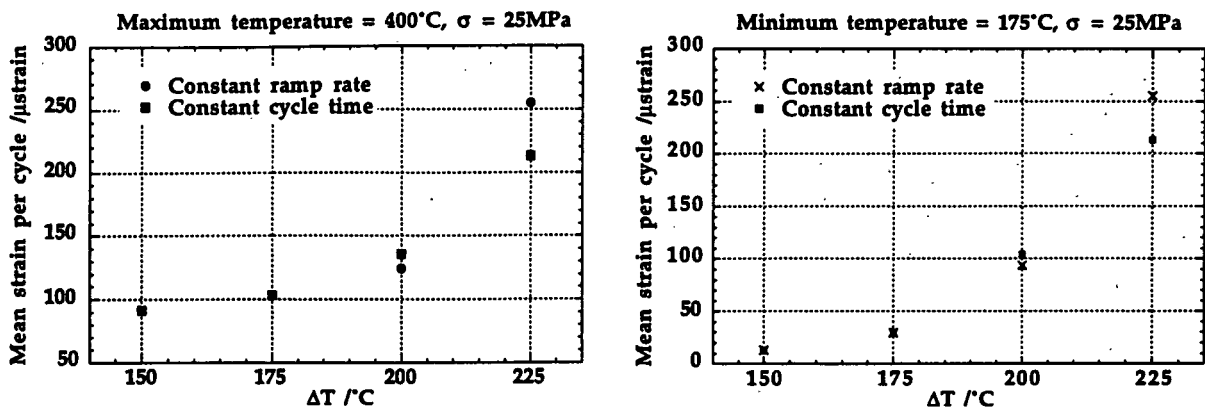


Figure 10.3 The changes in macro-strain per cycle obtained for different temperature excursions (ΔT) with a) the maximum temperature and b) the minimum temperature of the cycle fixed

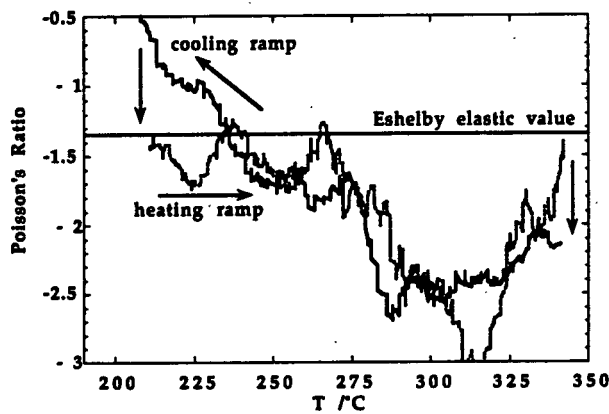


Figure 10.4 Variation of Poisson's ratio during a 200-350°C cycle, under 25MPa load. Here Poisson's ratio represents $-d\epsilon_{trans} / d\epsilon_{axial}$

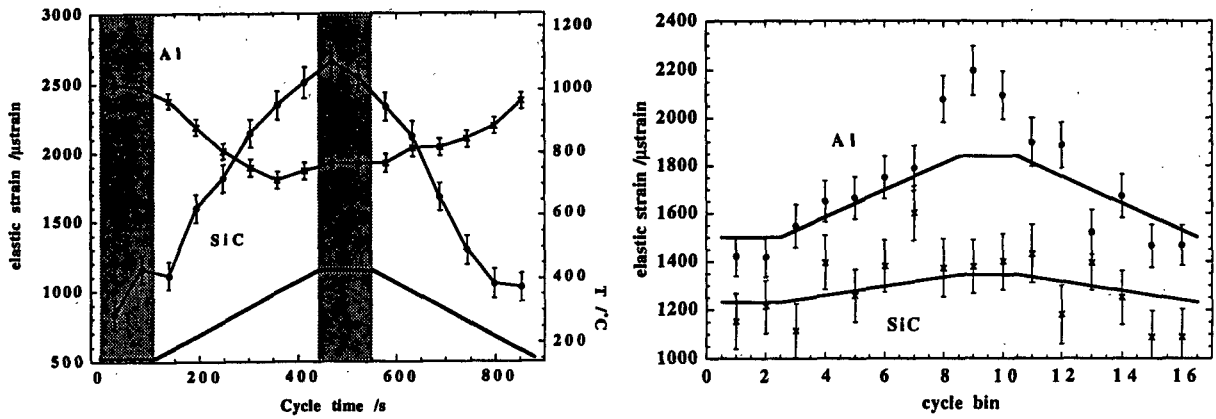


Figure 10.5: The variation of neutron diffraction determined a) axial and b) transverse elastic strains (i.e. $-\alpha\Delta T$) in the two phases of the Al/10% SiC_w composite during the 150-425°C cycles without a superimposed load. The lines in b) show Eshelby predictions.

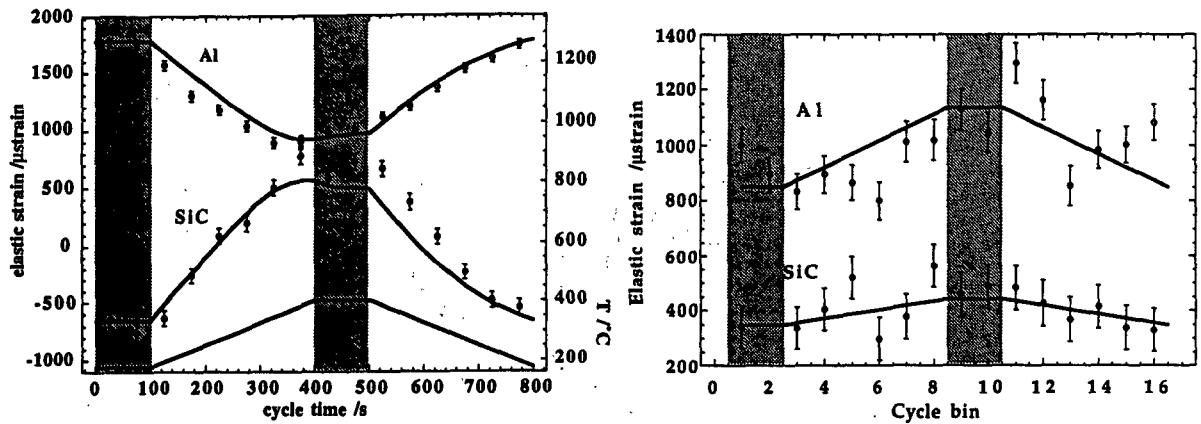


Figure 10.6: The variation of neutron diffraction determined a) axial and b) transverse elastic strains (i.e. $-\alpha\Delta T$) in the two phases of the Al/10% SiC_w composite during the 175-400°C cycles with a superimposed load of 25MPa. In a) the solid lines represent finite element model predictions, in b) Eshelby model values.

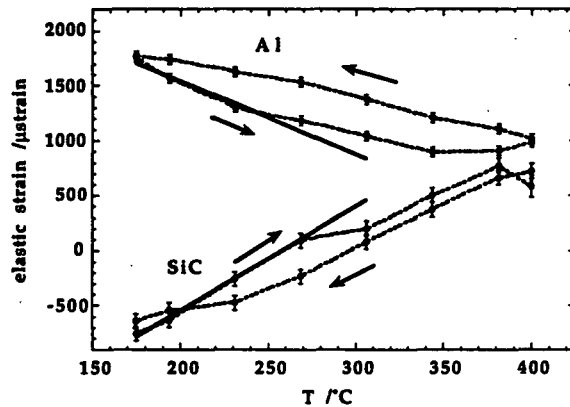


Figure 10.7: A hysteresis plot showing how strains diverge from the elastic at low T on cool and high T on rise, for the 175-400°C cycle, 25MPa applied load. Solid lines represent Eshelby model predictions.

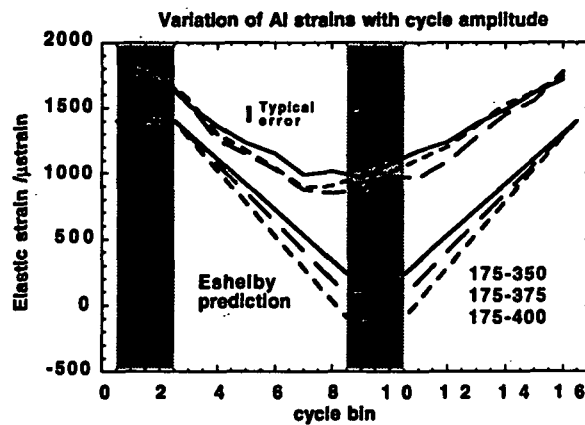


Figure 10.8: Al strains for changing ΔT - the curves have been re-zeroed to have the same strain in the cold dwell.

10.7 References

1. Withers, P.J., et al. *The Evaluation of Internal Stresses in a Short Fibre Metal Matrix Composite by Neutron Diffraction*. in *Proc. ICCM VI/ECCM2*. 1987. London: Elsevier.
2. Withers, P.J., W.M. Stobbs, and O.B. Pedersen, *The Application of the Eshelby Method of Internal Stress Determination for Short Fibre Metal Matrix Composites*. *Acta metall. mater.*, 1989. 37: p. 3061-3084.
3. Wu, M.Y. and O.D. Sherby, *Superplasticity in a Silicon Carbide Whisker Reinforced Aluminium Alloy*. *Scripta Met.*, 1984. 18: p. 773-776.
4. Pickard, S.M. and B. Derby. *Superplasticity During Thermal Cycling of Metal Matrix Composites*. in *Fundamental Relationships Between Microstructures and Mechanical Properties of Metal-Matrix Composites*. 1990. Indianapolis, Indiana: TMS.
5. Daymond, M.R. and P.J. Withers, *An Examination of Tensile/Compressive Loading Asymmetries in Aluminium based MMCs using the Finite Element Method*. *Mat. Sci. Tech.*, 1995. 11(3): p. 228-236.
6. Levy, A., *Finite Element Three-Dimensional Elastic-Plastic Creep Analysis*. *Eng. Struct.*, 1981. 3(January): p. 9-16.
7. Clauer, A.H. and N. Hansen, *High Temperature Strength of Oxide Dispersion Strengthened Aluminium*. *Acta metall. mater.*, 1984. 32(2): p. 269-278.
8. Levy, A. and J.M. Papazian, *Elastoplastic Finite Element Analysis of Short-Fiber-Reinforced SiC/Al Composites: Effects of Thermal Treatment*. *Acta metall. mater.*, 1991. 39(10): p. 2255-2266.
9. Daymond, M.R. and P.J. Withers. *In Situ Monitoring of Thermal Cycled Metal Matrix Composites Using Laser Extensometry and Neutron Diffraction*. in *Int. Conf. on Composite Materials 10*. 1995. Whistler, Canada: Woodhead.
10. Daymond, M.R. and P.J. Withers. *Thermal Cycling of Whisker Reinforced Metal Matrix Composites - A Comparison Between Finite Element Models and Experimental Results*. in *Numerical Predictions of Deformation Processes and the Behaviour of Real Materials*. 1994. Risø, Roskilde, Denmark: Risø National Laboratory.
11. Daymond, M.R. and P.J. Withers, *Stroboscopic Neutron Diffraction Monitoring of Metal Matrix Composites Undergoing Rapid Thermal Cycling*. *Scripta Met.*, 1996. To be published.
12. Daymond, M.R. and P.J. Withers, *Internal Strains in Metal Matrix Composite Undergoing Rapid Thermal Cycling Determined by Neutron Diffraction*. *Acta metall. mater.*, 1996. To be published.

11 Studies of Short Range Stresses in MMC Fatigue Cracks

11.1 Introduction

As stated in the original PREMIS work programme 'Metal Matrix Composites are distinctly inhomogeneous at a microscopic level. It is this inhomogeneity which gives rise to a suite of commercially interesting mechanical properties, through a transfer of load from the matrix to the stiffer reinforcing phase, but it also makes them very difficult to model analytically or numerically. Neutron diffraction is an excellent way of investigating the efficacy of load transfer. However, because the elastic strain in any one crystallite is made up of a macroscopic component (i.e. that which would exist in an homogeneous isotropic continuum) and microscopic components (i.e. the internal stresses between it and those around it) interpretation is difficult.'

As originally planned, we have examined the behaviour of fatigue cracks in Al/20% SiC particulate composites exploiting the penetrating power of the neutron beam to measure the stress field around a crack tip deep within the material. In addition, the interaction between residual stress fields, particle/matrix mismatch stress fields and crack tip stresses has been revealed for the first time. In order to do this we have developed and applied a model for the separation of different types of stress. At the outset our objectives were:

- to measure macro-residual stress fields
- to map-out crack-tip stress fields at maximum and minimum crack opening load
- to measure elastic and thermal mismatch mean phase stresses
- to separate macro and micro residual strains

As some of the above objectives overlapped with an EPSRC funded programme looking at macro/microscale interactions during fatigue growth, some of the objectives were met directly from this programme and the remainder tackled through the latter project. Together, the findings are of general utility and tell one much about the feasibility of using strain scanning for problems such as crack-tips where high spatial resolution is required.

The approach was to use neutron strain scanning to measure the initial state of residual stress in Al/SiC composite plate caused by quenching, and by subsequent annealing. The 1.5mm sampling volume achievable on ENGIN was more than sufficient to characterise the stress field. Good agreement was achieved with similar measurements made in Denmark. A stress separation model was extended to separate microstresses arising from the elastic modulus mismatch between the reinforcement and the matrix, and the thermal mismatch stresses arising from their different coefficients of thermal expansion. The effect of growing fatigue cracks into the residual stress field was then characterised by neutron strain scanning at maximum crack opening and at minimum crack opening (i.e. fully loaded and fully unloaded crack).

11.2 Residual stress Fields

High values of residual stress, such as that caused by a quench, can slow the growth rate of long fatigue cracks.[1] It has been proposed that the high compressive surface residual stresses (measured as about 380 MPa.[1]) retard the crack growth in the near-surface regions, whereas the tensile stresses in the centre of the material accelerate crack growth causing crack bowing. It has been proposed that this might arise as a result of changes in

crack closure with residual stress causing a lowering of the effective stress intensity *range* experienced by the crack tip as a function of position in the stress field.

The magnitude of such quench residual stress fields have been measured; these results are important if the interaction between residual stresses and crack tip stresses is to be understood.

11.2.1 Experimental Details

The material studied for this work is a powder-metallurgy 2124-Al MMC reinforced with 20wt% ($\approx 17\text{vol}\%$) nominally $3\mu\text{m}$ particulate SiC. Two ageing conditions were adopted:

- As quenched (NA): solution treated at 505°C , cold water quenched and aged at room temperature for >100 hrs
Overaged (OA): solution treated, cold water quenched and aged at 190°C for 48 hrs.

11.2.2 Results

Quenched Plates

The stress field in the quenched plates were measured by neutron diffraction. Results are presented in figure 11.1a for two quenched plates of the composite material. Both were quenched as per above. One plate (plate 1 - A712A/4) was heat treated at Cambridge, the other (plate 2 - 681/3), at AEA, Harwell. The neutron diffraction measurements on plate 1 were performed on ENGIN, while plate 2 was examined at the DR3 reactor at the Risø National Laboratory, Denmark. Measurements were made of the in-plane (y or x) and through-thickness (z) strains, as a function of position along the z-axis.

Overaged Material

The effect of the overageing heat treatment on the stress levels in the composite is shown in figure 11.1b. It is clear that a large reduction ($>50\%$) in elastic strain (stress) is achieved by the overageing heat treatment.

Note how the in-plane and through-thickness strain variations combine to give approximately no stress variation in the through-thickness direction. This indicates that the observed strains in the z-direction arise solely from Poisson's ratio effects. The consistency in the results is particularly noteworthy, as comparable results have been obtained from two separate composite plates, using two different neutron spectrometers, one on a constant flux source and the other on a pulsed source.

11.3 Crack Tip Stress Fields

11.3.1 Experimental Procedures

Cracks have been grown in single edge notched bend (SENB) specimen bars quenched and treated as plate with the crack growth direction running from surface to surface of the original plate (Figure 11.2).

This has the advantage that straight cracks can be grown, because the residual stress experienced by the crack is the same all along its width. The magnitude of the residual stress experienced by the crack changes as a function of its length (a), i.e. of its position in the field.

Three samples were examined as part of this study, one reinforced, two unreinforced. The samples were fatigue cracked, and examined both unloaded, and loaded to the maximum load that the specimen would have experienced during growth of the final portion of the fatigue crack. One of the unreinforced samples was tested in the quenched state, the other in the overaged state. The specimens were loaded using a specially-designed bending rig which allows strain scanning to be performed while the specimens are loaded *in situ* on the diffractometer. The gauge volume, the region of intersection of the incident and scattered beams, over which the diffraction measurements were averaged, was defined by apertures 0.5 mm wide and 8 mm high placed in the incident and scattered beams.

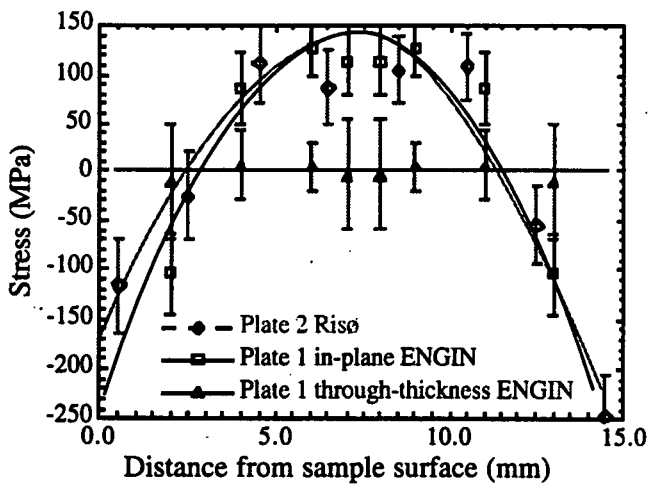


Figure 11.1a: Stress in the matrix of plate 1 in y (in-plane) and z (through-thickness) directions, as a function of depth (z), deduced from the measured strains. Independent measurements on plate 2 made at Risø show excellent agreement with our results.

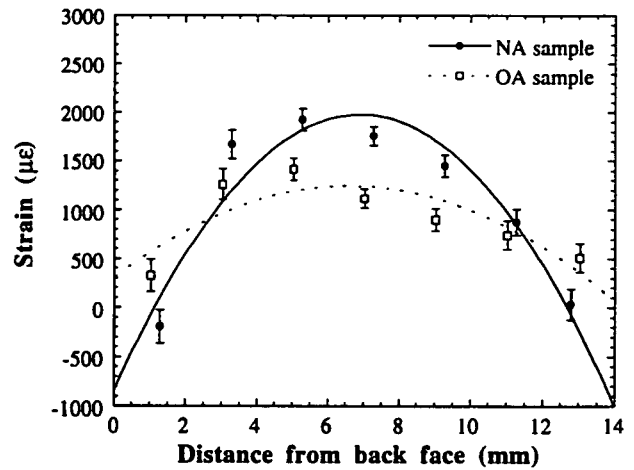


Figure 11.1b: Measured in-plane (ϵ_y) strain variations with depth (z) in the matrix of naturally-aged and overaged samples of the composite material.

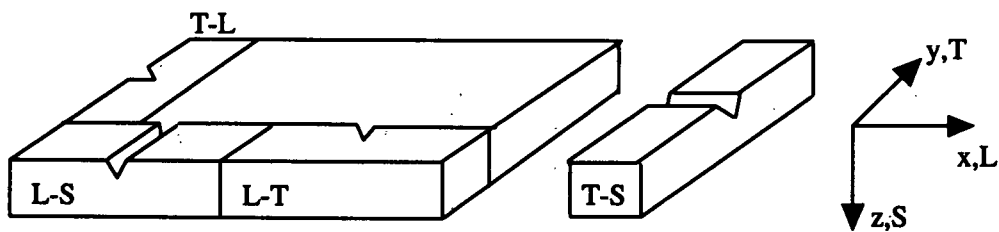


Figure 11.2: Specimen orientations and axes relative to the rolled plate.

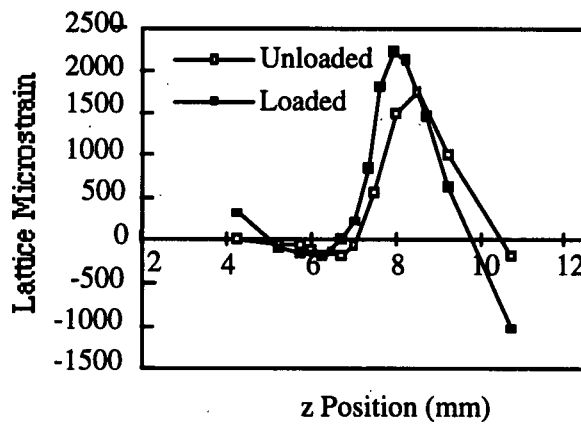


Figure 11.3. Elastic strain along the crack line in the crack opening direction in the NA alloy bar.

11.3.2 Results

Quenched Al Alloy bar

The elastic strains in the crack opening direction were measured along the crack plane for the same specimen, both for the loaded and unloaded cases (Figure 11.3). At $K_{max,app}$, the elastic strain ϵ_y peaks just in front of the crack tip (crack front position=7.54 mm - observed when the specimen was subsequently broken). The large tensile peak in the unloaded bar was unexpected and shows that the crack is held open even for $K_{min,app} = 0$, and is direct evidence that crack closure is taking place.

Over aged Al/20% SiC bar

That closure is acting to keep open the crack faces at minimum load is corroborated by the results on the composite material. In Figures 11.4(a) and 4(b), the elastic strain components ϵ_y in the matrix and the reinforcement for the overaged composite bar are shown, and the same pattern is clearly visible between the loaded (solid symbols) and the unloaded (open symbols). Several other important features should be noted. Firstly, the effect of the thermal mismatch stresses is clearly seen. In Figure 11.4(a) the far field matrix strains are tensile (dashed line), while those in the particles are compressive, elevating or depressing the parabolae respectively. The mismatch term is equivalent to a temperature drop of around 230°C [3]. As a result, over the 0.5 mm sampling length, the average elastic strains in the particles are compressive everywhere, even near the crack tip.

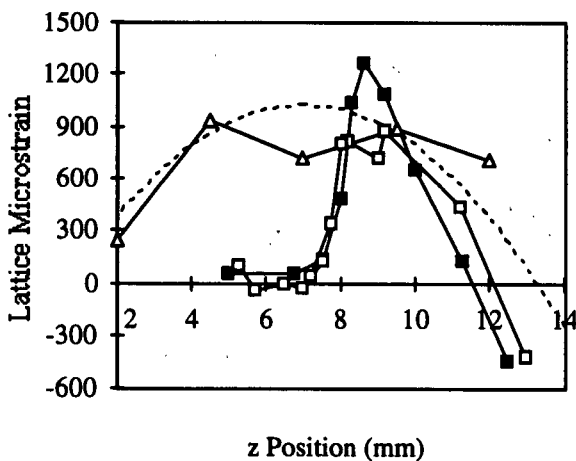


Figure 11.4(a). Lattice strain (ϵ_y) on the crack plane in the Al matrix.

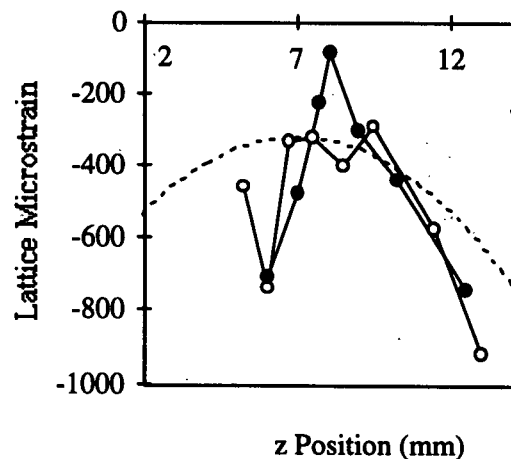


Figure 11.4(b). Lattice strain (ϵ_y) on the crack plane in SiC.

11.3.3 Theoretical Models

FE and analytical modelling of the fatigue crack growth through the quench residual stress field also point strongly towards the occurrence of crack closure as shown in figure 11.5.

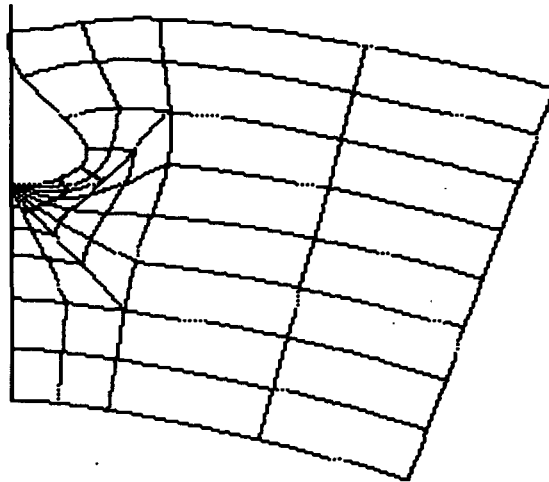


Figure 11.5. A coarse FE mesh, showing how the quench residual stress causes crack contact in the vicinity of the crack mouth (carried out as part of an EPSRC project).

Using the dislocation density model, Figure 11.6(a) shows the stress variation along the line of the crack (solid line). The crack opening profile (long dash) shows closure to occur approx. 3mm from the crack tip. Note, in common with the measurements, the tensile peak associated with the stress intensification near the tip. The compressive stress occurring due to crack mouth contact is outside the range of the current neutron measurements.

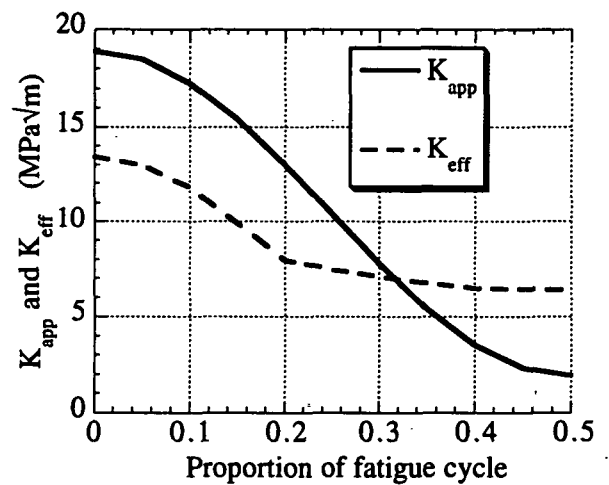
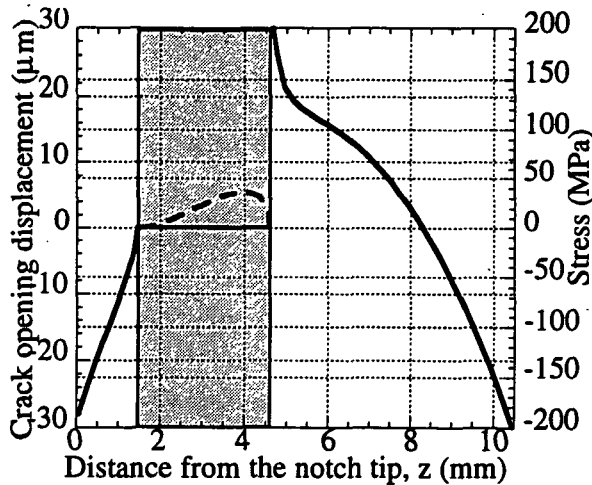


Figure 11.6(a). Stress distribution on the crack plane in a fully unloaded sample (from EPSRC project)

Figure 11.6(b). Variation of K_{app} and K_{eff} during the unloading half of the fatigue cycle (from EPSRC project).

In Figure 11.6(b) a comparison is made between the variation of the applied stress intensity factor, deduced from the specimen configuration and loading disregarding the presence of the residual stresses, and the *effective* stress intensity factor, calculated assuming that discontinuous crack closure is taking place. At a certain time during the cycle, when K_{app} reaches a critical value ($K_{app}^* \approx 8 \text{ MPa}/\text{m}$ in this case), the first contact of crack faces takes place. Following this event, the crack closure keeps the rest of the crack propped open. As a result further variation of K_{eff} is very slight and ΔK_{eff} is greatly reduced.

11.3.4 Conclusions

These are the first measurements of crack tip stress fields in composite materials and they strongly indicate that crack closure is occurring. The theoretical approaches suggest that the presence of quench-induced residual stresses is likely to result in discontinuous crack closure, with the first instance of crack face contact being well removed from the crack tip. Of course the measured profiles shown here are smeared out both by the effect of the finite size of the sampling volume, and by any curvature of the crack front. However, it is clear from the steepness of the rise in stress at the crack tip that the latter effect is small.

11.4 Separation of the Various Stress Fields

As composites are, by their very nature, physically inhomogeneous, stresses are almost never uniformly distributed throughout their structure. Applied loads tend to be distributed such that a higher stress will be present in the reinforcement; both because of the **stiffness mismatch**, and because in certain cases the matrix may deform plastically whereas the reinforcement may undergo only elastic deformation. In addition, changes in temperature will lead to the development of **thermal mismatch stresses**.

In view of the different stress fields which can arise in a composite, it is important to be able to separate them. We have developed a means of doing this. Both macrostresses (σ^{Macro}) and mean phase microstresses ($\langle \sigma \rangle_M$ and $\langle \sigma \rangle_P$) can cause the shifting of a diffraction peak, but provided the strains are known in both phases it is possible to separate them[2]. This is because the microstresses, $\langle \sigma \rangle_M$ and $\langle \sigma \rangle_P$, must average to zero over the sampling volume while the macrostress, σ^{Macro} , must be the same in both phases. The macrostress may thus be readily determined from the stress in each phase, which is calculated from the measured strains in each phase.

Once the macrostress-related contributions have been calculated in each phase, the thermal mismatch stresses can be calculated simply by subtracting the macrostress terms from the overall phase stress, provided that there are no other stress misfit terms. These stresses arise because of the difference in coefficients of thermal expansion (CTE) of each phase. On cooling from the fabrication temperature, or in this case the heat-treatment temperature, the material will experience a temperature drop of ΔT which will generate a misfit strain of $\Delta \alpha \Delta T$ between the phases.

Crack tip stresses

The power of the stress separation technique is well illustrated in the analysis of our fatigue crack results.[3]. The phase stresses arising solely from the macrostress are shown in Fig. 11.7. The macrostress field (which lies between the individual phase curves) comprises the original quench residual stress field and that arising from the fatigue crack. Because of the reinforcing effect of the stiffer SiC phase, the phase stress arising in the reinforcement from the macrostress is at all points larger than that in the matrix. With the crack held fully open,

the tensile stresses at the crack tip are increased, while those at the back face are more compressive, as expected.

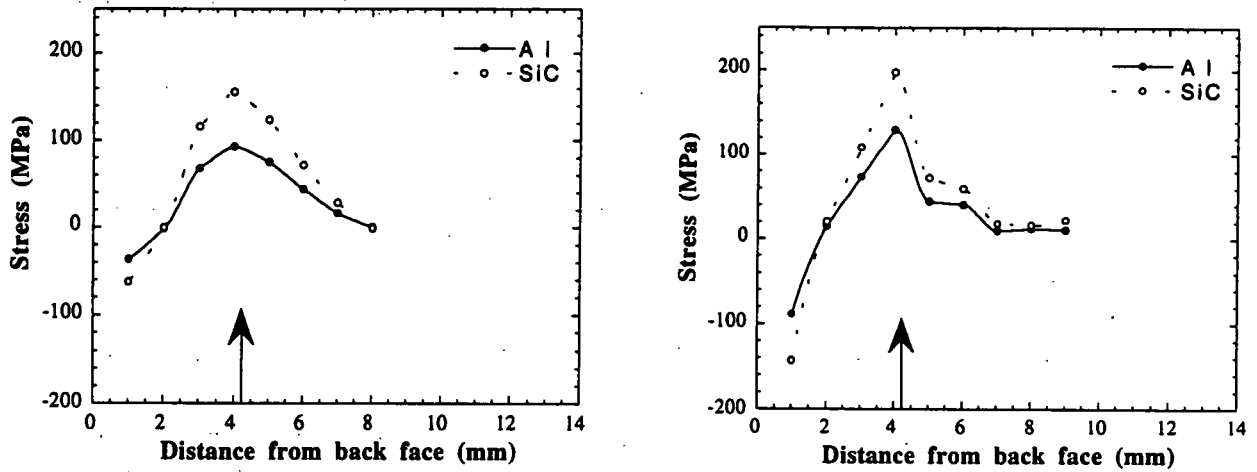


Figure. 11.7: The separated phase stresses arising from the macrostress field, a) with no load applied and b) with the crack held at maximum opening load[3].

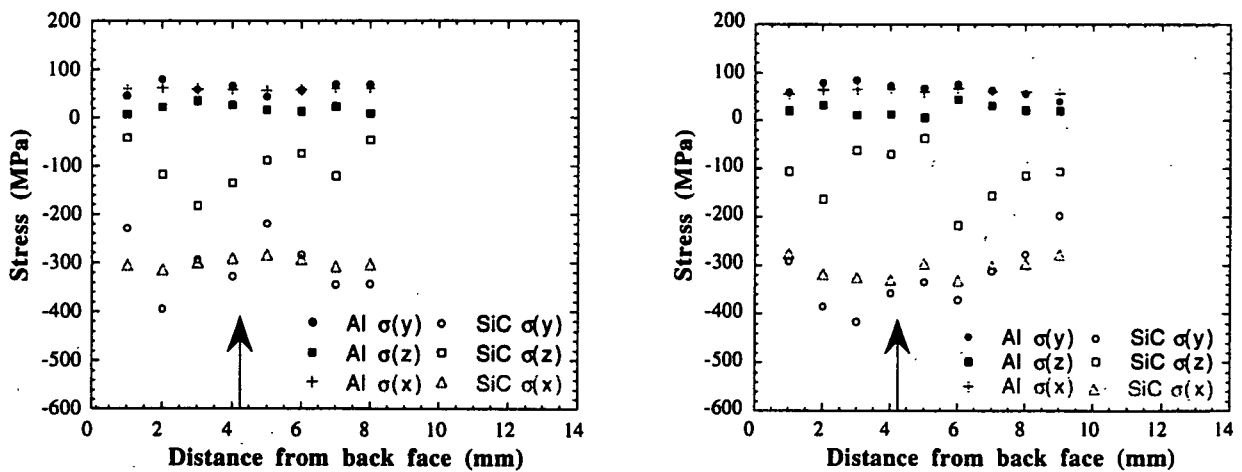


Figure. 11.8: The separated inelastic mismatch phase stresses in the fatigued composite, a) with no load applied and b) with the crack held fully open[3].

Finally, the stress free shape misfit stresses are shown in Fig. 11.8. These are quite large and are compressive in the reinforcement and tensile in the matrix. Although the scatter is fairly large, these stresses would appear to be largely hydrostatic, and insensitive both to the position along the crack path and to the application of load. One might therefore reasonably assume they are the thermal residual mismatch microstresses. If interpreted in this light, they correspond to a stress free temperature of around 200°C, which is close to that observed elsewhere in this report. It is perhaps surprising that the thermal residual stresses seem to be retained in spite of the passage of the crack tip, and that the total stress in the 'reinforcing' particles is in fact negative everywhere, even in the immediate vicinity of the crack tip. However, it is important to bear in mind the fact that the size of the plastic zone is very small - about a tenth of the sampling volume. Here a sampling cross section of 1mm² was used as against 0.25mm² for the distributions of Fig 11.3; this explains the greater smearing seen here. In summary, this example illustrates the usefulness of being able to strip away both the macrostress and the related elastic mismatch microstress to reveal the variation in the shape misfit stresses (in this case, the thermal residual stresses).

11.5 Discussion

The technical requirements for this part of the work programme (6.4.1) were envisaged to be:

- **1x2x2mm sampling volume** - a sampling volume of 0.5x0.5x8mm was used to achieve very high resolution for the crack tip fields while 1.5x1x10mm was used for to determine the original quench residual stress fields
- **<0.25mm spatial resolution after deconvolution** - it was found that 0.5mm resolution prior to deconvolution was sufficient for the crack tip measurements
- **0.1mm sample translation** - this was well within the capability of the spectrometer, however because of the 0.5mm sampling volumes used, scan increments of 0.5mm were used.
- **effective deconvolution procedures** - because of the increased spatial resolution achieved, it was not necessary to design new deconvolution methods, however it is still regarded that this should be done in the near future as there are many engineering applications which would benefit from the analysis
- **macro/micro separation** - effective procedures for the separation of the macro and micro components of the stress field have been developed and published

11.6 Conclusions

- Crack tip stress field have been measured for the first time in composite materials
- Residual stresses have been found to have a very important effect of fatigue crack growth through residual stress induced closure.
- The various stress components have been identified and measured

The project was very successfully carried out, aided through the interaction with an EPSRC funded programme. Direct comparisons were made with residual stress measurements made on a continuous source in Denmark and a remarkable good agreement was found[3]. As planned, stress fields around fatigue cracks in Al/SiCp material was mapped both at maximum and minimum opening load. It was not easy to resolve the plastic crack tip zone, but the elastic field and its interaction with the prior residual stress field was very interesting. The results were surprising in terms of the extent to which closure mechanisms were successful in keeping the crack open (i.e. the stress field tensile) even when the applied crack opening load was removed. This finding has very important implications for fatigue crack growth predictions when residual stress fields are present. Finite element calculations are able to predict similar stress field only if the residual stresses cause the crack to close near the mouth of the crack and have confirmed that such residual stresses can reduce the stress intensity range (i.e. shield the crack) experienced at the crack tip by up to 60%.

11.7 References

1. D.M. Knowles and J.E. King, *Influence of Macroscopic Residual Stress Fields on Fatigue Crack Growth Measurement in SiC Particulate reinforced 8090 Alloy*. Mat. Sci. & Tech., 7: 1015, (1991).

2. I.C. Noyan and J.B. Cohen, *Residual Stress - Measurement by Diffraction and Interpretation*. Materials Research and Engineering, ed. B. Ilshner and N.J. Grant. New York: Springer-Verlag. 272, (1987).
3. M.E. Fitzpatrick, M.T. Hutchings, J.E. King, D.M. Knowles and P.J. Withers. *The Effect of Thermal residual Stress Fields on Crack Growth in Al/SiC_p Metal Matrix Composites*. in IXth Int Conf. Composite Materials. Madrid: In Press, (1993).
- 7 M. E. Fitzpatrick , M. T. Hutchings, C. G. Windsor, & P. J. Withers, Separation of Macroscopic, Elastic Mismatch and Thermal Expansion Mismatch Stresses in Particle-Reinforced Metal Matrix Composite Quenched Plates from Neutron Diffraction Measurements, Submitted to Acta Met. et Mat., (1995).

12 Extracting the Strain Tensor

12.1 Introduction

When a force is applied to a material, the material is said to be in stressed condition. Stress is defined as the amount of applied force per unit area. In general a material may be subject to two kinds of stress.

- Applied stress, which is the result of using the construction for what it has been designed.
- Residual stress, which is the result of fabrication processes (rolling, welding, forging) and/or wear processes during use.

Stress is a quantity that cannot be measured directly, but there are several techniques which enable it to be measured from its effects on the material. The stress measurement employed in the PREMIS project - neutron diffraction - uses the crystallographic lattice spacing as an internal strain gauge.

To determine the stress state from measured strain data, we need a relationship between stress and strain. Only then the engineering quantity stress can be calculated from the physical quantity strain. Strains cannot be measured by means of neutron diffraction but we can measure lattice distances. Distances can be determined as a single value related to all the planes aligned according to the present orientation of planes with reference to the scattering vector ("multiple-peak analysis) or they can be related to a single lattice plane (single-peak analysis). To perform stress measurements by means of neutron diffraction, a relationship between the lattice plane distance and the strain has to be established. The strain in an arbitrary direction of a point in space can be expressed in the elements of a tensor that is defined in an arbitrary co-ordinate. The strain tensor in any other co-ordinate system can be derived from the present one by an adequate co-ordinate system transformation. The relationship to be established contains the six elements of the strain tensor and the stress free lattice parameters which all are, in principle, unknown quantities. The solution of all seven unknowns from a set of seven or more of these equations is impossible, unless some other information about the stress state is known in terms of "constraint equations". As constraint equations we chose to fix the stress free lattice parameters to reach a system of six unknowns which is demonstrated to be solvable from a number of six or more observations by means of neutron diffraction.

12.2 Definitions

To introduce the strain tensor, first the specimen co-ordinate system $0x'y'z'$ has to be defined. With respect to this co-ordinate system the second order strain tensor ϵ is defined. The diagonal elements of this tensor represent the strain in the axis direction; the off-diagonal elements represent the shear in planes containing two of the axes of the system. The strain tensor fully describes the strain state of a small volume element in a material with the following shape:

$$\epsilon = \begin{bmatrix} \epsilon_{11} & \epsilon_{12} & \epsilon_{13} \\ \epsilon_{21} & \epsilon_{22} & \epsilon_{23} \\ \epsilon_{31} & \epsilon_{32} & \epsilon_{33} \end{bmatrix}$$

being

$$\epsilon_{21} = \epsilon_{12}$$

$$\epsilon_{31} = \epsilon_{13}$$

$$\epsilon_{32} = \epsilon_{23}$$

The diagonalization of the matrix ϵ automatically yields to the principal tensor of the strain. This corresponds to a co-ordinate transformation to the so called principal co-ordinate system, which is the unique system in which the shear stresses vanish, leading to null off-diagonal elements:

$$\epsilon_p = \begin{bmatrix} \epsilon_{11} & 0 & 0 \\ 0 & \epsilon_{22} & 0 \\ 0 & 0 & \epsilon_{33} \end{bmatrix}$$

The transformation of a strain tensor on the principal co-ordinate system is always possible because the strain tensor is symmetric. The matrix that describes the tensor has three independent eigenvectors, associated to each eigenvalue, which are mutually perpendicular.

The strain tensor relative to the co-ordinate system $0x'y'z'$ fixed in the sample may be determined from a number of experiments by measuring the strain e in different directions. Different directions are obtained by choosing different sample orientations with respect to the scattering vector q . For each strain measurement, the direction of e is defined by the direction cosines $(k_i l_i m_i)$:

$$e(k_i l_i m_i) = k_i^2 \epsilon_{11} + l_i^2 \epsilon_{22} + m_i^2 \epsilon_{33} \\ + 2k_i l_i \epsilon_{12} + 2k_i m_i \epsilon_{13} + 2l_i m_i \epsilon_{23}$$

The left hand member can be written as

$$e(k_i l_i m_i) = \frac{d(k_i l_i m_i) - d_0}{d_0}$$

where $d(k_i l_i m_i)$ is the lattice spacing for lattice planes oriented according to k , d_0 is the lattice spacing when no stress is present. In previous equation numerator is typically 10^3 smaller than the denominator. Therefore d_0 in the denominator can without noticeable error be replaced by $\langle d(k_i l_i m_i) \rangle$, the average value of the d -values that have been measured:

$$\frac{d(k_i l_i m_i) - d_0}{d_0} \approx \frac{d(k_i l_i m_i) - d_0}{\langle d(k_i l_i m_i) \rangle}$$

We write, for convenience, $\langle d(k_i l_i m_i) \rangle = d$ to obtain the new equation:

$$\frac{d(k_i l_i m_i)}{d} = d_0 / d + k_i^2 \epsilon_{11} + l_i^2 \epsilon_{22} + m_i^2 \epsilon_{33} + 2k_i l_i \epsilon_{12} + 2k_i m_i \epsilon_{13} + 2l_i m_i \epsilon_{23}$$

For n diffraction peaks we obtain n equations of this type. Together they form a system of equations of the form:

$$\frac{1}{d} \begin{pmatrix} d(K_1 l_1 m_1) \\ d(K_2 l_2 m_2) \\ d(K_3 l_3 m_3) \\ \vdots \\ d(K_n l_n m_n) \end{pmatrix} = \begin{pmatrix} 1 & k_1^2 & l_1^2 & m_1^2 & k_1 l_1 & k_1 m_1 & l_1 m_1 \\ 1 & k_2^2 & l_2^2 & m_2^2 & k_2 l_2 & k_2 m_2 & l_2 m_2 \\ 1 & k_3^2 & l_3^2 & m_3^2 & k_3 l_3 & k_3 m_3 & l_3 m_3 \\ \vdots & \vdots & \vdots & \vdots & \vdots & \vdots & \vdots \\ 1 & k_n^2 & l_n^2 & m_n^2 & k_n l_n & k_n m_n & l_n m_n \end{pmatrix} \begin{pmatrix} d_0 / d \\ \epsilon_{11} \\ \epsilon_{22} \\ \epsilon_{33} \\ 2\epsilon_{12} \\ 2\epsilon_{13} \\ 2\epsilon_{23} \end{pmatrix}$$

Its solution should give us the elements of the strain tensor and the stress free lattice parameters. Unfortunately it can be demonstrated that it is impossible to solve the system when d_0/d , ϵ_{11} , ϵ_{22} and ϵ_{33} are unknown at the same time. Thus it can be stated that d_0 should be known a priori.

In order to apply such theory we followed two steps:

- we assumed a simulated scattering vector moving with reference to the reference instrument frame and we developed strain tensor formulas according to its movements in terms of angles as in fig.1
- we developed formulas to simulate the movement of scattering vector (two vectors for what concerns TEST instrument) from sample rotations.

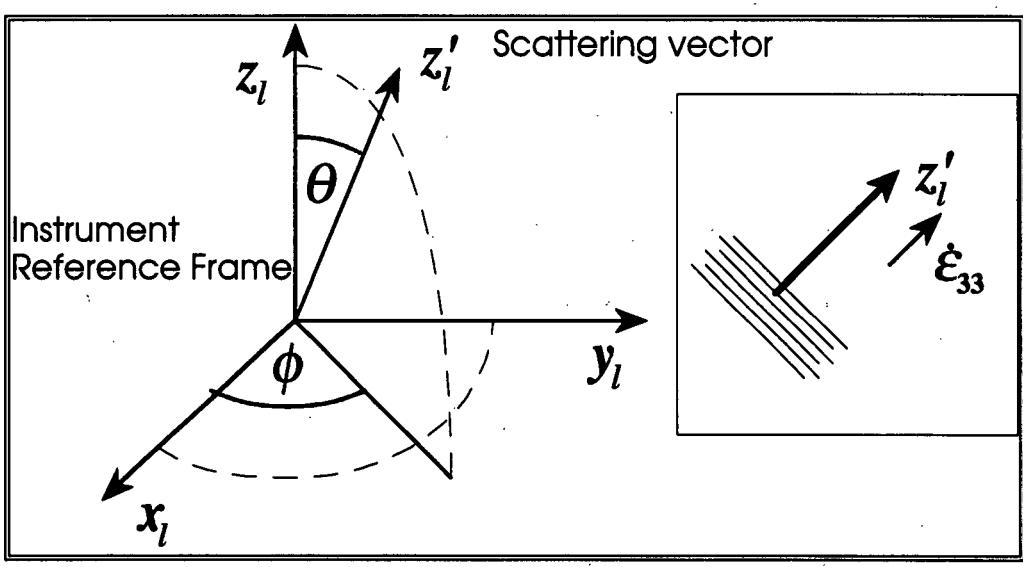


Fig.1

From this point of view we should take into account both the instrument reference frame and a new co-ordinate frame related to the sample itself. Being $Oxyz$ the sample reference frame and $Ox'y'z'$ the laboratory reference frame, the relations between the two frames can be expressed in terms of direction cosines as

	x	y	z
x'	$\cos(x'x)$	$\cos(x'y)$	$\cos(x'z)$
y'	$\cos(y'x)$	$\cos(y'y)$	$\cos(y'z)$
z'	$\cos(z'x)$	$\cos(z'y)$	$\cos(z'z)$

or

	x	y	z
x'	a_{11}	a_{12}	a_{13}
y'	a_{21}	a_{22}	a_{23}
z'	a_{31}	a_{32}	a_{33}

In general the transformation from $Oxyz$ to $Ox'y'z'$ is performed as

$$\begin{aligned} \epsilon'_{ij} = & a_{i1}a_{j1}\epsilon_{11} + a_{i1}a_{j2}\epsilon_{12} + a_{i1}a_{j3}\epsilon_{13} \\ & + a_{i2}a_{j1}\epsilon_{21} + a_{i2}a_{j2}\epsilon_{22} + a_{i2}a_{j3}\epsilon_{23} \\ & + a_{i3}a_{j1}\epsilon_{31} + a_{i3}a_{j2}\epsilon_{32} + a_{i3}a_{j3}\epsilon_{33} \end{aligned}$$

or

$$\epsilon^{xyz} = \begin{bmatrix} a_{11} & a_{12} & a_{13} \\ a_{21} & a_{22} & a_{23} \\ a_{31} & a_{32} & a_{33} \end{bmatrix} \cdot \epsilon'^{xyz}$$

According to the previous theory, for any point inside the sample and for each sample orientation we can introduce a function as

$$\forall x, y, z \quad \epsilon'_{ij}{}^{xyz} = f(\theta, \phi, d_{\theta, \phi}, d_0) = f(\theta, \phi, \text{tof}_{\theta, \phi}, \text{tof}_0)$$

whose actual form is of the kind

$$\epsilon'_{ij}{}^{xyz} = \frac{d_{\theta, \phi} - d_0}{d_0}$$

With regard to the example depicted as in fig.1 we have:

$$(\epsilon'_{33})_{\phi\theta} = a_{3k} a_{3l} \epsilon_{kl}$$

while the matrix of direction cosines becomes:

$$a_{ik} = \begin{vmatrix} \cos \phi \cos \theta & \sin \phi \sin \theta & -\sin \theta \\ -\sin \phi & \cos \phi & 0 \\ \cos \phi \sin \theta & \sin \phi \cos \theta & \cos \theta \end{vmatrix}$$

Thus we can write an equation as:

$$\begin{aligned} \frac{d_{\theta, \phi} - d_0}{d_0} &= \epsilon_{11} \cdot \cos^2 \phi \cdot \sin^2 \theta + \epsilon_{12} \cdot \sin 2\phi \cdot \sin^2 \theta + \\ &+ \epsilon_{22} \cdot \sin^2 \phi \cdot \sin^2 \theta + \epsilon_{33} \cdot \cos^2 \theta + \\ &+ \epsilon_{13} \cdot \cos \phi \cdot \sin 2\theta + \epsilon_{23} \cdot \sin \phi \cdot \sin 2\theta \end{aligned}$$

If we consider all the observations performed over a single point inside the sample and we take into account each one of the observed planes we obtain a system of equations like:

$$\begin{bmatrix} a_{11}^{11} & a_{12}^{11} & a_{13}^{11} & a_{14}^{11} & a_{15}^{11} & a_{16}^{11} \\ a_{21}^{12} & a_{22}^{12} & a_{23}^{12} & a_{24}^{12} & a_{25}^{12} & a_{26}^{12} \\ \dots & \dots & \dots & \dots & \dots & \dots \\ a_{np,1}^{1,np} & a_{np,2}^{1,np} & a_{np,3}^{1,np} & a_{np,4}^{1,np} & a_{np,5}^{1,np} & a_{np,6}^{1,np} \\ \dots & \dots & \dots & \dots & \dots & \dots \\ \dots & \dots & \dots & \dots & \dots & \dots \\ a_{np-nf,1}^{nf,np} & a_{np-nf,2}^{nf,np} & a_{np-nf,3}^{nf,np} & a_{np-nf,4}^{nf,np} & a_{np-nf,5}^{nf,np} & a_{np-nf,6}^{nf,np} \end{bmatrix} \cdot \begin{bmatrix} \epsilon_{11} \\ \epsilon_{22} \\ \epsilon_{33} \\ \epsilon_{12} \\ \epsilon_{23} \\ \epsilon_{13} \end{bmatrix} = \begin{bmatrix} b_1^{11} \\ b_2^{12} \\ \dots \\ b_{np}^{1,np} \\ \dots \\ b_{np-nf}^{nf,np} \end{bmatrix}$$

where: np = number of planes, nf = number of experiments (observations)

As a first remark it must be pointed out that the number of planes can vary for each observation. Thus the term $np \times nf$ only shows that each one of the planes observed is taken into account.

A second remark regards the refinement of data from neutron diffractometer. All we stated is related to a single-peak refinement while for a multiple-peak refinement, data regarding all the planes related to an experiment are gathered to achieve a single information about lattice spacing. In this case the system becomes

$$\begin{bmatrix} a_{11}^1 & a_{12}^1 & a_{13}^1 & a_{14}^1 & a_{15}^1 & a_{16}^1 \\ a_{21}^1 & a_{22}^1 & a_{23}^1 & a_{24}^1 & a_{25}^1 & a_{26}^1 \\ \dots & \dots & \dots & \dots & \dots & \dots \\ a_{nf,1}^{nf} & a_{nf,2}^{nf} & a_{nf,3}^{nf} & a_{nf,4}^{nf} & a_{nf,5}^{nf} & a_{nf,6}^{nf} \end{bmatrix} \cdot \begin{bmatrix} \varepsilon_{11} \\ \varepsilon_{22} \\ \varepsilon_{33} \\ \varepsilon_{12} \\ \varepsilon_{23} \\ \varepsilon_{13} \end{bmatrix} = \begin{bmatrix} b_1^{nf} \\ b_2^{nf} \\ \dots \\ b_{nf}^{nf} \end{bmatrix}$$

In both cases the system has to be solved by means of a least square method. We adopted and implemented a Gauss method.

For what concerns d_0 several experiments were performed in order to evaluate the most convenient a priori value to be used. The simplest rule, i.e. to assume as d_0 the average of the d values calculated for all the observations, led to quite good results. A good proposal seems that of performing a set of experiments in which all the sample volume should be concurrently tested over various orientations. This can be achieved bathing all the sample during an experiment and letting it rotate. On TEST instrument the collimator could be opened in order to make the beam to irradiate all the sample height. Then the sample could be rotated continuously or step by step to cover all possible orientations. This method seems to give good results and is probably the best choice.

12.3 Software Implementation

New programs take control over the great number of routines and data files involved in a typical complete data evaluation chain. All these files were originally conceived at RAL to work interactively; we modified them in order to pass information such as input data and file names as parameters. An almost complete list of these routines and related notes follows.

RAW2ASC

This is an executable file originally written in FORTRAN which extracts from raw files data and stores them into a new ASCII file. This routine is used to access both the raw data, in

order to test their integrity, and the file header in order to extract related information. At present the header files do not contain any information about the sample position and orientation (please see next chapter). Since we think that these information should be stored somewhere as soon as possible, we suggest to automatically store them into raw file header. RAW2ASC original file was modified to automatically pass information to the monitor and is now stored as "RAW2DAT".

ENGINFOC - ENGINFOCL - ENGINFOCRT

These are command files which perform focusing and normalisation to the background and to vanadium. They originally worked inside Genie program and asked for some typical Genie information (e.g. instrument, workspace, run number etc.). We modified them to achieve an automatic exchange of parameters and they have been renamed: PREMFOC PREMFOCL PREMFOCRT.

The focusing and normalisation of raw data are greatly influenced by the choice of two files which contain the information for background and vanadium corrections. Thus, it is very important to update these data files and PREMFOC routines whenever a new set-up of the instrument is performed. A different kind of focusing can be performed over a single .raw file or a group of files.

PROLSFILE

This FORTRAN file moves data from Genie workspaces to an ASCII data file. The new automatic version was stored as "ASCIIDAT".

REFINT

This is a command file which was used to run the executable program which actually performs Rietveld refinement (refinement type is now 12). It was modified to avoid user intervention and to change the protocol of file names; this allows the system to use, if needed, the same files (e.g. .CCL cards) with the same names for different refinements. This new version was named "REFINC".

PICTIC - PLS

These are routines developed to display results by means of Genie. The new versions were only modified to be used inside new program and are named "TICPIC" and "PLSC".

The table 1 contains the list of original and modified files.

RAW2ASC	RAW2DAT
PROLSFILE	ASCIIDAT
ENGINFOC	PREMFOC
ENGINFOCL	PREMFOCL
ENGINFOCRT	PREMFOCRT
CCLDAT	CCL
REFINT	REFINC
PICTIC	TICPIC
PLS	PLSC

Table 1

12.4 Strain tensor extraction

As a general rule for each point inside the sample whose strain tensor has to be evaluated, we need at least data from six experiments. Since TEST instrument is provided with two detectors the actual number of experiments ("runs") to be performed on a single point could be three. This procedure will produce three *RAW files but, after focusing and refinement, six *.OUT files. Although this number of experiments has a theoretic significance we already debated about the necessity to perform at least eight to ten experiments (thus four or five runs). A number of four runs could be a good compromise between the necessities to save beam time and to maintain a good degree of accuracy and precision for the results.

Due to instrument geometry (position of detectors and incoming beam) we propose a general rule to conduct a set of runs useful for the strain tensor analysis.

Let "a" be an axis connecting the centres of the two detectors; let "b" be the vertical rotation axis of the mechanical rotating device; let "c" be an axis which is determined as that of the incoming beam path. These three axes are perpendicular and can be taken as reference rotation axes (see fig.2).

It can be demonstrated that we need only two kinds of rotations to obtain all the sample orientations we need. We chose "a" and "b" axes but programs can be easily modified to treat "c" rotations too.

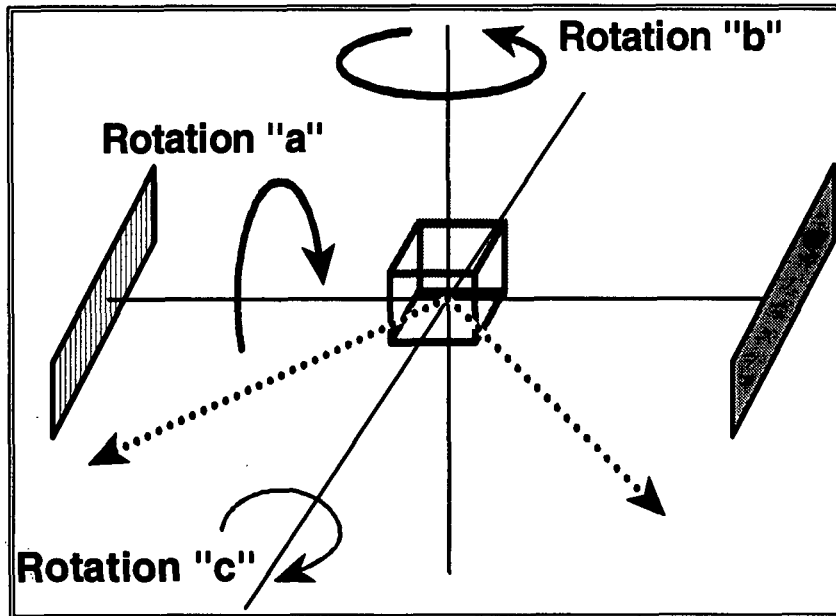


Fig.2

We assume as positive "a" rotation and positive "b" rotations those shown in fig.2.

Both "a" rotation values and "b" rotation values are "absolute" values and should be taken with reference to a well stated sample position.

Thus a good set of four experiments (runs) could be performed with reference to the rotations:

File Name	"a" Rotation (deg)	"b" Rotation (deg)
TESTxxx1	0	0
TESTxxx2	0	45
TESTxxx3	-45	0
TESTxxx4	45	0

Table 2

A good set of six or more runs could be:

File Name	"a" Rotation (deg)	"b" Rotation (deg)
TESTxxx1	0	0
TESTxxx2	0	45
TESTxxx3	-45	0
TESTxxx4	45	0
TESTxxx5	0	-22.5
TESTxxx6	0	22.5
TESTxxx7	-22.5	0
TESTxxxx

Table 3

Of course these proposals are only indicative and cannot represent a general rule.

Anyway it should be noticed that the geometry of the instrument makes superfluous any "b" rotation of more than 45°. In general "b" rotations of more than 45° could produce significant results but could also waste beam time. For example, a "b" rotation of 90° leads one of the detectors to the analysis of the same direction the other detector analysed when "b" rotation was 0°. The other direction will be the same as well while the versus will be the opposite. This means, in terms of scattering vectors, that we will have two overlapping vectors and two vectors lying on the same direction. Apart from statistical considerations we would waste beam time!

The expression for the principal tensor of the strain is very useful since one can actually "see" the strain provided that he knows how to address the new reference frame.

Now, we have stated a laboratory standard reference frame how depicted in fig.3 and a sample reference frame which is defined so as in the first sample position it overlaps the first one ("first sample position" is that position for which we have "dx"="dy"="dz"=0, "a"="b"=0). The three unit vectors (derived from the eigenvectors) which define the new coordinate system and the principal strain directions, will be expressed in terms of the laboratory reference frame. Thus there will be a well defined way to address the principal directions for the internal stress provided that during the experiment the operator has recorded the actual sample orientation when it was in the reference position.

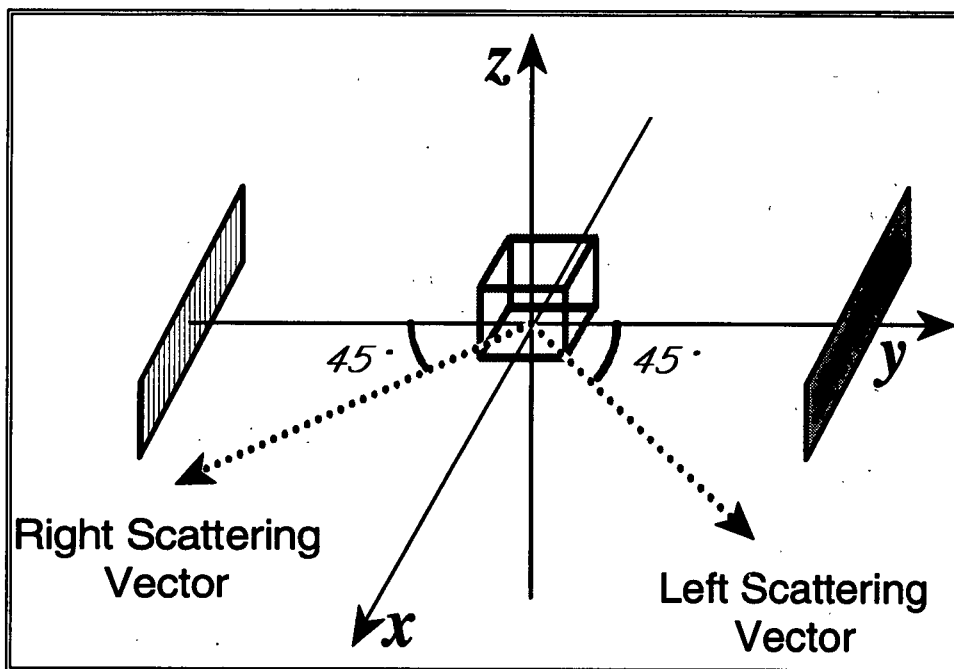


Fig.3

When the sample is shaped as a parallelepiped or a cube we suggest to sign by means of a marker the reference frame over the sample. Otherwise it would be a good idea to take a photograph of the first sample orientation.

Cycle	Experimenter	Run Num	Date	Leaf Run	Date	Target Moderator	Collimator	Focus	Batch Focus	Venue/Sum	Background	Relevance	Parameter File								
92-4	Rhodes Johnson Wright Johnson Wright	2856	10/09/92	2859	11/09/92	Tantalum Methane 2 (1 Foil)	Prototype														
		2860	11/09/92	2870	15/09/92																
		2871	18/09/92	2923	18/09/92																
		2884	18/09/92	2931	21/09/92																
2932	21/09/92	2948	23/09/92																		
92-6	Webster/Enzlo Smith/Borner	3326	03/12/92	3359	08/12/92	Tantalum Methane 2	Prototype														
		3380	08/12/92	3380	07/12/92																
92-6	Alignment Edwards Fitzpatrick Priemeayer Edwards Fitzpatrick Swallow	3460	12/12/92	3485	13/12/92	Tantalum Methane 2 (1 Foil)	Prototype	lab_commandarea_58.com													
		3497	13/12/92	3512	14/12/92																
		3513	14/12/92	3517	14/12/92																
		3518	14/12/92	3524	14/12/92																
		3525	14/12/92	3536	15/12/92																
		3537	15/12/92	3540	15/12/92																
3541	15/12/92	3582	18/12/92																		
92-7	Rose/Valeis Edwards Harrie Alignment	3732	01/02/93	3740	02/02/93	Tantalum Methane 2 (1 Foil)	Prototype	lab_commandarea_27.com													
		3741	02/02/93	3764	03/02/93																
		3758	04/02/93	3773	04/02/93																
		3774	05/02/93	3778	05/02/93																
93-1	Alignment	3800	28/05/93	3814	30/05/93	TaCH4 3	Prototype														
93-2	Alignment Webster/Enzlo Smith/Borner	3845	28/06/93	3889	01/07/93	Tantalum Methane 3 (2 Foil)	Prototype														
		3892	02/07/93	4025	08/07/93																
4026	08/07/93	4088	10/07/93																		
93-2	Alignment Priemeayer Alignment Priemeayer Edwards/Wang Harrie Fitzpatrick Ancona	4181	20/07/93	4326	04/08/93	Tantalum Methane 3 (2 Foil)	Right Hand 40 el.	lab_commandarea_93.com	utilitylab	e4290a.dat	e4218a.dat	utilitylab									
		4327	04/08/93	4333	05/08/93																
		4334	05/08/93	4355	08/08/93																
		4356	08/08/93	4389	07/08/93																
		4370	07/08/93	4387	08/08/93																
		4388	09/08/93	4394	10/08/93																
		4395	10/08/93	4399	11/08/93																
		4400	11/08/93	4416	11/08/93																
93-3	Alignment Fiori Edwards/Wang Noise tests	4418	04/10/93	4532	07/10/93	Tantalum Methane 3 (2 Foil)	Right Hand 40 el.	lab_commandarea_93.com	utilitylab	e4515.dat	e4516.dat	utilitylab									
		4533	07/10/93	4577	11/10/93																
		4578	11/10/93	4694	15/10/93																
		4623	24/10/93	4698	22/11/93																
93-5	Alignment Fiori Laxen/Harris Daymond Bourke/Goldstone Lewis/Waters Prieis Team	4983	24/02/94	5138	27/02/94	Tantalum Methane 4 (1 Foil)	135 el. left 40 el. right	lab_commandarea_93.com lab_commandarea_93.com	utilitylab	e5138.vd e5138.vr	none	utilitylab	utilitylab_5122.psm utilitylab_5122.psm utilitylab_5023.psm								
		5139	28/02/94	5168	02/03/94																
		5187	02/03/94	5434	07/03/94																
		5435	07/03/94	5449	09/03/94																
		5450	09/03/94	5580	14/03/94																
		5581	14/03/94	5822	18/03/94																
		5823	18/03/94	5901	28/03/94																
		5902	28/03/94	5971	02/04/94																
94-1	Alignment Wierand	5972	02/05/94	6028	12/05/94	Tantalum Methane 4	135 el. left 40 el. right	lab_commandarea_93.com lab_commandarea_93.com	utilitylab	e5138.vd e5138.vr	none	utilitylab	utilitylab_5023.psm								
		6029	02/05/94	6028	12/05/94																
94-2	Alignment Fiori Edwards/Wang	6010	28/05/94	6080	14/06/94	Tantalum Methane 4 (1 Foil)	135 el. left 135 el. right	lab_commandarea_8_94.com lab_commandarea_8_94.com	utilitylab	e6388.vd e6388.vr	none	utilitylab	utilitylab_6480.psm utilitylab_6480.psm								
		6081	15/06/94	6500	20/06/94																
6501	20/06/94	6670	28/06/94																		
94-3	Alignment Bourke/Goldstone Bourke/Allen/Edwards	6759	13/10/94	6928	19/10/94	Tantalum Water	135 el. left 135 el. right	lab_commandarea_10_94.com lab_commandarea_10_94.com	utilitylab	e6978.hs 1 e6978.hs 2	none	utilitylab	utilitylab_6088.psm								
		6927	19/10/94	7028	24/10/94																
7027	28/10/94	7170	03/11/94																		
94-4	Alignment Wang/Edwards/Wright Loren/Harris/Chrys	7420	15/12/94	7467	19/12/94	Tantalum Water	135 el. left 135 el. right	lab_commandarea_12_94.com lab_commandarea_12_94.com	utilitylab	e74654.hs 1 e74654.hs 2	none	utilitylab	utilitylab_7467.psm								
		7468	19/12/94	7495	19/12/94																
7496	22/12/94	7572	22/12/94																		
94-5	Alignment Daymond Wang/Edwards/Wright Webster/Allen/Edwards Ien Harrie	7873	09/01/95	7968	11/01/95	Tantalum Water	135 el. left 135 el. right	lab_commandarea_1_95.com lab_commandarea_1_95.com	utilitylab	e77554.hs 1 e77554.hs 2	none	utilitylab	utilitylab_7754.psm								
		7967	11/01/95	7984	18/01/95																
		7925	18/01/95	7928	20/01/95																
		7937	20/01/95	7991	22/01/95																
7992	24/01/95	7913	24/01/95																		
94-6	Alignment Wang/Edwards/Wright Wright - Fibre mass. Alignment Wang/Edwards/Wright Ien Harrie Wang/Edwards/Wright	8141	22/02/95	8188	22/02/95	Tantalum Water	135 el. left 135 el. right	lab_commandarea_1_95.com lab_commandarea_1_95.com	utilitylab	e88294.hs 1 e88294.hs 2	none	utilitylab	utilitylab_7754.psm								
		8189	24/02/95	8185	24/02/95																
		8186	24/02/95	8442	25/02/95																
		8588	09/03/95	8530	10/03/95																
		8531	09/03/95	8589	18/03/95																
		8570	18/03/95	8785	21/03/95																
		8787	21/03/95	8832	24/03/95																
		95-1	Alignment Laxen/Prieis Harrie Daymond Bourke/Goldstone/CH Bourke/Goldstone/CH	8927	19/05/95									9235	22/05/95	Uranium Methane 5	135 el. left 135 el. right	lab_commandarea_5_95.com lab_commandarea_5_95.com	utilitylab	e92034.hs 1 e92034.hs 2	none
9236	22/05/95			9489	28/05/95																
9490	29/05/95			9587	31/05/95																
9588	31/05/95			9830	08/06/95																
9831	11/06/95	9894	13/06/95																		
95-2	Alignment Laxen/Prieis	10017	07/07/95	10185	10/07/95	Tantalum Methane 5	135 el. left 135 el. right	lab_commandarea_7_95.com lab_commandarea_7_95.com	utilitylab	e100774.hs 1 e100774.hs 2	none	utilitylab	utilitylab_10070.psm								
		10186	12/07/95	10828	18/07/95																
95-3	Alignment Ien Harrie Edwards/Wang Ancona/ENEL Ancona/Bruno Alignment/Rock tests	10810	31/07/95	11008	03/08/95	Tantalum Methane 6	135 el. left 135 el. right	lab_commandarea_7_95.com lab_commandarea_7_95.com	utilitylab	e100774.hs 1 e100774.hs 2	none	utilitylab	utilitylab_11182.psm								
		11037	05/08/95	11073	03/08/95																
		11076	10/08/95	11143	15/08/95																
		11144	15/08/95	11174	19/08/95																
		11183	19/08/95	11341	22/08/95																
		11342	22/08/95	11899	24/08/95																
95-4	Alignment Imperial/Bellard Daymond Edwards/Wang/RR Daymond	11800	02/10/95	11891	03/10/95	Tantalum Methane 7	135 el. left 135 el. right	lab_commandarea_10_95.com lab_commandarea_10_95.com	utilitylab	e118314.hs 1 e118314.hs 2	none	utilitylab	utilitylab_11819.psm								
		11802	04/10/95	11775	08/10/95																
		11809	09/10/95	11889	15/10/95																
		11887	15/10/95	11901	17/10/95																
11940	28/10/95	11970	02/11/95																		

Note: Methane 3 installed April 1993
Methane 4 installed December 1993
Water installed July 1994
Methane 5 and uranium target installed May 1995
Tantalum reloaded July 1995
Methane 6 installed August/September 1995

UTILITY = labdata@bmg.prem.anst.gov
UTILITYN = postlab@bmg.prem.anst.gov
TEB_COMMAND = labdata@bmg.command
TEB_CALIB_VAN = labdata@bmg.calib.van
TEB_CALIB_EMPTY = labdata@bmg.calib.empty

Publications from the PREMIS Project

G Albertini, M Ceretti, R Cappola, A Lodini, P Mariani, M Perriu, F Rustichelli, *Map of Residual Strain in a Welded Aisi 304 Steel Component, Obtained by Neutron Diffraction*, in "Metallurgical Science and Technology" 11/1/93.

G Albertini, R Coppola, F Rustichelli, *Advanced Applications of Diagnostics Techniques to Fusion Reactor Materials*, in Physics Report (in print)

G Albertini, F Cernuschi, G Cicoguani, S Ghia, T Lorentzen, F Rustichelli, *Residual strain measurements in welded steel Fe 5101*, (submitted to Baltimore Conference).

L Edwards, M W Johnson, H Priesmeyer, F Rustichelli, P Withers & J Wright, "Precise measurements of internal stress within materials using neutrons." in Proc of 3rd European Conf on Residual Stress Frankfurt (1992)

Daymond, M.R. & Withers, P.J. (1995). *An Examination of Tensile/Compressive Loading Asymmetries in Aluminium based MMCs using the Finite Element Method*. Mat. Sci. Tech **11**, 228-236.

Daymond, M.R. & Withers, P.J. (1994). *Thermal Cycling of Whisker Reinforced Metal Matrix Composites - A Comparison Between Finite Element Models and Experimental Results*. In: Numerical Predictions of Deformation Processes and the Behaviour of Real Materials. Edited by S.I. Anderson et al. (Risø National Laboratory, Risø, Roskilde, Denmark) 293-298.

Daymond, M.R. & Withers, P.J. (1995). *In Situ Monitoring of Thermal Cycled Metal Matrix Composites Using Laser Extensometry and Neutron Diffraction*. In: Int. Conf. on Composite Materials 10. Edited by A. Poursartip and K. Street (Woodhead, Whistler, Canada) 621-628.

Daymond, M.R. & Withers, P.J. (1996). *Stroboscopic Neutron Diffraction Monitoring of Metal Matrix Composites Undergoing Rapid Thermal Cycling*. Scripta Met. (Accepted for publication),

Daymond, M.R. & Withers, P.J. *Neutron Diffraction & Laser Extensometry in-situ Monitoring of Thermally Cycled Metal Matrix Composites*, J. Appl. Composites (1996). (Accepted for publication),

Daymond, M.R. & Withers, P.J. (1996). *Internal Strains in Metal Matrix Composite Undergoing Rapid Thermal Cycling Determined by Neutron Diffraction*. Acta metall. mater., To be published,

Daymond, M.R. & Withers, P.J. *A Synchrotron Radiation Study of Transient Internal Strain Changes During the Early Stages of Thermal Cycling in MMCs*, Submitted to Scripta Met. et Mat. (1996)

L Edwards, D Q Wang, M W Johnson, J S Wright, H G Priesmeyer, F Rustichelli, G Albertini, P J Withers and I B Harris, *Precise Measurement of Internal stresses within materials using pulsed neutrons*, (PREMIS). Submitted to:- ICRS-4 (Baltimore, June 1994).

- Fitzpatrick, M. E. (1995). Effects of Residual Stress on Fatigue in a Metal Matrix Composite. PhD thesis, Cambridge University.
- Fitzpatrick, M.E., Hutchings, M.T., King, J.E., Knowles, D.M. and Withers, P.J., *The Effect of Thermal Residual Stress Fields on Crack Growth in Al/SiC_p Metal Matrix Composites*, in "IXth Int Conf. Composite Materials", (1993), A. Miravete (eds.), Madrid, Univ. Zaragoza, p.642-649.
- Fitzpatrick, M.E., Downes, T.J., Hutchings, M.T., King, J.E., Knowles, D.M. and Withers, P.J., *The Effect of Long-range Thermal Residual Stress Fields on Fatigue Growth in Al-SiC_p Metal Matrix Composite Materials & their Measurement by Neutron Diffraction*, in "4th International Conference on Residual Stresses", (1994), M.R. James (eds.), Baltimore, Soc. for Exp. Mechanics, p.559-568.
- Fitzpatrick, M.E., Hutchings, M.T. and Withers, P.J., *The Determination of the Profile of Macrostress & Thermal Mismatch Stress Through an Al/SiC_p Composite Plate from the Average Residual Strains Measured in each Phase*, *Physica B*, 213/214 (1995), p.790-792.
- Fitzpatrick, M.E., Hutchings, M.T., King, J.E., Knowles, D.M. and Withers, P.J., *Effect of Thermal Residual Stresses on Fatigue Crack Opening & Propagation Behaviour in an Al/SiC Metal Matrix Composite*, *Met Trans A*, 26A, 3191 -3198 (1995), .
- M. E. Fitzpatrick , M. T. Hutchings, C. G. Windsor, & P. J. Withers, Separation of Macroscopic, Elastic Mismatch and Thermal Expansion Mismatch Stresses in Particle-Reinforced Metal Matrix Composite Quenched Plates from Neutron Diffraction Measurements, Submitted to *Acta Met. et Mat.*, (1995).
- M.E. Fitzpatrick, P.J. Withers, A Baczmarski, M.T. Hutchings, R Levy, M. Ceretti, A Lodini, The Effect of Plastic Flow on Thermal Mismatch Stress in Al/SiC MMC, ECRS4, Cluny, France, June 1996.
- I Harris, P J Withers, M W Johnson, L Edwards, H G Priesmeyer, F Rustichelli & J S Wright, *A New Technique for Strain Measurement within Materials*, Accepted for pub. in EUROMAT '95, Padua, Sept. 1995.
- M W Johnson , N J Rhodes & J Wright, ENGIN: An instrument for the measurement of internal stresses using neutrons , Proc. ICANS XII. (1993) RAL-94-025
- Korsunsky, A.M., Fitzpatrick, M.E. and Withers, P.J., *Neutron Diffraction Measurement & Modelling of Stresses Around Fatigue Cracks in Al/SiC Particulate Composites*, in "Int. Conf. on Composite Materials 10", (1995), A. Poursartip and K. Street (eds.), Whistler, Vancouver, p.545-552.
- A T Ozdemir, R Cooke, L Edwards, *Residual Stress Distribution Around Cold Experimental Holes* in Proc. ICAF (International Committee on Aeronautical Fatigue) Stockholm (1993)
- Ozdemir, A.T, Wang, D.Q. and Edwards, L, *Measurement of the 3D residual stress distribution at split sleeve cold expanded holes*, Proc. ICRS-4, Publ. SEM, USA, 1994

Wang D Q & Edwards L, Precise Determination of Specimen Surface Position During Near Surface Strain Scanning by Neutron Diffraction, ECRS 4, Cluny, France 1996

Wang D Q, Harris I B, Withers P J & Edwards L, Near Surface strain measurement using Neutron Diffraction, ECRS 4, Cluny, France 1996

Watts M R, Fitzpatrick M E, Korsunsky A M, and Withers, P J, X-ray and Neutron Diffraction Measurements of Micro and Macro stresses in MMCs, ECRS4, Cluny, June 1996.

Withers, P.J., Clarke, A.P. and Fitzpatrick, M.E., *Internal stress Considerations during Crack Growth in Al/SiC Particulate Composites*, in "Intrinsic & Extrinsic Fracture Mechanisms in Inorganic Composite Systems", (1994), J.J. Lewandowski and W.H. Hunt (eds.), Las Vegas, TMS, p.49-56.

P J Withers, I B Harris, L Edwards, D Q Wang, M W Johnson, J S Wright, H G Priesmeyer, J Larsen, F Rustichelli, G Albertini, *ENGIN - A Neutron Spectrometer for internal stress measurement in Engineering Structures* Submitted to Inst. Symp. on Adv Materials for Lightweight Structures, Noordwijk, Holland, March 1994.